이학박사 학위논문

Deformation microstructures of chlorite peridotite: Implications for seismic anisotropy and intermediate-depth earthquakes

녹니석 페리도타이트의 변형미구조가 지진파 이방성과 중발지진 발생에 미치는 영향

2022 년 8 월

서울대학교 대학원

지구환경과학부

김 도 현

Doctoral Thesis

Deformation microstructures of chlorite peridotite: Implications for seismic anisotropy and intermediate-depth earthquakes

Dohyun Kim

A dissertation submitted in partial fulfillment of the requirements for the degree of Doctor of Philosophy

School of Earth and Environmental Sciences

Seoul National University

August 2022

Deformation microstructures of chlorite peridotite: Implications for seismic anisotropy and intermediate-depth earthquakes

지도 교수 정 해 명

이 논문을 이학박사 학위논문으로 제출함
2022 년 8 월

서울대학교 대학원
지구환경과학부
김 도 현

김도현의 이학박사 학위논문을 인준함
2022 년 8 월

위 원 장 이 준 기 (인)

부위원장 정 해 명 (인)

위 원 이 현 우 (인)

위 원 길 영 우 (인)

위 원 박 문 재 (인)

ABSTRACT

Deformation microstructures of chlorite peridotite: Implications for seismic anisotropy and intermediate-depth earthquakes

Dohyun Kim
School of Earth and Environmental Sciences
The Graduate School
Seoul National University

To understand seismic anisotropy and mechanism of intermediate-depth earthquakes observed in subduction zones, microstructures of naturally and experimentally deformed chlorite peridotite were studied. As the first step, chlorite peridotite from Almklovdalen, southwest Norway was analyzed. Olivine showed previously reported lattice preferred orientation (LPO) types and chlorite showed two different LPO types, named as type-1 and type-2. The type-1 chlorite LPO is characterized by the [001] axes aligned subnormal to the foliation, and the type-2 chlorite LPO is characterized by a girdle distribution of the [001] axes subnormal to the lineation. Chlorite had much stronger LPOs than olivine, and affected much more on seismic anisotropy in subduction zones. The polarization direction of the fast S-wave rotated 90° depending on the dip angle (θ) in subducting slab. Low angle ($\theta \leq 45°$) subducting slab can contribute to trench-normal seismic anisotropy,

and high angle ($\theta > 50°$) subducting slab can contribute to trench-parallel seismic anisotropy. As the second step, high pressure-temperature (P-T) deformation experiments were conducted to find out the mechanism for causing the two different LPOs of chlorite. Under high P-T conditions (P = 0.5–2.5 GPa, T = 540–720 °C, γ = 1.7–6.3), simple shear deformation experiments of chlorite peridotite produced two different types of chlorite LPO. The type-1 chlorite LPO developed under low shear strain ($\gamma \leq 3.1 \pm 0.3$), producing trench-parallel seismic anisotropy. The type-2 chlorite LPO developed under high shear strain ($\gamma \geq 5.1 \pm 1.5$), producing trench-normal seismic anisotropy. As the final step, dehydration embrittlement of chlorite was studied to understand the mechanism of intermediate-depth (50–300 km) earthquakes in subduction zones. Deformation experiments of chlorite peridotite were conducted under high P-T conditions (P = 0.5–2.5 GPa, T = 500–750 °C). Partial dehydration of chlorite was observed under high pressure conditions ($1.5 \leq P \leq 2.5$ GPa), with fault microstructures and Ca-amphibole which was dehydration product. Because the phase of chlorite peridotite is predicted stable over double seismic zone of subducting slabs, this result shows chlorite can be the mineral which triggers intermediate-depth earthquakes in double seismic zone.

Keywords : chlorite, lattice preferred orientation, seismic anisotropy, earthquake, dehydration embrittlement

Student Number : 2012-20335

TABLE OF CONTENTS

CHAPTER 1: Introduction

Seismic anisotropy is important to understand internal structures of the Earth, which is interpreted by seismic wave data. When natural or artificial underground impact produces seismic wave, it reaches the Earth's surface through elastically anisotropic medium. Therefore, understanding seismic anisotropy which is produced by elastically anisotropic medium is essential to interpret seismic data which implies deep Earth structures human cannot reach yet. Seismic anisotropy has been observed in the fore-arc mantle wedge in many subduction zones (Long, 2013; Long and Silver, 2008; Park and Levin, 2002; Russo and Silver, 1994; Savage, 1999). The polarization direction of the fast S-wave is often trench-normal in the back-arc area, but changes to trench-parallel in the fore-arc area (Huang et al., 2011a, b; Smith et al., 2001). This anisotropy can be attributed to olivine, the most dominant mineral in upper mantle (Jung and Karato, 2001b; Karato et al., 2008; Kneller et al., 2007; Wang and Zhao, 2013). It is known that the different types of the lattice preferred orientations (LPOs) of olivine can affect seismic anisotropy (Jung and Karato, 2001b; Kneller et al., 2007; Long and Silver, 2008; Wang and Zhao, 2013). However, seismic anisotropy observed in some subduction zones cannot be explained by olivine LPOs alone (McCormack et al., 2013; Wagner et al., 2013).

Elastically anisotropic hydrous minerals are thought to be responsible to trench-parallel seismic anisotropy (Wagner et al., 2013). Chlorite is one of the elastically anisotropic hydrous minerals, which has wide a stability field in the

upper mantle pressure-temperature (P-T) conditions (Fumagalli and Poli, 2005; Hacker et al., 2003b; Padrón-Navarta et al., 2010; van Keken et al., 2011). Therefore, chlorite possibly exists in the mantle wedge and subducting slab as chlorite peridotite (Fumagalli and Poli, 2005; van Keken et al., 2011; Wada et al., 2012). In addition, chlorite is elastically anisotropic very much because of its phyllosilicate structure (Deer et al., 2013; Mainprice and Ildefonse, 2009) (Fig. 1). When chlorite is deformed to form a strong LPO, it can affect seismic anisotropy (Han and Jung, 2021; Jung, 2017; Kang and Jung, 2019; Kim and Jung, 2015; Kim et al., 2020; Lee et al., 2020). However, deformation microstructure of chlorite in high P-T conditions has not been studied yet.

Intermediate-depth (50–300 km) earthquakes have been reported in many subducting slabs (Abers et al., 2013; Kirby et al., 1996; Kita et al., 2010; Kita et al., 2006), although brittle deformation hardly occurs in high P-T conditions (Green and Houston, 1995; Kirby, 1995; Raleigh and Paterson, 1965). Three hypotheses are possible mechanism for intermediate-depth earthquakes: transformational faulting, ductile shear instability, and dehydration embrittlement (Hacker et al., 2003b). Transformational faulting is a fault-making process by weaker reaction products of phase transformation (Green and Burnley, 1989; Kirby, 1987). Ductile shear instability is that a shear instability generates heat faster, melts failure planes and causes slip at relatively low shear stresses (Ogawa, 1987). Among them dehydration embrittlement was proposed as a plausible mechanism of intermediate-depth earthquakes of subducting slabs (Green and Houston, 1995; Hacker et al., 2003b; Jung and Green, 2004; Jung et al., 2004; Kirby, 1995; Raleigh and Paterson, 1965). Experimental studies of Jung and Green (2004) and Jung et al. (2004) found

out that dehydration embrittlement of serpentine can cause intermediate-depth earthquakes. Experiments of Okazaki and Hirth (2016) found out that dehydration embrittlement of lawsonite also can cause intermediate-depth earthquakes in subducting oceanic crust. Even though chlorite breakdown also may influence double seismic zone seismicity (Fumagalli and Poli, 2005; Hacker et al., 2003b; Hasegawa and Nakajima, 2017; Mishra and Zhao, 2004; Wang et al., 2017), there have been no evidence for dehydration embrittlement of chlorite yet.

In Chapter 2, the LPOs and microstructures of natural chlorite peridotites from Almklovdalen, southwest Norway were studied to understand the trench-parallel seismic anisotropy of olivine and chlorite in subduction zone. Almklovdalen is in the Western Gneiss Region (WGR) of Norway, which has been experienced ultrahigh-pressure (UHP) metamorphism (3.6 GPa and 800 °C) called Scandian Orogeny (Hacker et al., 2010; Lapen et al., 2009; Wang et al., 2013). Studied samples were deformed chlorite peridotites which have been exhumed due to the collision of Baltica and Laurentia (Hacker et al., 2010; Lapen et al., 2009; Wang et al., 2013). The LPOs of olivine and two different chlorite LPO types were found using electron backscattered diffraction (EBSD) in scanning electron microscope (SEM). Seismic anisotropy was calculated from the LPO data of olivine and chlorite. Olivine showed weak LPOs and seismic anisotropy, but strong LPOs of chlorite highly enhanced seismic anisotropy of chlorite peridotite. Furthermore, it was found out that the polarization direction of the fast S-wave rotated 90° depending on the dip angle (θ) of chlorite peridotite in subducting slab. It is also found that low angle ($\theta \leq 45°$) subducting slab can contribute to trench-normal seismic anisotropy, and high angle ($\theta > 50°$) subducting slab can contribute to

trench-parallel seismic anisotropy. The strong LPO of chlorite can be a source of the observed seismic anisotropy in the mantle wedge as well as in subducting slabs where chlorite is stable.

In Chapter 3, experimental study on the chlorite peridotite at high P-T was conducted in simple shear to understand the LPO development of chlorite. Not only the type-1 of chlorite LPO has been previously reported (Cardenes et al., 2021; Han and Jung, 2021; Kang and Jung, 2019; Kim and Jung, 2015; Lee et al., 2020; Morales et al., 2013; Padrón-Navarta et al., 2015; Puelles et al., 2012; Schmidtke et al., 2021), but the type-2 of chlorite LPO has been reported in natural samples (Cardenes et al., 2021; Kim and Jung, 2015; Lee et al., 2020; Padrón-Navarta et al., 2015; Schmidtke et al., 2021; Wallis et al., 2015). However, there have been no studies for the deformation conditions and mechanism to form these LPOs of chlorite yet. Modified Griggs apparatus was used to conduct simple shear deformation experiments of chlorite peridotite from Almklovdalen, Norway. The experiment conditions were P = 0.5–2.5 GPa, T = 540–720 °C, and strain rate 2.7–9.7×10^{-6} s^{-1}. Four samples (JH100, JH101, JH154, and JH156) were deformed in low shear strain ($\gamma \leq 3.1\pm0.3$) and other four samples (JH116, JH127, JH138, and JH152) were deformed in high shear strain ($\gamma \geq 5.1\pm1.5$). Results showed that the LPO of chlorite was changed depending on shear strain, independent of P-T conditions. Experiments with low shear strain showed strong chlorite LPOs with [001] axes aligned subnormal to the shear plane (type-1). Experiments with high shear strain showed a girdle distribution of chlorite [001] axes subnormal to the shear direction (type-2). This study suggests that chlorite LPO can be changed depending on shear strain. Crystal rotation accompanied by grain size reduction

with increasing shear strain possibly causes different LPOs of chlorite. We also found that the type-1 chlorite LPO could produce trench-parallel seismic anisotropy in the fore-arc zones, whereas the type-2 chlorite LPO could produce trench-normal seismic anisotropy in the back-arc area of subduction zones.

In Chapter 4, experimental study on the dehydration embrittlement of chlorite at high P-T was conducted to understand mechanism of intermediate-depth earthquakes. Modified Griggs apparatus was used to conduct simple shear deformation experiments of chlorite peridotite from Almklovdalen, Norway. The experiment conditions were P = 0.5–2.5 GPa, T = 500–750 °C, and strain rate 2.7–9.7×10^{-6} s^{-1}. Samples showed fault development at high pressure conditions ($1.5 \leq P \leq 2.5$ GPa) with partial dehydration of chlorite. At low pressure ($0 < P < 1.5$ GPa), there was neither fault microstructures nor dehydration products. Detailed analysis by energy dispersive spectrometer (EDS) mapping and field emission electron probe micro analyzer (FE-EPMA) determined partial dehydration product observed along fault plane at high pressure was Ca-amphibole, which did not exist in the starting material (Kim and Jung, 2015). Only under intermediate-depth pressure conditions ($1.5 \leq P \leq 2.5$ GPa) samples were fault-developed with partially dehydrated chlorite. Furthermore, it was known that chlorite peridotite phase was stable over double seismic zone of subducting slabs. The result implies that dehydration embrittlement of chlorite can explain intermediate-depth earthquake of double seismic zone of subducting slabs.

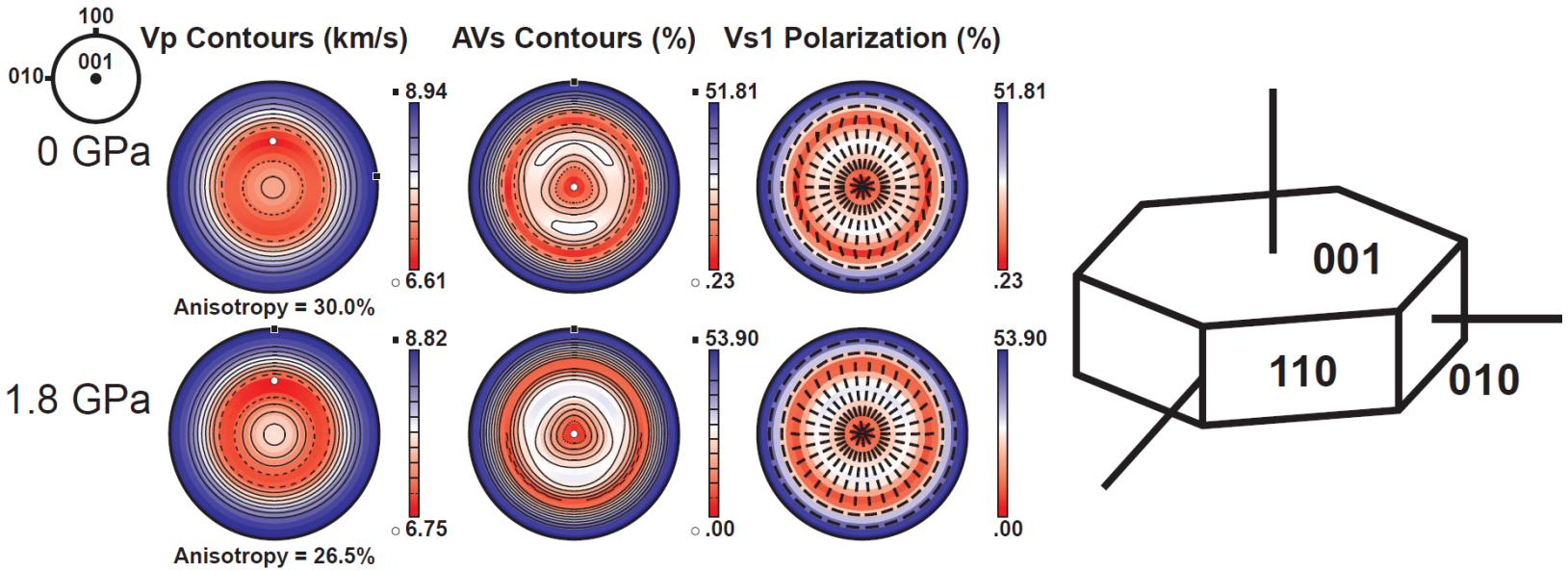

Figure 1. Seismic velocity and anisotropy for a single crystal of chlorite, presented in the lower hemisphere using an equal-area projection. The P-wave velocity (Vp), amplitude of S-wave anisotropy (AVs), and the polarization direction of the fast S-wave (Vs1) are plotted. The center of the pole figure represents the [001] axis, the E-W direction represents the [010] axis, and the N-S direction represents the [100] axis. The elastic constant of chlorite for two different pressure conditions came from Mookherjee and Mainprice (2014). Simplified cartoon for chlorite crystal structure was modified after Deer et al. (2013).

CHAPTER 2: Deformation microstructures of olivine and chlorite in chlorite peridotites from Almklovdalen in the Western Gneiss Region, southwest Norway and implications for seismic anisotropy

**** This chapter has been modified from a published paper:***

Kim, D., and Jung, H., 2015, Deformation microstructures of olivine and chlorite in chlorite peridotites from Almklovdalen in the Western Gneiss Region, southwest Norway, and implications for seismic anisotropy: International Geology Review, v. 57, no. 5-8, p. 650-668.

Abstract

Chlorite peridotites from Almklovdalen in southwest Norway were studied to understand the deformation processes and seismic anisotropy in the upper mantle. The lattice preferred orientation (LPO) of olivine and chlorite was determined using electron backscattered diffraction (EBSD)/scanning electron microscope. A sample with abundant garnet showed [100] axes of olivine aligned subparallel to lineation, and [010] axes aligned subnormal to foliation: A-type LPO. Samples rich in chlorite showed different olivine LPOs. Two samples showed [001] axes aligned subparallel to lineation, and [010] axes aligned subnormal to foliation: B-type LPO. Two other samples showed [100] axes aligned subparallel to lineation, and [001] axes aligned subnormal to foliation: E-type LPO. Chlorite showed a strong LPO characterized by [001] axes aligned subnormal to foliation with a weak girdle

subnormal to lineation. Fourier transform infrared (FTIR) spectroscopy of the specimens revealed that the olivines with A-type LPO contain a small amount (170 ppm H/Si) of water. In contrast, the olivines with B-type LPOs contain a large amount (340 ppm H/Si) of water.

The seismic anisotropy of the olivine and chlorite was calculated. Olivine showed Vp anisotropy of up to 3.8% and a maximum Vs anisotropy of up to 2.7%. However, the chlorite showed a much stronger Vp anisotropy, up to 21.1% and a maximum Vs anisotropy of up to 31.7%. A sample with a mixture of 25% of olivine and 75% of chlorite can produce a Vp anisotropy of 14.2% and a maximum Vs anisotropy of 22.9%. Because chlorite has a wide stability field at high pressure and high temperature in subduction zone, the strong LPO of chlorite can be a source of the observed trench-normal or trench-parallel seismic anisotropy in the mantle wedge as well as in subducting slabs depending on the dipping angle of slab in a subduction zone where chlorite is stable.

Keywords: chlorite, lattice preferred orientation, petrofabrics, seismic anisotropy

1. Introduction

Since olivine is the most dominant mineral in the upper mantle, the LPO of olivine is useful for studying mantle flow and the seismic anisotropy of the upper mantle (Karato et al., 2008; Long and Silver, 2008; Nicolas and Christensen, 1987). Therefore, there were numerous studies on the LPO of olivine. In dry condition, A-type olivine LPO which is characterized by the [100] axes aligned subparallel to the shear direction, and the [010] axes aligned subnormal to the shear plane was found (Jung and Karato, 2001b) and frequently found in the upper mantle (ben Ismaïl and Mainprice, 1998; Jung et al., 2009a; Nicolas and Christensen, 1987). Deformation experiments at high pressures and high temperatures have revealed that A-, B-, C-, D- and E-type LPOs of olivine exist in other deformation conditions as well (Bystricky et al., 2000; Couvy et al., 2004; Holtzman et al., 2003; Jung and Karato, 2001b; Jung et al., 2006; Jung et al., 2009b; Karato et al., 2008; Katayama et al., 2004; Ohuchi et al., 2012; Ohuchi et al., 2011). In wet condition, B-, C-, or E-type olivine LPOs were found (Jung and Karato, 2001b; Jung et al., 2006; Katayama et al., 2004; Katayama and Karato, 2006). The correlation between olivine LPOs and water content has been established (Jung et al., 2006). The B-type LPO is characterized by [001] axes aligned subparallel to the shear direction, and [010] axes aligned subnormal to the shear plane. The C-type LPO is characterized by [001] axes aligned subparallel to the shear direction, and [100] axes aligned subnormal to the shear plane. The E-type LPO is characterized by [100] axes aligned subparallel to the shear direction, and [001] axes aligned subnormal to the shear plane.

Water-related olivine fabrics have also been reported in several natural peridotites and mantle xenoliths. Mizukami et al. (2004) found the B-type olivine LPO in garnet peridotites from the Higashi-akaishi peridotites body of southwest Japan. Katayama et al. (2005) found the C-type olivine LPO in garnet peridotites from Otrøy Island, in the Western Gneiss Region in Norway. Skemer et al. (2006) found the B-type olivine LPO in garnet peridotites from Cima di Gagnone, Switzerland. Michibayashi et al. (2007) and Park and Jung (2015) found B-type olivine LPOs in the southern Mariana trench and in mantle xenoliths from Shanwang, eastern China, respectively. Webber et al. (2008) found the B-type olivine LPO in mantle peridotites from Red Hills, New Zealand. Jung (2009) and Jung et al. (2014) found both B- and E-type olivine LPOs in peridotites from Val Malenco in Italy and from Bergen Arc in southwest Norway, respectively. Jung et al. (2013) also reported the C-type olivine LPO in garnet peridotites in the North Qaidam UHP belt in northwest China. Michibayashi and Oohara (2013) found both C- and E-type olivine LPOs in dunites in the shear zone from the Fizh massif, Oman Ophiolite. Park et al. (2014) found under hydrous condition the C-type olivine LPO in mantle xenoliths from Adams Diggings in the Rio Grande Rift, USA.

Trench-parallel seismic anisotropy has been observed in the fore-arc mantle wedge in many subduction zones (Long, 2013; Long and Silver, 2008; Park and Levin, 2002; Russo and Silver, 1994; Savage, 1999). The polarization direction of the fast S-wave is often trench-normal in the back-arc area, but changes to trench-parallel in the fore-arc area (Huang et al., 2011a, b; Smith et al., 2001). This anisotropy can be attributed to the B-type olivine LPO (Jung and Karato, 2001b;

Kneller et al., 2007). Wang and Zhao (2013) also reported trench-parallel seismic anisotropy above the mantle wedge, as well as in the slab of Tohoku and Kyushu, Japan, which was interpreted to be caused by the fabric transition to B-type olivine LPO in the presence of water. Recently, McCormack et al. (2013) found a thin layer (~6 km) of strong anisotropy (~10–14%) beneath Ryukyu with a slow axis of symmetry directly above the slab, which cannot be explained by the olivine LPO. Wagner et al. (2013) also found trench-parallel seismic anisotropy using Rayleigh waves beneath Cascadia, and suggested that hydrous minerals in the mantle wedge or in the slab may also be responsible for trench-parallel seismic anisotropy. Typical anisotropic hydrous minerals are serpentine and chlorite, which are formed by dehydration of the subducting slab. The seismic anisotropy of serpentine has been previously reported, revealing that serpentine can be responsible for trench-parallel seismic anisotropy if the serpentine is stable at depth (Jung, 2011; Katayama et al., 2009; Nishii et al., 2011; Watanabe et al., 2011). The stability field of serpentine and chlorite at high pressure and high temperature is known (Fumagalli and Poli, 2005; Hacker et al., 2003b; Padrón-Navarta et al., 2010; Ulmer and Trommsdorff, 1995; van Keken et al., 2011). Chlorite is known to be stable in a wide range of pressures and temperatures in subduction zones (Fumagalli and Poli, 2005; van Keken et al., 2011; Wada et al., 2012). However, the LPO type and seismic characteristics of chlorite have not been well studied.

In this paper, we studied the LPO of chlorite and olivine in chlorite peridotites from Almklovdalen, southwest Norway, and found that chlorite has a strong LPO and can produce significant seismic anisotropy in the mantle wedge and in the slab at high pressure and high temperature.

2. Geological setting and sample characteristics

The Western Gneiss Region in Norway experienced collision with Baltica and Laurentia and exhumation to crustal levels at 425–380 Ma, an event called the Scandian Orogeny (Hacker et al., 2010; Lapen et al., 2009; Wang et al., 2013). This collision triggered UHP metamorphism at 800 °C and 3.6 GPa (Hacker et al., 2010). The WGR is the lowest structure unit in the Scandinavian Caledonides (Lapen et al., 2009). The major domain of the WGR is biotite, hornblende, and garnet containing gneisses with eclogites and peridotites (Hacker et al., 2010; Wang et al., 2013). Almklovdalen, located in the WGR of Norway (Fig. 2), has some garnet peridotite bodies that came from Archean mantle fragments embedded in the Proterozoic Baltic continental crust (Hacker et al., 2010; Lapen et al., 2009; Wang et al., 2013). Almklovdalen has also some peridotites with high chlorite content, which may be attributed to hydrated garnet.

We collected six peridotites from Almklovdalen. The major minerals in the samples consist of olivine (60–83%) and chlorite (2–35%), and the minor minerals are orthopyroxene (1–7%) and clinopyroxene (2–13%). The compositional layering of the garnet/pyroxene, olivine, and chlorite is well developed (Figs. 3a, b), and grains are mostly elongated (Fig. 4). Garnets are generally round with a large grain size (~1 cm), and chlorites tend to be aligned to form a sheet structure (Figs. 3b and 4b, c). One sample (434) is especially abundant in garnet (19%) compared to the other chlorite-rich samples (Table 1). Figure 4a shows a large garnet grain with elongated olivines (sample 434). Three samples (435, 436, and 438) contain more chlorite (31–35%) than the other samples (Table 1).

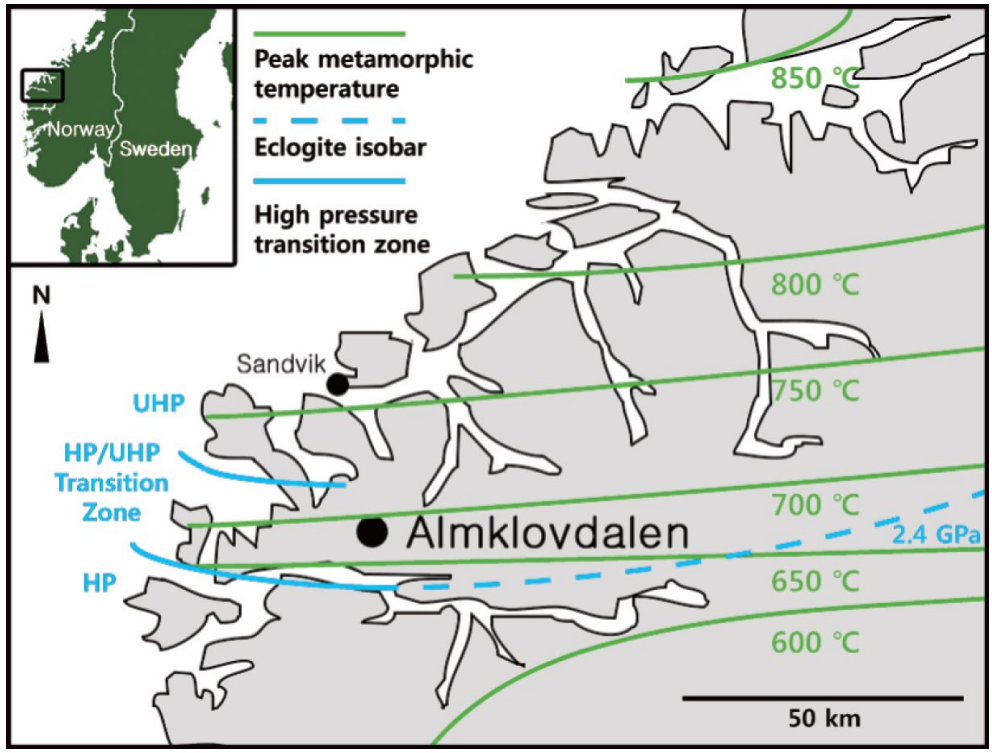

Figure 2. Location of study area, Almklovdalen, southwest Norway, with pressure and temperature contours (modified after Wang et al. (2013)).

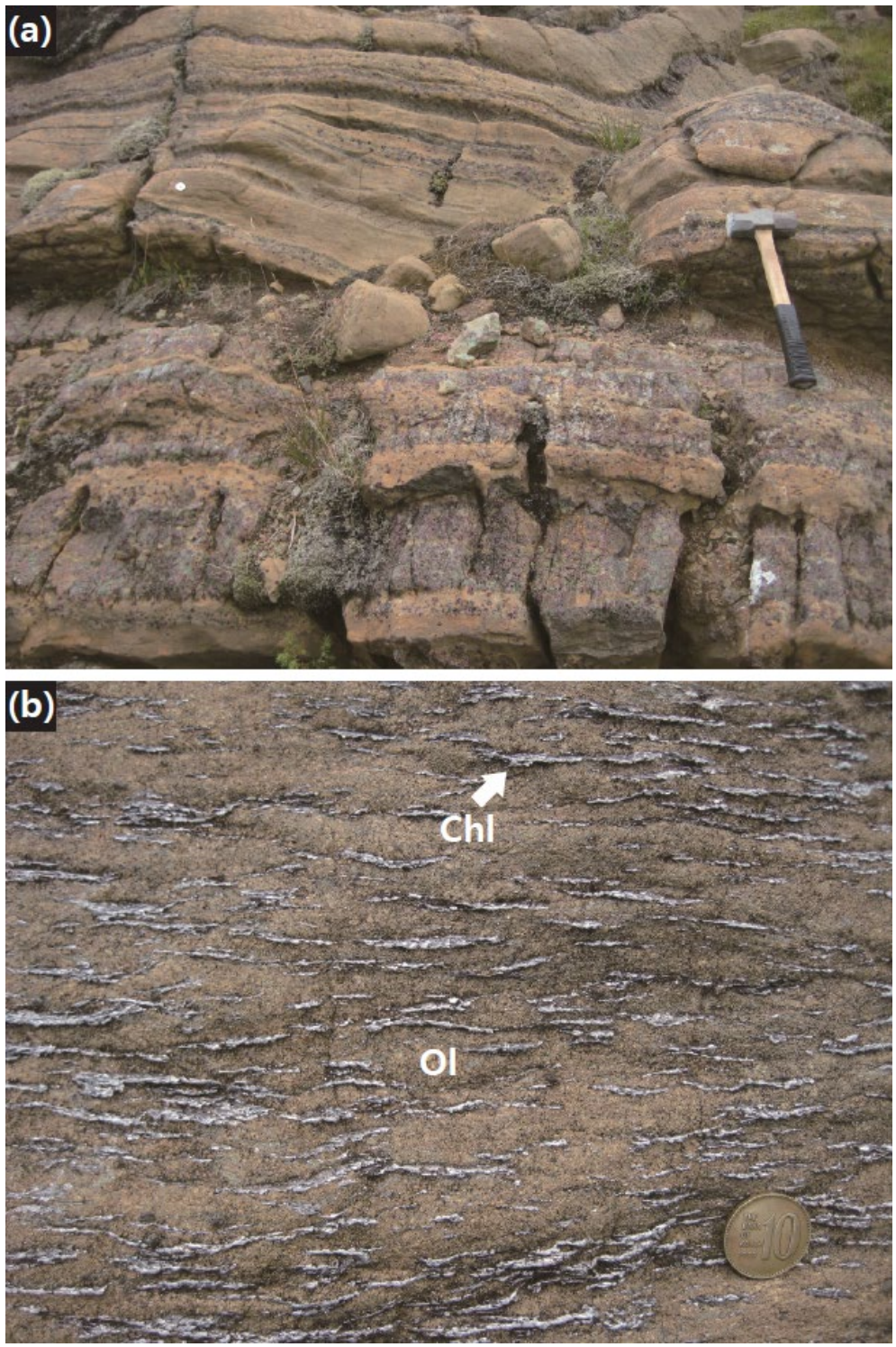

Figure 3. Outcrops of Almklovdalen peridotites. **(a)** Compositional layering of olivine-rich and pyroxene/garnet-rich peridotite. Olivine is shown as a yellowish brown color after oxidation on the surface. Hammer is 40 cm long. **(b)** Chlorite-rich peridotite with elongated lenses of chlorite. Coin has a diameter of 22.86 mm. Ol, olivine; Chl, chlorite.

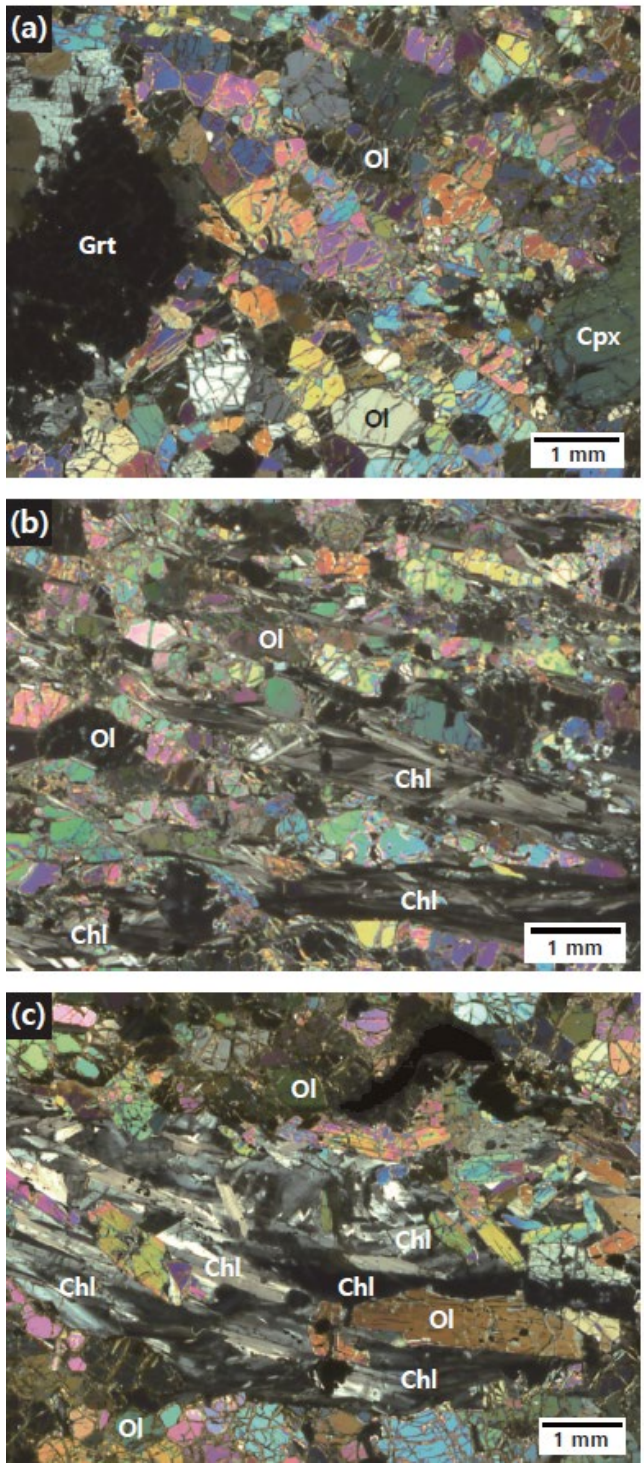

Figure 4. Optical photomicrographs in cross-polarized light. **(a)** Sample 434 showing relatively large garnet grain, with elongated small olivines. **(b)** Sample 436 showing notable chlorite lenses elongated sub-parallel to the lineation. **(c)** Sample 438 with abundant chlorite grains elongated. (Ol, olivine; Cpx, clinopyroxene; Chl, chlorite; and Grt, garnet).

3. Methods

3.1. Measurement of LPO and calculation of seismic anisotropy

The foliation of the samples was determined by compositional layering of chlorite, garnet/pyroxene, and olivine. The lineation of the samples was determined by the shape-preferred orientation of minerals in the foliation plane, using the projection-function method (Panozzo, 1984). Samples were cut, and thin sections were made on the x-z plane (x: lineation, z: normal to foliation). The LPO of samples was determined using EBSD in a JEOL JSM-6380 SEM housed at the School of Earth and Environmental Sciences (SEES) at Seoul National University (SNU). The accelerating voltage was 20 kV, and the working distance was 15 mm in the SEM. An HKL EBSD system with channel 5 software was used for the EBSD analysis. The EBSD patterns of every grain were analyzed manually to ensure correct indexing, and the fabric strength of the LPO was estimated using the misorientation index (M-index) (Skemer et al., 2005). The M-index ranges from 0 (random fabric) to 1 (single crystal).

The seismic anisotropy of these peridotites was calculated from the LPO data of olivine and chlorite. Minor minerals such as orthopyroxene and clinopyroxene were ignored. The elastic constant of olivine came from Abramson et al. (1997), and that of chlorite came from Aleksandrov and Ryzhova (1961). The newest elastic constant of chlorite at P = 1.8 GPa (Mookherjee and Mainprice, 2014) was also used to compare the resultant seismic anisotropy. The ANIS2k and VpG programs (Mainprice, 1990) were used to calculate seismic wave velocity and seismic anisotropy.

3.2. Measurement of water content in olivine

Fourier transform infrared (FTIR) spectroscopy was used to measure water content in the olivine samples. A Nicolet 6700 FTIR spectrometer with a continuum IR microscope housed at the Tectonophysics laboratory at the SEES at SNU was used to collect unpolarized FTIR spectra using the transmitted light. Samples for FTIR analysis were both-side-polished to a thickness of 100–350 μm (Table 1), depending on the grain size of the specimen. Additionally, they were heated to T = 120 °C for 24 hours to eliminate water from the surface. The sample chamber was purged with N_2 gas to exclude atmospheric moisture during the IR measurements. The aperture size was 100 × 100 μm, and only one sample (sample 436) used an aperture size of 50 × 50 μm. The IR beam was penetrated through a clean area of olivine without any cracks, inclusions, or grain boundaries. The water content of 10 different grains was measured and averaged. The water content of the olivine was calculated from infrared absorptions in the wavenumbers 3400–3620 cm^{-1}, the range of the O-H stretching vibrations. The calibration of Paterson (1982) was used, following the former studies of olivine LPOs in wet condition (Jung and Karato, 2001b; Jung et al., 2006; Katayama et al., 2004; Katayama and Karato, 2006).

3.3. Dislocation microstructure of olivine

An oxygen decoration technique (Kohlstedt et al., 1976) was used to observe the dislocation microstructures of the olivine specimens. Samples were heated to T = 800 °C for one hour to oxidize the specimens. After that, each sample was polished with Syton (colloidal silica) to remove a thin oxide layer from the surface. Prepared samples were carbon-coated to be used in the JEOL JSM-6380 SEM.

Backscattered electron images (BEI) were taken with an acceleration voltage of 15 kV and a working distance of 10 mm to observe the dislocation microstructures of the olivine specimens in the SEM (Jung and Karato, 2001a; Karato, 1987).

3.4. EPMA analysis and P-T estimation of specimen

A JEOL JXA-8900R electron probe micro analyzer (EPMA) at the National Center for Inter-university Research Facilities (NCIRF) at SNU was used to analyze the chemical composition of the minerals. The accelerating voltage was 15 kV, the working distance was 11 mm, and the beam size was 5 μm. Samples with abundant garnet (434) and chlorite (438) were selected, and two garnet grains from sample 434 and two chlorite grains from sample 438 were analyzed. Three olivine grains from each sample were also analyzed. The grains were observed at the core and rim areas, and the results were averaged to represent each grain. The results of the EPMA analysis were recalculated using Minpet 2.02, written by Dr. Yong-Joo Jwa, Gyeongsang National University, Republic of Korea.

For the P-T calculations, the oxide mass percentage was used. The oxides came from the olivine, clinopyroxene, and garnet grains of sample 434, 435, 436, and 439. The ptex13 program written by Dr. Andrei Girnis, Goethe University, Frankfurt, Germany, was used for the P-T calculation.

Table 1. Sample description and results.

Sample	Modal composition						LPO of Ol	M-index[1]		IR sample thickness (μm)	Water content of Ol[2] (ppm H/Si)	Recrystallized grain size of Ol[3] (μm)	Stress[4] (MPa)
	Ol (%)	Opx (%)	Cpx (%)	Spl (%)	Chl (%)	Grt (%)		Ol	Chl				
434	60.3	6.5	12.6	0.5	1.6	18.5	A	0.049	-	130	170±30	496	17±15
435	58.3	1.5	4.9	0.5	34.4	0.4	B	0.045	0.083	100	310±30	481	39±15
436	60.4	4.6	2.7	0.6	30.5	1.1	B	0.035	0.099	230	210±30	389	47±15
437	81.9	2.7	5.4	3.0	5.1	1.9	E	0.056	-	350	180±30	314	50±15
438	61.8	0.6	1.7	0.4	35.3	0.2	~E	0.069	0.082	160	170±30	328	50±15
439	83.0	1.7	4.8	5.7	2.1	2.7	C	0.060	-	100	-	465	41±15

[1]M-index represents fabric strength (Skemer et al., 2005).

[2]The water content of 10 different grains were measured and averaged. The calibration of Paterson (1982) was used. The water content of sample 439 was omitted because of its poor resolution of the IR spectrum.

[3]Recrystallized grain size was measured using the linear intercept method (Gifkins, 1970).

[4]Stress was estimated from the recrystallized grain size of olivine (Jung and Karato, 2001a).

Ol: olivine, Opx: orthopyroxene, Cpx: clinopyroxene, Spl: spinel, Chl: chlorite, and Grt: garnet.

Table 2. Chemical composition of major minerals.

Sample	434					438				
Mineral	Grt 1	Grt 2	Ol 1	Ol 2	Ol 3	Chl 1	Chl 2	Ol 1	Ol 2	Ol 3
SiO_2	41.50	41.73	40.54	39.46	40.67	31.25	30.98	40.33	40.47	39.90
TiO_2	0.04	0.08	0.03	0.02	0.01	0.03	0.04	0.01	-	0.04
Al_2O_3	23.97	23.98	0.01	0.03	0.00	17.44	17.95	-	0.02	-
Cr_2O_3	1.49	1.52	-	-	-	1.31	1.59	-	-	-
FeO	12.42	12.01	11.68	11.60	11.57	4.12	3.87	13.19	13.09	13.37
MnO	0.41	0.41	0.07	0.09	0.10	0.03	0.04	0.20	0.18	0.19
MgO	17.76	18.03	48.67	48.32	48.76	31.87	31.63	47.57	47.48	47.34
CaO	4.81	4.91	-	0.01	-	0.03	0.01	-	0.02	-
Na_2O	0.03	0.01	0.01	0.01	0.02	-	0.01	0.03	0.02	-
K_2O	-	-	0.01	0.04	-	0.01	-	-	0.02	-
NiO	-	-	0.80	0.68	0.80	-	-	0.55	0.45	0.35
Total	102.41	102.66	101.81	100.24	101.94	86.10	86.13	101.89	101.74	101.18
O=12										
Si	2.930	2.935	2.964	2.934	2.969	1.999	1.979	2.964	2.976	2.955
Al	1.992	1.986	-	0.001	-	1.313	1.351	-	-	-
Ti	0.002	0.004	-	0.001	-	0.002	0.002	-	-	0.003
Fe^{2+}	0.675	0.660	0.714	0.722	0.705	0.220	0.207	0.812	0.804	0.828
Fe^{3+}	0.058	0.046	-	-	-	-	-	-	-	-
Cr	0.083	0.084	-	-	-	0.066	0.081	-	-	-
Mn	0.024	0.024	0.005	0.006	0.006	0.001	0.002	0.012	0.012	0.012
Mg	1.869	1.890	5.304	5.359	5.304	3.039	3.013	5.214	5.204	5.226
Ca	0.364	0.370	-	-	-	0.001	-	-	0.002	-
Na	0.002	-	-	-	0.002	-	0.001	0.005	0.003	-
K	-	-	-	0.001	-	-	-	-	0.002	-
Ni	-	-	0.047	0.040	0.048	-	-	0.033	0.027	0.021
Cations	8.001	8.000	9.033	9.064	9.033	6.641	6.635	9.039	9.029	9.045
Mg#	71.8	72.8	88.1	88.1	88.3	93.2	93.6	86.5	86.6	86.3

Garnet-rich (434) and chlorite-rich (438) samples were selected, and each measurement is the average of the core and rim area of each grain.

Ol: olivine, Chl: chlorite, and Grt: garnet.

4. Results

4.1. Mineral chemistry and P-T estimation of specimens

The chemical compositions of major minerals from EPMA analysis are shown in Table 2. The chemical composition of each mineral did not differ much by grain and sample. The Mg#, 100*Mg/(Mg+Fe), of the olivines was 86.32–88.27, indicating that the olivines are close to forsterite (Fo_{86}–Fo_{88}). The garnets had high Al and Mg contents, and the averaged garnet composition was $Alm_{23}Adr_2Grs_6Prp_{64}Sps_1Uv_4$ (Alm: almandine, Adr: andradite, Grs: grossular, Prp: pyrope, Sps: spessartine, Uv: uvarovite). The chlorites contained Mg and Fe^{2+}, possibly close to clinochlore.

The P-T conditions were calculated from averaged core and rim EPMA data of olivine, clinopyroxene, and garnet. The pressure was calculated using the method of clinopyroxene barometer for garnet peridotites (Nimis and Taylor, 2000). The temperature was calculated using the method of Fe-Mg exchange between clinopyroxene and garnet (Berman et al., 1995; Nakamura and Hirajima, 2005), and Ca partitioning between olivine and clinopyroxene (Köhler and Brey, 1990). The estimated pressure was 2.2 GPa. The temperature for the A-type olivine LPO (sample 434) was 689 °C using the Berman et al. (1995) method, and 769 °C using the Nakamura and Hirajima (2005) method. The temperature for the B-type olivine LPO (samples 435 and 436) was 741 °C using the Köhler and Brey (1990) method. The temperature for the C-type olivine LPO (sample 439) was 908 °C using the Köhler and Brey (1990) method.

4.2. LPO of minerals

4.2.1. LPO of olivine

The LPOs of olivine are plotted in pole figures (Fig. 5). Six peridotite samples showed various olivine LPOs. Sample 434, with abundant garnet, showed [100] olivine axes aligned subparallel to the lineation, and [010] axes aligned subnormal to the foliation, close to A-type LPO. Two samples (435 and 436) showed [001] axes aligned subparallel to the lineation, and [010] axes aligned subnormal to the foliation, consistent with B-type LPO (Jung and Karato, 2001b). Sample 437 showed [100] axes aligned subparallel to the lineation, and [001] axes aligned subnormal to the foliation, consistent with E-type LPO (Katayama et al., 2004). Sample 438 showed [100] axes aligned subparallel to the lineation, and [010] and [001] axes aligned subnormal to the foliation. Sample 439 showed [001] axes aligned subparallel to the lineation, and [100] axes aligned subnormal to the foliation, close to C-type LPO (Jung et al., 2006). The fabric strength was represented as a misorientation index (M-index) (Skemer et al., 2005). The M-index of the olivine ranged from 0.035 to 0.069, which is relatively weak (Table 1).

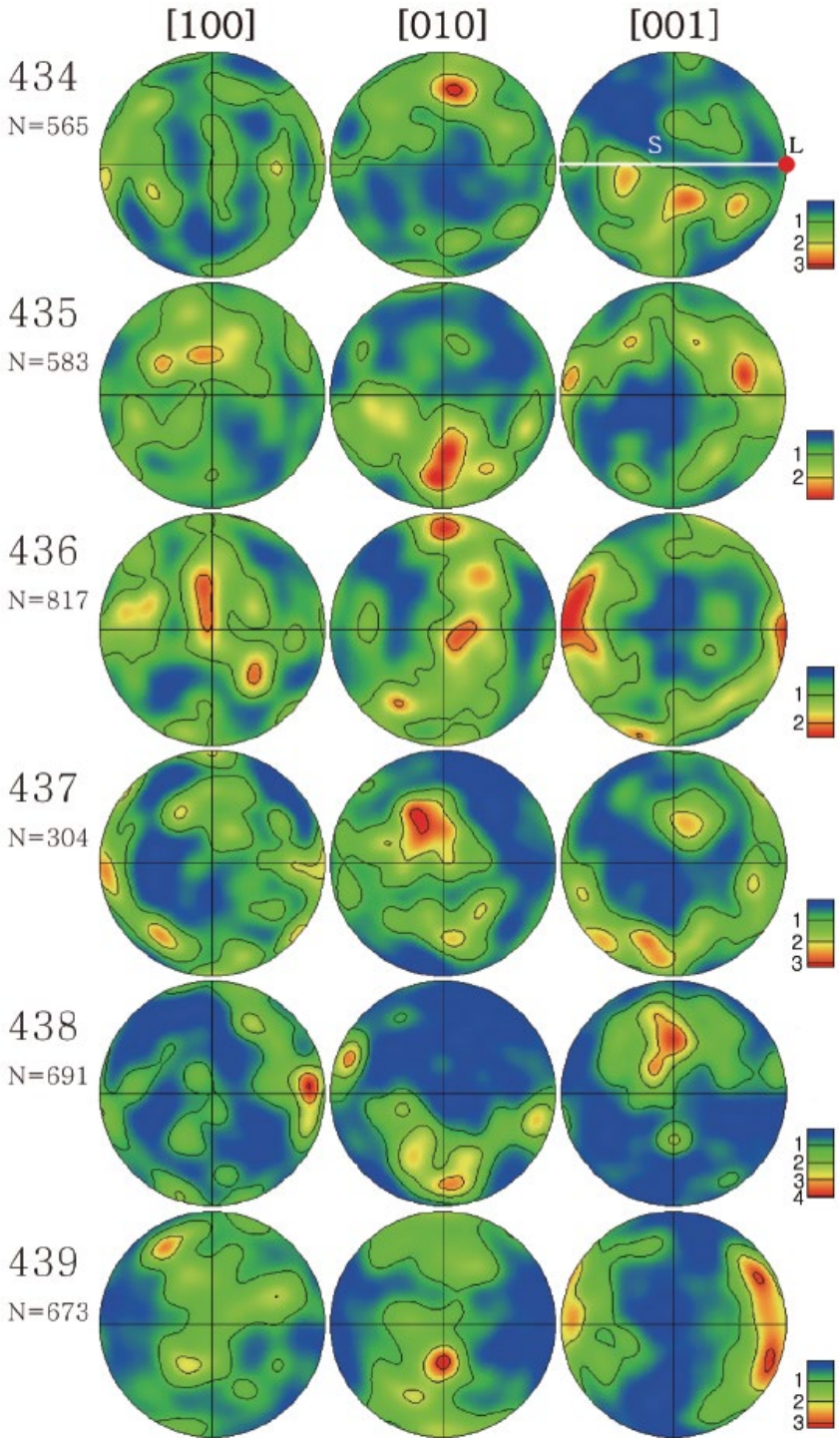

Figure 5. Pole figures of olivine presented in the lower hemisphere using an equal-area projection. The white line (S) indicates the foliation and the red dot (L) indicates the lineation. N represents the number of grains, and a half-scatter width of 20° was used for the contours. The red color represents the high density of data points, and the numbers in the legend correspond to the multiples of uniform distribution.

4.2.2. LPO of chlorite

The LPOs of chlorite are plotted in pole figures (Fig. 6). Three samples (435, 436, and 438) had enough chlorite content to plot. Two samples (435 and 436) showed [001] axes strongly aligned subnormal to the foliation, with a weak girdle subnormal to the lineation, and both [100] axes and poles of (010) and (110) are aligned subparallel to the lineation with a weak girdle along the foliation. Sample 438 showed [001] axes weakly distributed as a girdle subnormal to the lineation, and both [100] axes and poles of (010) and (110) aligned subparallel to the lineation. The M-index of the chlorite ranged from 0.082 to 0.099, which is much stronger than that of olivine (Table 1).

4.3. Seismic anisotropy

Seismic anisotropy was calculated for the individual minerals olivine and chlorite, and for the mixture of olivine and chlorite (Table 3; Figs. 7 and 8). In the case of olivine-only, the P-wave anisotropy $(Vp_{max}\text{-}Vp_{min})/Vp_{mean}$ was weak in the range of Vp = 1.8–3.8% with an average of 2.9%, and the maximum shear-wave anisotropy was also weak AVs = 1.66–2.68%. The maximum P-wave velocity was 8.41–8.53 km/s with an average of 8.47 km/s (Fig. 7). In the case of chlorite-only, using the elastic constant of chlorite (Aleksandrov and Ryzhova, 1961), the P-wave anisotropy was high, in the range of 14.9–21.1%, with an average of 18.2%, and the maximum shear-wave anisotropy was very high, up to 14.46–31.74%. The maximum P-wave velocity was 7.21–7.41 km/s with an average of 7.30 km/s (Fig. 8a). In the case of the mixture of olivine and chlorite, seismic anisotropy was based on the compositional ratio between olivine and chlorite for samples 435, 436, and 438. In this case, the P-wave anisotropy was in the range of 6.2–8.3%, with an

average of 7.5%, and the maximum shear-wave anisotropy was 6.93–13.10% (Fig. 8b). These results indicate that seismic wave propagation in chlorite is much more anisotropic than that in olivine, and chlorite can provide a significant effect of overall seismic anisotropy. Using the elastic constant of chlorite at P = 1.8 GPa (Mookherjee and Mainprice, 2014), seismic anisotropy was also calculated and compared with the results which were obtained using the elastic constant of chlorite (Aleksandrov and Ryzhova, 1961). In general, the maximum P-wave velocity of chlorite was increased, but seismic anisotropy of P- and S-wave was decreased slightly using the recent elastic constant of chlorite (Mookherjee and Mainprice, 2014), but still preserved high anisotropy of chlorite (Table 3). The ratio change of chlorite in a rock specimen can affect both Vp and Vs1 seismic anisotropy. Considering LPOs of olivine and chlorite (sample 436), Figure 9 shows that increasing chlorite ratio increases both Vp and Vs1 anisotropy.

The polarization direction of the fast S-wave (Vs1) is also plotted in Figures 7 and 8. In the case of olivine-only (Fig. 7), the A-type olivine LPO (sample 434) showed a polarization direction of the fast S-wave subparallel to the lineation for vertically propagating S-waves, the B-type olivine LPO (samples 435 and 436) showed a polarization direction of the fast S-wave subnormal to the lineation, the C-type olivine LPO (sample 439) showed a polarization direction subnormal to the lineation, and the E-type olivine LPO (samples 437 and 438) showed a polarization direction subparallel to the lineation. In the case of chlorite-only (Fig. 8a), all three samples (435, 436, and 438) showed a polarization direction of the fast S-wave subparallel to the lineation for vertically propagating S-waves. It is notable that chlorite (sample 436) produces Vs1 polarization anisotropy of up to 31.74%. In the

case of the mixture of olivine and chlorite (Fig. 8b), it is found that the polarization direction of the fast S-wave closely follows that of chlorite-only. The samples (435 and 436) with a high Vs1 polarization anisotropy showed a trend of axial anisotropy, where high and low anisotropy is found close to the horizontal and vertical planes, respectively (Fig. 8b).

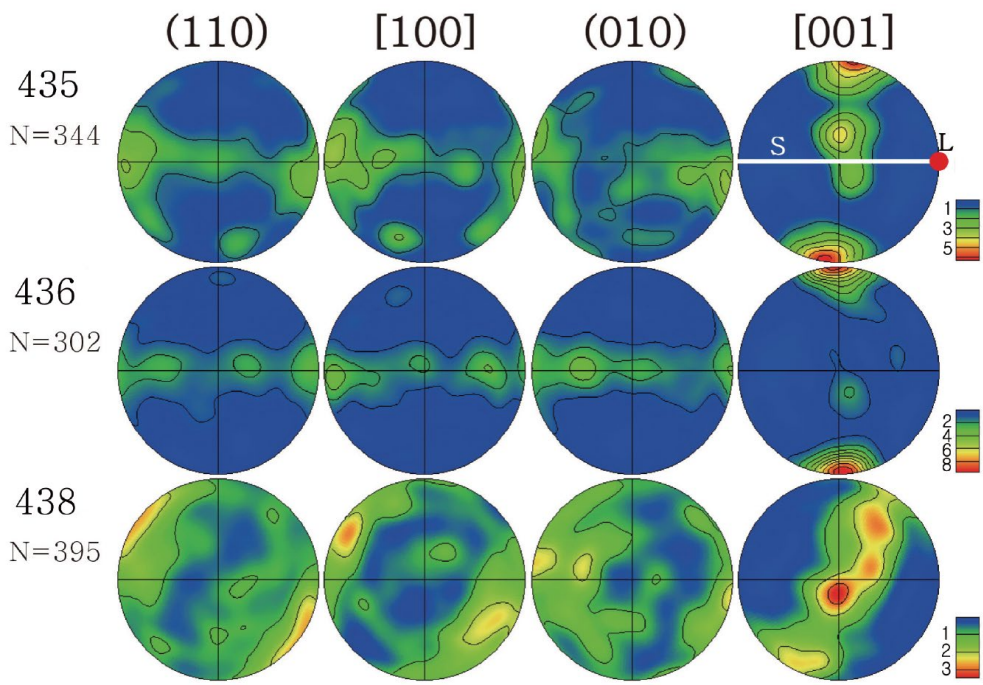

Figure 6. Pole figures of chlorite presented in the lower hemisphere using an equal-area projection. The white line (S) indicates the foliation and the red dot (L) indicates the lineation. N represents the number of grains, and a half-scatter width of 20° was used for the contours. The red color represents the high density of data points, and the numbers in the legend correspond to the multiples of uniform distribution.

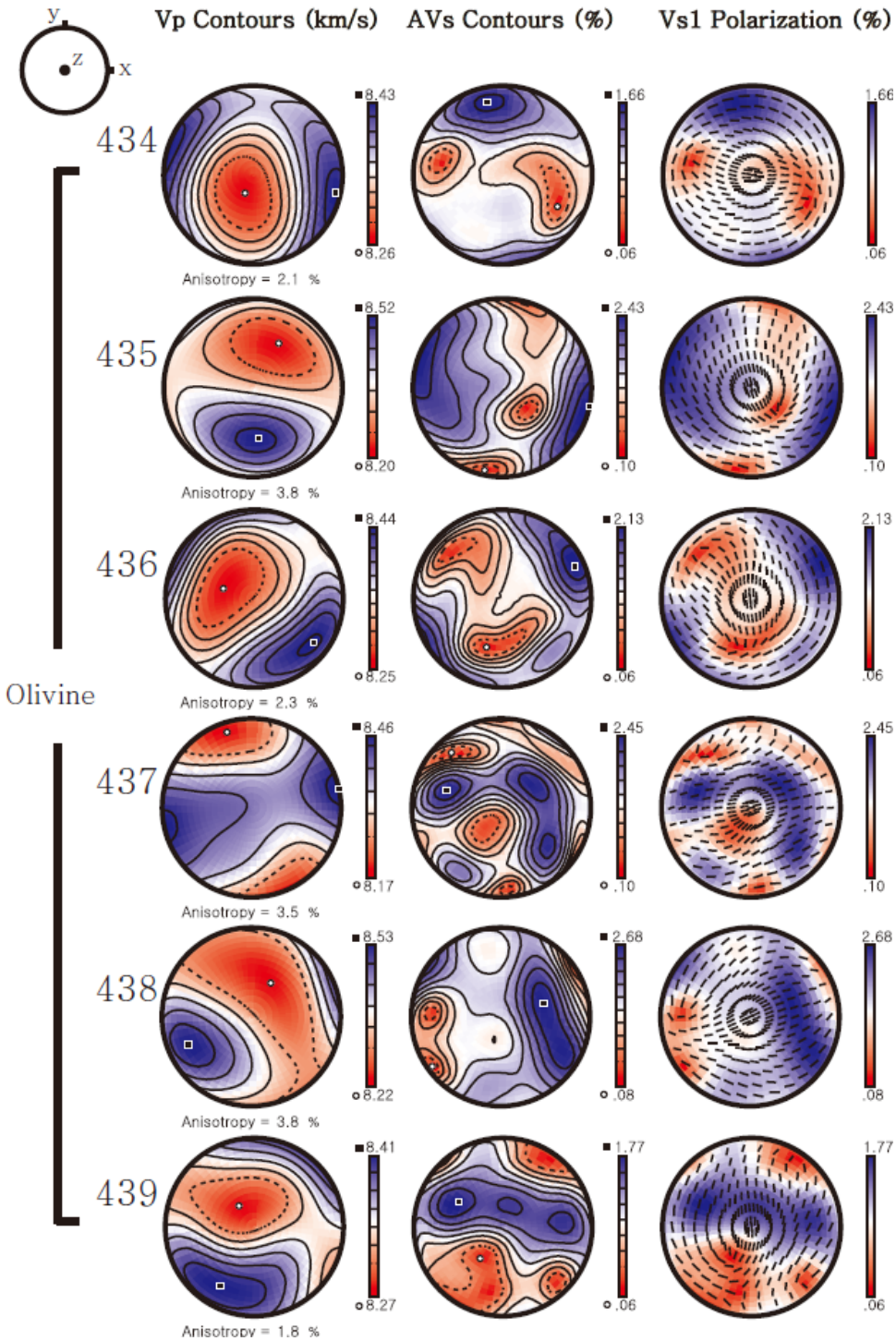

Figure 7. Seismic anisotropy and velocity calculated from the LPO of olivine-only, presented in the lower hemisphere using an equal-area projection. The center of the pole figure (z) is the direction normal to the foliation, and the E-W direction (x) represents the lineation. The P-wave velocity (Vp), amplitude of S-wave anisotropy (AVs), and the polarization direction of the fast S-wave (Vs1) are plotted.

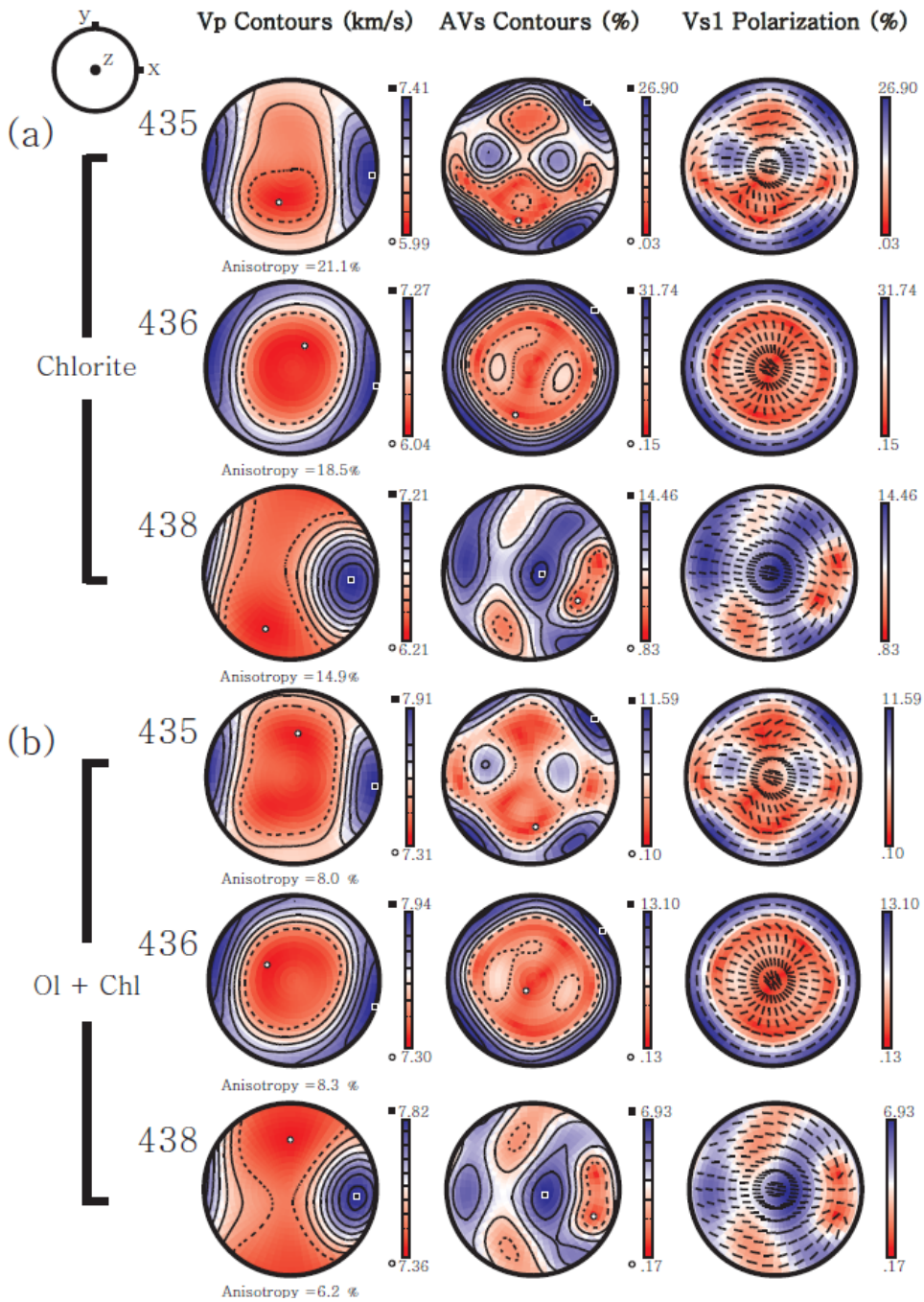

Figure 8. Seismic anisotropy and velocity calculated from LPOs of **(a)** chlorite-only and **(b)** mixture of olivine and chlorite presented in the lower hemisphere using an equal-area projection. The center of the pole figure (z) is the direction normal to the foliation, and the E-W direction (x) represents the lineation. The P-wave velocity (Vp), amplitude of S-wave anisotropy (AVs), and the polarization direction of the fast S-wave (Vs1) are plotted. The modal compositions of olivine and chlorite in Table 1 were used to calculate the seismic velocity and anisotropy in **(b)**.

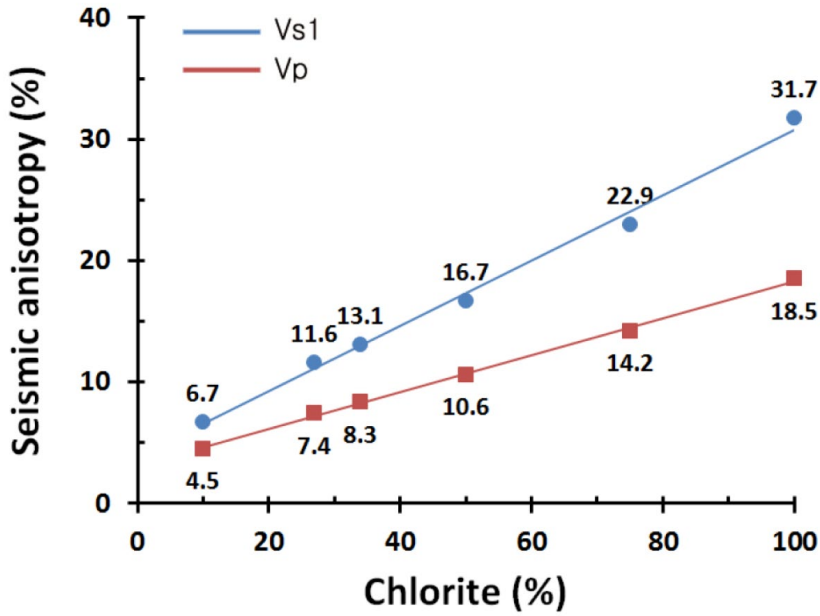

Figure 9. The relation between chlorite content and seismic anisotropy, considering LPOs of olivine and chlorite (sample 436).

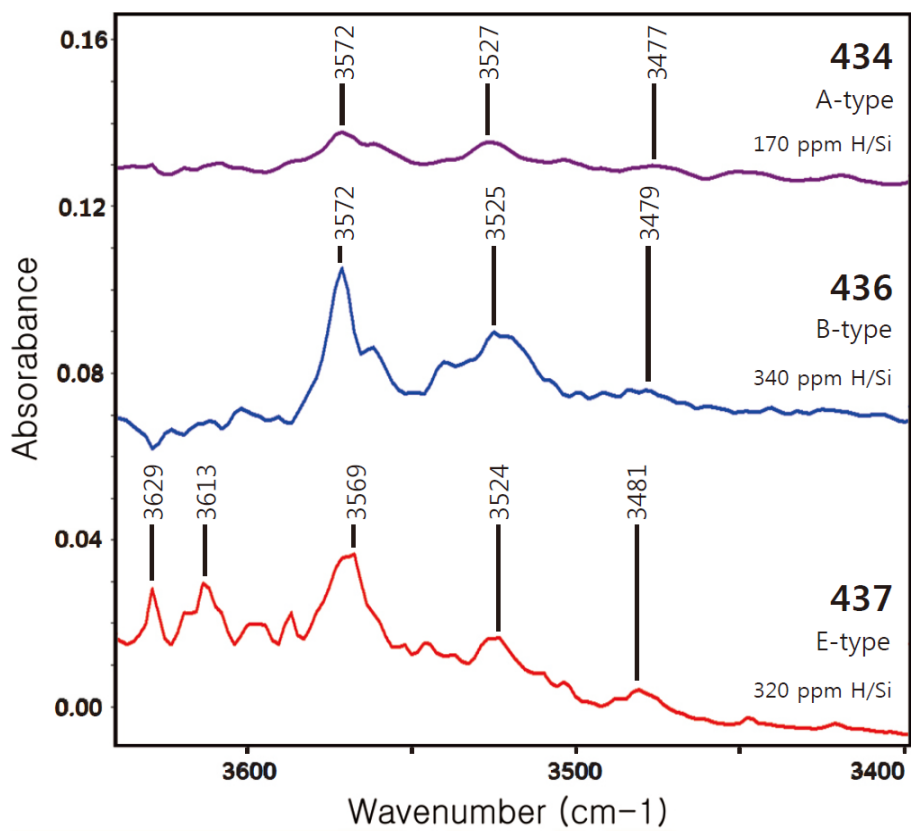

Figure 10. Representative unpolarized FTIR spectra of the olivine showing each type of LPO. Sample 439 was omitted because of its poor resolution of the IR spectrum.

Table 3. Seismic velocity and anisotropy of olivine, chlorite, and whole rock.

Sample	Max. Vp of Ol (km/s)	Vp anisotropy of Ol (%)	Max. AVs anisotropy of Ol (%)	Max. Vp of Chl (km/s)	Vp anisotropy of Chl (%)	Max. AVs anisotropy of Chl (%)	Max. Vp of whole rock (km/s)	Vp anisotropy of whole rock (%)	Max. AVs anisotropy of whole rock (%)
434	8.43	2.1	1.66	-	-	-	-	-	-
435	8.52	3.8	2.43	7.41 (8.27)	21.1 (15.2)	26.90 (20.25)	7.91 (8.26)	8.0 (5.7)	11.59 (8.64)
436	8.44	2.3	2.13	7.27 (8.17)	18.5 (13.3)	31.74 (22.82)	7.94 (8.28)	8.3 (6.0)	13.10 (9.53)
437	8.46	3.5	2.45	-	-	-	-	-	-
438	8.53	3.8	2.68	7.21 (8.10)	14.9 (10.3)	14.46 (10.61)	7.82 (8.20)	6.2 (4.3)	6.93 (5.16)
439	8.41	1.8	1.77	-	-	-	-	-	-

The values inside the bracket ( ) are calculated using the elastic constants of chlorite from Mookherjee and Mainprice (2014). Ol: olivine, Chl: chlorite.

4.4. Water content of olivine

Typical FTIR spectra of olivine are shown in Figure 10. Olivine grains showed IR absorption peaks at and near the wavenumbers 3479, 3525, 3572, and 3613 cm^{-1} (Fig. 10), which are related to the stretching vibrations of O-H bonding (Kohlstedt et al., 1996; Mei and Kohlstedt, 2000). Two samples (435 and 436) that showed B-type olivine LPOs had a high water content in the olivine: 210–310 ± 30 ppm H/Si (Table 1). If the calibration of Bell et al. (2003) is used, water content will be four times higher (Mosenfelder et al., 2006). These water contents are relatively high, indicating that these peridotites were deformed under wet condition. However, sample 434, which showed an A-type olivine LPO, had a low water content, approximately 170 ± 30 ppm H/Si (Table 1).

4.5. Dislocation microstructure

Dislocation microstructures of the olivines are shown in the BEIs from the SEM (Fig. 11). Dislocations are shown as white dots and lines. Sample with A-type olivine LPO (sample 434) showed curved and straight dislocations (Figs. 11a, b). Some dislocations were aligned and formed subgrain boundaries (Fig. 11b). Sample with ~E-type olivine LPO showed generally a straight dislocation (Fig. 11c) and also showed aligned dislocations, forming a subgrain boundary (Fig. 11d). Dislocations of the sample with B-type olivine LPOs (samples 435 and 436) were distributed heterogeneously (Figs. 11e, f) and subgrain boundary was rarely found, which is consistent with previous experimental study under wet condition (Jung et al., 2006).

4.6. Stress estimation of samples

A recrystallized grain size of olivine can be used to estimate the differential stress of a sample (Jung and Karato, 2001a; Karato et al., 1980; van der Wal et al., 1993). The recrystallized area of olivine was selected on the thin section of the x-z plane. The recrystallized grain size of olivine was measured using the linear intercept method (Gifkins, 1970; Russ and Dehoff, 2012). The measured 2-D recrystallized grain size was converted to 3-D recrystallized grain size by multiplying a factor of 1.5, and the recrystallized grain size of olivine in each sample was in the range of 314–496 μm (Table 1). To estimate the stress of samples, the recrystallized grain size piezometer (Jung and Karato, 2001a) was used for both dry (A-type olivine LPO) and wet (B- and E-type olivine LPOs) conditions. Sample with A-type olivine LPO (sample 434) showed a low stress 17 ± 15 MPa and other samples with other types of olivine LPOs showed a little higher stress 39–50 ± 15 MPa (Table 1).

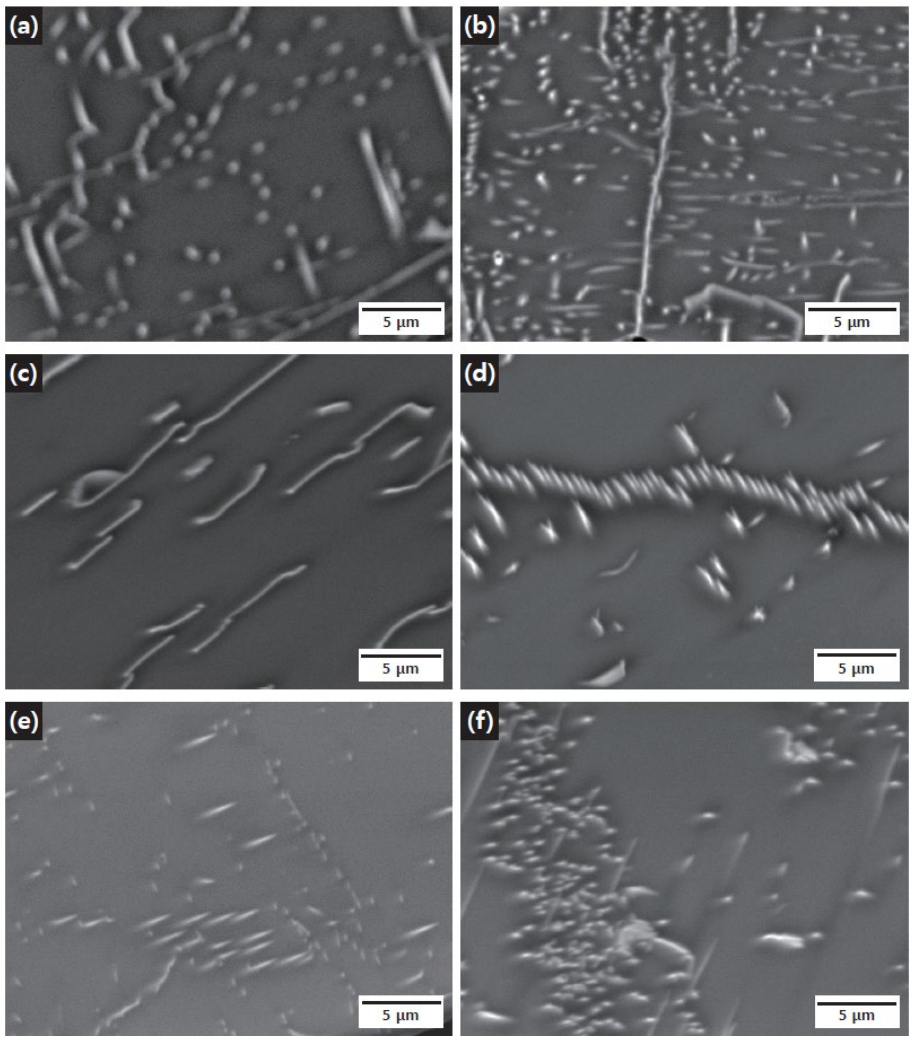

Figure 11. BEIs of olivine showing dislocation microstructure. **(a and b)** Curved and straight dislocations in olivine with an A-type LPO (sample 434). **(c and d)** Straight and aligned dislocations forming a subgrain boundary with an E-type LPO (sample 438). **(e and f)** Heterogeneous distribution of dislocations in olivine with a B-type LPO (**e**, sample 436; **f**, sample 435).

5. Discussion

Various types of olivine LPOs, such as A-, B-, C-, and E-types are found in chlorite peridotites from Almklovdalen, southwest Norway. Using FTIR spectroscopy, we found that samples with B- and E-type olivine LPOs contain water (170–310 ± 30 ppm H/Si). This water content of olivine is thought to be the minimum water content because water might have been lost due to the fast hydrogen diffusion in olivine (Mackwell and Kohlstedt, 1990). Our result that both B- and E-type olivine LPOs are found in a wet olivine is consistent with the result of previous experimental studies (Jung and Karato, 2001b; Jung et al., 2006; Katayama et al., 2004; Katayama and Karato, 2006). Wang et al. (2013) also reported olivine LPOs such as A-, B-, and E-type in Almklovdalen peridotites, with smaller amounts of water in the olivine (10–180 ppm H/Si). We plotted A- and E-type olivine LPOs in terms of water content and stress (Jung et al., 2006) (Fig. 12a), where our data are located near the fabric boundary between A- and E-type. Because the former fabric diagram in terms of water content and stress (Jung et al., 2006) was based on much higher temperature condition (1470–1570 K) than the peridotites we studied (962–1181 K), we plotted our data of B- and C-type olivine LPOs in the diagram of B-/C- fabric transition (Katayama and Karato, 2006; Skemer et al., 2006) at lower temperature (Fig. 12b), where our data was fitted to the stress-temperature field with the data of previous studies. Furthermore, garnet and chlorite percentage between samples were also correlated with olivine LPO types. Chlorite was abundant in samples showing B- and E-types of olivine LPO, representing wet conditions (Table 1). A sample showed A-type olivine LPO under dry condition with abundant garnet and little amount of chlorite (Table 1).

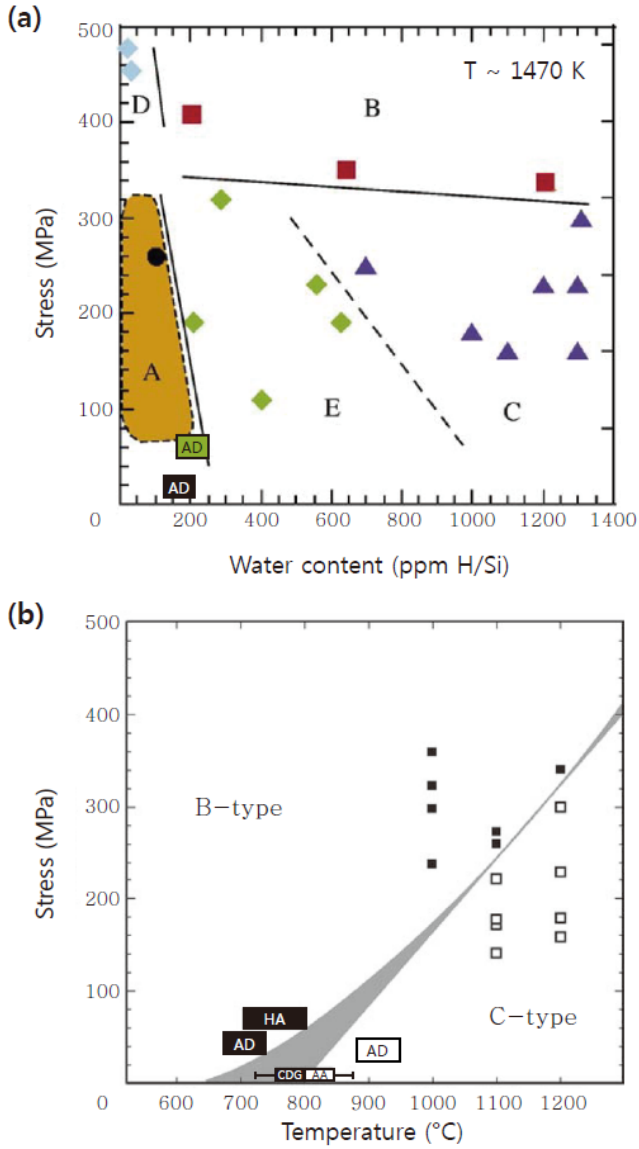

Figure 12. (a) Olivine fabric diagram in terms of water content and stress, modified after Jung et al. (2006). AD represents Almklovdalen specimen in this study. AD in black rectangle represents the data of the A-type olivine LPO of Almklovdalen. AD in green rectangle represents the data of the E-type olivine LPO of Almklovdalen. **(b)** Olivine fabric diagram of B-/C-type LPO transition, modified after Skemer et al. (2006). Solid squares are the data from deformation experiments that formed B-type fabrics, and open squares that formed C-type fabrics (Katayama and Karato, 2006). HA, Higashi Akaishi peridotites with B-type olivine LPO (Mizukami et al., 2004); CDG, Cima di Gagnone (Skemer et al., 2006); and AA, Alpe Arami (Skemer et al., 2006). AD in a black rectangle represents the data of the B-type olivine LPO of Almklovdalen in this study. AD in a white rectangle represents the data of the C-type olivine LPO of Almklovdalen in this study.

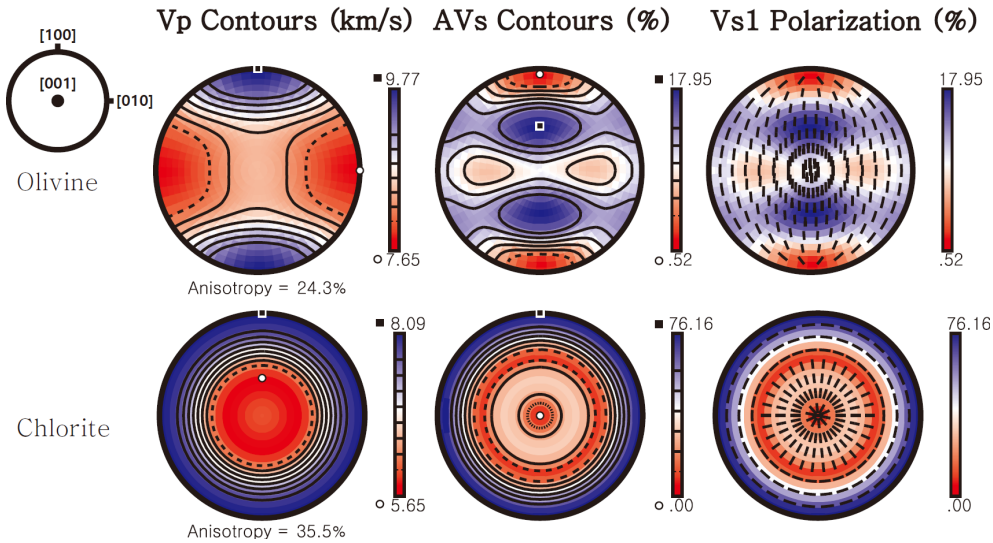

Figure 13. Seismic velocity and anisotropy for a single crystal of olivine and chlorite, presented in the lower hemisphere using an equal-area projection. The P-wave velocity (Vp), amplitude of S-wave anisotropy (AVs), and the polarization direction of the fast S-wave (Vs1) are plotted. The center of the pole figure represents the [001] axis, the E-W direction represents the [010] axis, and the N-S direction represents the [100] axis.

The LPO of chlorite has not been studied much. Puelles et al. (2012) reported only one chlorite LPO so far from a specimen in NW Spain, which showed [001] axes aligned subnormal to the foliation, which is similar to the chlorite LPO that we found in this study. Two samples (435 and 436) showed [001] axes are strongly aligned subnormal to the foliation, with a weak girdle subnormal to the lineation, and [100] axes aligned subparallel to the lineation. Seismic anisotropy of single-crystal chlorite and olivine is shown in Figure 13. Both P- and S-waves propagate slowly along the [001] axis of chlorite, but propagate fast along both the [100] and [010] axes. Both P-wave and S-wave anisotropies of single-crystal chlorite are very high, up to Vp = 35.5% and AVs = 76.2%, respectively (Fig. 13) as previously reported (Mainprice and Ildefonse, 2009). Therefore, the formation of strong LPO of [001] axes in chlorite (Fig. 6) can produce significant seismic anisotropy: P-

wave anisotropy up to 21.1% and S-wave polarization anisotropy up to 31.7% (Fig. 8a)

Olivine from Almklovdalen peridotites showed that A- and E-type olivine LPOs (samples 434, 437, and 438) have a Vs1 polarization direction subparallel to the lineation for vertically propagating S-waves (Fig. 7). The B-type olivine LPO (samples 435 and 436) showed a Vs1 polarization direction subnormal to the lineation (Fig. 7), which may be responsible for trench-parallel seismic anisotropy in the subduction zone (Jung and Karato, 2001b). However, the strength of the olivine LPO in this study was low, with an M-index of M = 0.035–0.069 (Table 1), resulting in a low seismic anisotropy of olivine only up to Vp = 3.8% and AVs = 2.7% (Fig. 7). In contrast, we found that the chlorite had developed a strong LPO, with a high M-index of M = 0.082–0.099 (Table 1), which produced a very strong seismic anisotropy of up to Vp = 21.1% and AVs = 31.7% (Fig. 8a) for the sample with 34% chlorite. Previous study on the LPO of serpentinite showed that a sample with 40% antigorite produced a strong seismic anisotropy of up to Vp = 23.6% and AVs = 23.2% (Jung, 2011), indicating that chlorite produces a similar Vp anisotropy to serpentine, but much higher AVs anisotropy than serpentine (antigorite).

Considering application of current chlorite fabric in the (meta)peridotites to the mantle wedge or the mantle part of the subducting slab, important factors for developing fabrics of minerals are deformation mechanism and deformation conditions such as pressure, temperature, stress, water, etc. If a rock is deformed under the same deformation mechanism and deformation condition, then the rock

fabric developed in one locality can be applied to the one developed in the other locality. Olivine and chlorite fabrics in the present study were developed in the meta-peridotite of HP-UHP metamorphic locality, the WGR of Norway. As we mentioned in the text, chlorite has a wide stability field at high-pressure and high-temperature conditions (Fumagalli and Poli, 2005; Till et al., 2012) so that chlorite peridotite can be present in the mantle wedge and in the mantle part of the subducting slab (Hacker et al., 2003b). Since deformation mechanism and deformation conditions of minerals in HP-UHP belt are considered to be similar to those in the part of mantle wedge and subducting slab, we believe that current data of chlorite and olivine fabrics can be applicable to the mantle fabrics.

Even though slab temperature, oblique subduction of slab, and trench rollback could affect mantle flow direction in subduction zones. 2-D corner flow was assumed in this study for simplicity. Rocks of slab surface and inside of slab could be assumed to experience simple shear. Therefore, foliation of rocks in subducting slabs was considered as planar structure parallel to slab plane with dip angle θ. Figure 14 show the change of the polarization direction of the fast S-wave with a dip angle θ, using the chlorite LPO of sample 436. For the shallow dip angle ($\theta \leq 45°$), the polarization direction of the fast S-wave (Vs1) is subparallel to the flow direction, which can cause trench-normal seismic anisotropy in subduction zone. On increasing θ, the blue band where Vs1 polarization anisotropy is high rotates, and the polarization direction of the fast S-wave (Vs1) becomes subnormal to the lineation (flow direction). This is very important because this feature can be used to explain a strong trench-parallel seismic anisotropy in subduction zones (Fig. 15).

Figure 15 shows a schematic view of the stability field of chlorite in subduction zone based on previous experimental and modelling studies (Fumagalli and Poli, 2005; Hacker et al., 2003b; Till et al., 2012) and also illustrates the signature of seismic anisotropy in a subduction zone that can be caused by the LPO of chlorite. For the low dipping angle ($\theta \leq 45^{o}$) of slab in subduction zone (Fig. 15a), LPO of chlorite will cause trench-normal seismic anisotropy for the vertically propagating fast S-waves. For example, the Juan de Fuca slab under the Cascadia subduction zone is dipping at low angle and the trench-normal seismic anisotropy observed under Oregon (Currie et al., 2004; Park et al., 2004; Wagner et al., 2013) may be attributed to the LPO of chlorite. In addition, the trench-normal seismic anisotropy observed in NE Japan with a low dipping angle of slab ($\theta < 45^{o}$) (Huang et al., 2011b) may also be caused by the LPO of chlorite in the mantle wedge. Recently, a trench-parallel seismic anisotropy was observed in a limited area under Oregon using the Rayleigh waves (Wagner et al., 2013) where source area of the trench-parallel seismic anisotropy includes the nose of 2-D corner flow. In this area, chlorite can be stable (Hacker et al., 2003b; Till et al., 2012) and the dip angle of the flow of chlorite peridotite in this area is high (Fig. 15a) so that the trench-parallel seismic anisotropy observed in the limited area (Wagner et al., 2013) may be attributed to the LPO of chlorite. In contrast, for the high dipping angle ($\theta > 50^{o}$) of slab in subduction zone (Fig. 15b), LPO of chlorite will cause trench-parallel seismic anisotropy for the vertically propagating fast S-waves. For example, slab under both Tonga and Mariana is dipping at high angle and a strong trench-parallel seismic anisotropy was observed under the fore-arc and arc area (Pozgay et al., 2007; Smith et al., 2001), which may be attributed to the LPO of chlorite in addition to the B-type LPO of olivine in the mantle wedge. Figure 15c illustrates

the change of seismic anisotropy when a dipping angle of slab in a subduction zone changes from low to high angle. In this case, LPO of chlorite is supposed to cause a change in seismic anisotropy from the trench-normal anisotropy in the low-angle subduction zone to the trench-parallel anisotropy in the high-angle subduction zone. It is very interesting to observe similar change of the seismic anisotropy from trench-normal to trench-parallel in Nicaragua subduction zone (Abt et al., 2009), where dipping angle of slab in Nicaragua changes from low to high angle, moving from fore-arc to back-arc area.

6. Conclusion

Various olivine LPO types (A-, B-, C-, E-) were found in chlorite peridotites in Almklovdalen (Fig. 5). FTIR spectroscopy of the olivine revealed that the A-type olivine LPO is found in dry condition, whereas the B-type olivine LPO is found in wet condition. This result is consistent with former experimental studies (Jung and Karato, 2001b; Jung et al., 2006; Katayama and Karato, 2006). The highest olivine water content in the samples was 340 ± 30 ppm H/Si, which belonged to a sample with a B-type olivine LPO (Fig. 10). It is found that the LPO of olivine is relatively weak, whereas the LPO of chlorite is very strong. The LPO of chlorite showed [001] axes strongly aligned subnormal to the foliation, with a weak girdle subnormal to the lineation. Since chlorite is much more anisotropic elastically than olivine (Fig. 13), seismic anisotropy of chlorite LPOs showed much higher anisotropy than that in olivine LPOs. Adding the seismic anisotropy of chlorite to that of olivine, the seismic anisotropy of a whole rock was increased up to Vp = 8.3% and AVs = 13.1% (Fig. 8b). In addition, it is found that increasing the dip

angle (θ) of a slab in a subduction zone highly rotates the polarization direction of the fast S-wave (Figs. 14 and 15), resulting in the polarization direction of the fast S-wave subnormal to the lineation (flow direction) with increasing dip angle, which can explain trench-parallel seismic anisotropy in a high-angle subduction zone. Because chlorite has a wide stability field at high pressure and high temperature in a mantle wedge and in a subducting slab (Fumagalli and Poli, 2005; Hacker et al., 2003b; Padrón-Navarta et al., 2010; Till et al., 2012; van Keken et al., 2011; Wada et al., 2012), the strong LPO of chlorite can be a source of the observed trench-normal or trench-parallel seismic anisotropy in the mantle wedge (Currie et al., 2004; Huang et al., 2011b; Long and Silver, 2008; Park et al., 2004; Pozgay et al., 2007; Smith et al., 2001; Wagner et al., 2013) as well as in subducting slabs (Wagner et al., 2013; Wang and Zhao, 2013) depending on the dipping angle of slab in a subduction zone where chlorite is stable.

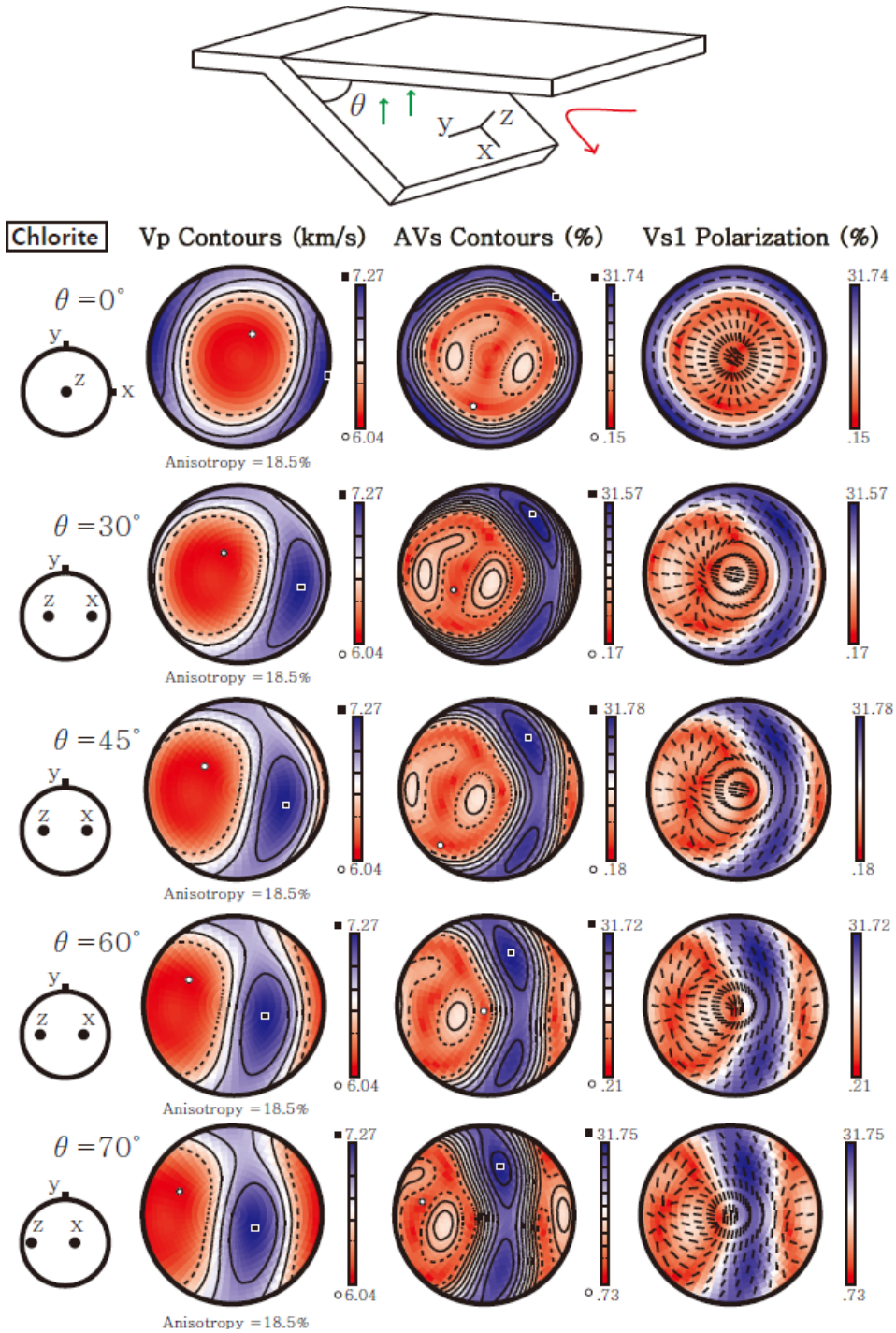

Figure 14. Effect of dip angle (θ) on the seismic anisotropy of chlorite (sample 436). In the cartoon, green arrows represent vertically propagating S-waves. The red arrow represents mantle flow direction. The P-wave velocity (Vp), amplitude of S-wave anisotropy (AVs), and the polarization direction of the fast S-wave (Vs1) are plotted. The plots are shown in equal-area and lower-hemisphere projections. The x and z directions represent the lineation

and the direction normal to the foliation, respectively. θ shows the eastward dip angle of the subducting slab. Horizontal flow occurs when θ = 0°. The polarization direction of the vertically propagating fast S-wave (Vs1) is shown at the center of the pole figure.

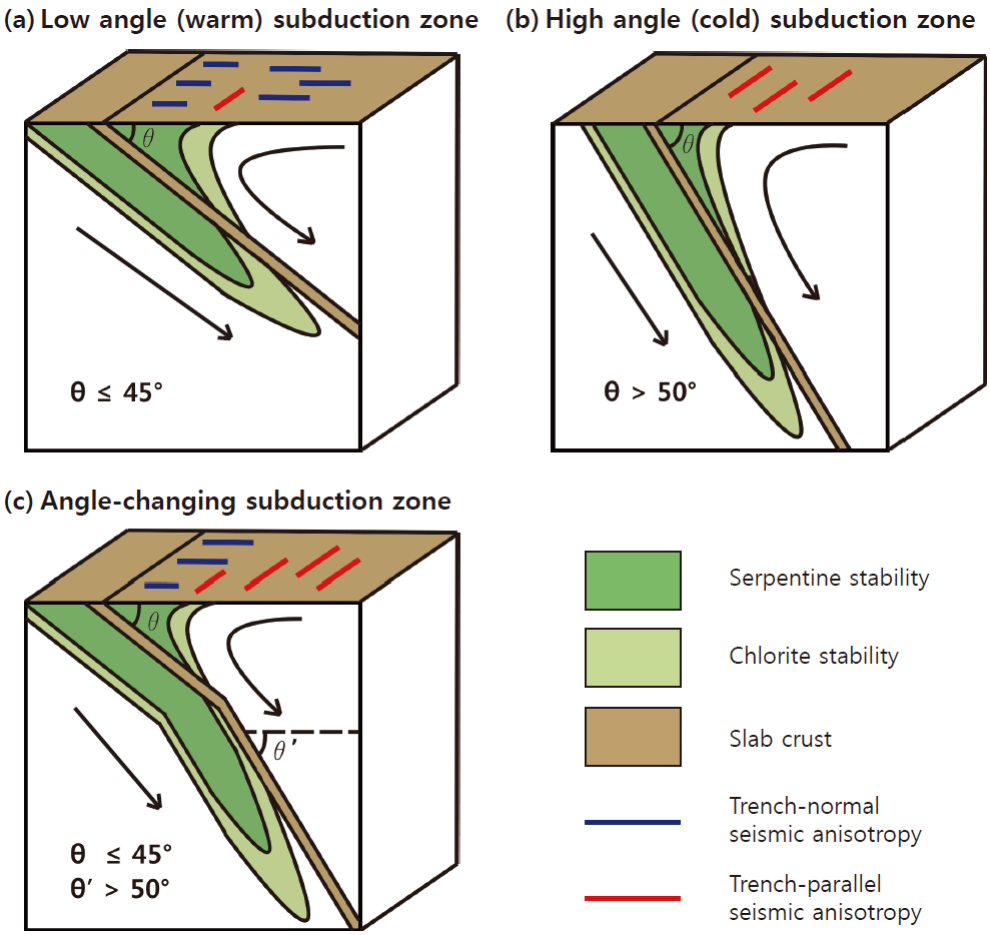

Figure 15. Schematic diagram showing the effect of the dipping angle of the slab on the seismic anisotropy caused by the LPO of chlorite, assuming 2-D corner flow. **(a)** Trench-normal seismic anisotropy in the low-angle subduction zone (θ ≤ 45º). **(b)** Trench-parallel seismic anisotropy in the high-angle subduction zone (θ > 50º). **(c)** Change in the seismic anisotropy corresponding to the change in the dipping angle of the slab. Blue and red bars represent trench-normal and trench-parallel seismic anisotropy of the fast S-wave, respectively. **(a)** Low-angle (warm) subduction zone. **(b)** High-angle (cold) subduction zone. **(c)** Angle-changing subduction zone.

CHAPTER 3: Strain-induced fabric transition of chlorite and implications for seismic anisotropy in subduction zones

**** This chapter has been modified from a published paper:***

Kim, D., Jung, H., and Lee, J., 2020, Strain-induced fabric transition of chlorite and implications for seismic anisotropy in subduction zones: Minerals, v. 10, no. 6, p. 503.

Abstract

Seismic anisotropy of S-wave, trench-parallel or trench-normal polarization direction of fast S-wave, has been observed in the fore-arc and back-arc regions of subduction zones. Lattice preferred orientation (LPO) of elastically anisotropic chlorite has been suggested as one of the major causes of seismic anisotropy in subduction zones. However, there are two different LPOs of chlorite reported based on the previous studies of natural chlorite peridotites, which can produce different expression of seismic anisotropy. The mechanism for causing the two different LPOs of chlorite is not known. Therefore, we conducted deformation experiments of chlorite peridotite under high pressure-temperature conditions (P = 0.5–2.5 GPa, T = 540–720 °C). We found that two different chlorite LPOs were developed depending on the magnitude of shear strain. The type-1 chlorite LPO is characterized by the [001] axes aligned subnormal to the shear plane, and the type-2 chlorite LPO is characterized by a girdle distribution of the [001] axes subnormal to the shear direction. The type-1 chlorite LPO developed under low shear strain (γ

≤ 3.1±0.3), producing trench-parallel seismic anisotropy. The type-2 chlorite LPO developed under high shear strain ($\gamma \geq 5.1 \pm 1.5$), producing trench-normal seismic anisotropy. The anisotropy of S-wave velocity (AVs) of chlorite was very strong up to AVs = 48.7% so that anomalous seismic anisotropy in subduction zones can be influenced by the chlorite LPOs.

Keywords: lattice preferred orientation, chlorite, seismic anisotropy

1. Introduction

Trench-parallel seismic anisotropy of S-wave has been observed in the fore-arc mantle wedge and subducting slab of many subduction zones (Long, 2013; Long and Silver, 2008; Nakajima and Hasegawa, 2004; Park and Levin, 2002; Savage, 1999; Schulte-Pelkum et al., 2005; Smith et al., 2001). Previous studies suggest that possible causes for trench-parallel fast polarization of seismic anisotropy of S-wave are the B-type olivine LPO in the hydrated mantle wedge (Behr and Smith, 2016; Cao et al., 2017; Jung and Karato, 2001b; Kang and Jung, 2019; Karato et al., 2008; Katayama and Karato, 2006; Kneller et al., 2007; Long and Silver, 2009; Michibayashi et al., 2007; Mizukami et al., 2004; Ohuchi et al., 2011; Park and Jung, 2015; Skemer et al., 2006; Tasaka et al., 2008; Wang and Zhao, 2013), pressure-induced olivine LPO (Jung et al., 2009b; Lee and Jung, 2015; Ohuchi et al., 2011), spatial distribution of faults in the hydrated slab (Faccenda et al., 2008), trench-parallel flow in the sub-slab mantle (Russo and Silver, 1994) and the mantle wedge (Fischer et al., 1998; Long and Silver, 2008; Peyton et al., 2001; Smith et al., 2001), and the LPOs of hydro-phyllosilicates such as serpentine (Bezacier et al., 2010; Boudier et al., 2010; Brownlee et al., 2013; Hirauchi et al., 2010; Ji et al., 2013; Jung, 2011; Katayama et al., 2009; Nishii et al., 2011; Watanabe et al., 2011), chlorite (Kang and Jung, 2019; Kim and Jung, 2015) and talc (Lee et al., 2020). In contrast, trench-normal seismic anisotropy has been observed in the back-arc area of subduction zones (Fischer et al., 1998; Huang et al., 2011a, b; Nakajima and Hasegawa, 2004; Smith et al., 2001), which has been interpreted as a change in olivine LPO in the back-arc area (Karato et al., 2008; Katayama and Karato, 2006; Kneller et al., 2005).

However, seismic anisotropy observed in some fore-arc subduction zones, such as Ryukyu and Cascadia, cannot be explained solely by the olivine LPOs (Long and van der Hilst, 2006; McCormack et al., 2013; Wagner et al., 2013). McCormack et al. (2013) found a thin layer (~6 km) of strong anisotropy (~10–14%) beneath Ryukyu with a slow axis of symmetry directly above the slab; this cannot be explained solely by the olivine LPO. In addition, Wagner et al. (2013) found trench-parallel seismic anisotropy beneath Cascadia using Rayleigh waves, and suggested that hydrous minerals in the mantle wedge or in the slab may also be responsible for the observed trench-parallel seismic anisotropy.

Chlorite is one of the elastically highly anisotropic hydrous minerals (Mainprice and Ildefonse, 2009; Mookherjee and Mainprice, 2014) with a wide stability field under high pressure and temperature (P-T) conditions in subduction zones (Fumagalli and Poli, 2005; Hacker et al., 2003b; Schmidt and Poli, 1998; van Keken et al., 2011; Wada et al., 2012) (Fig. 16). Chlorite is stable as chlorite peridotite in the lower part of the mantle wedge and subducting slab (Fumagalli and Poli, 2005; van Keken et al., 2011; Wada et al., 2012). The deformation of chlorite and formation of its LPO during subduction processes can cause large seismic anisotropy (Jung, 2017; Kim and Jung, 2015). However, the development of the chlorite LPO under high P-T conditions is poorly understood, and limited studies exist on the LPOs of only naturally deformed chlorite (Kang and Jung, 2019; Kim and Jung, 2015; Morales et al., 2013; Padrón-Navarta et al., 2015; Puelles et al., 2012; Wallis et al., 2015). Two types of chlorite LPOs have been reported (Fig. 17). The chlorite [001] axes align subnormal to the foliation, and the other poles of (110) and (010) are aligned subparallel to the foliation (Kang and

Jung, 2019; Kim and Jung, 2015; Morales et al., 2013; Puelles et al., 2012). This structure was defined as the type-1 LPO of chlorite (Jung, 2017). In contrast, the chlorite [001] axes align not only subnormal to the foliation but also subnormal to the lineation on the foliation (Kim and Jung, 2015; Padrón-Navarta et al., 2015; Wallis et al., 2015), which defines the type-2 LPO of chlorite. The two different types of chlorite LPOs can produce different seismic anisotropy (Kim and Jung, 2015) and therefore, the applicability of the chlorite LPO for the interpretation of seismic anisotropy is ambiguous.

In nature, the mode of deformation in the subducting slab is most likely simple shear. Therefore, to understand the development of two different LPOs of chlorite we conducted deformation experiments of chlorite peridotite in simple shear under high P-T conditions, providing the mechanism for the development of the two different types of chlorite LPOs and the resultant seismic anisotropy.

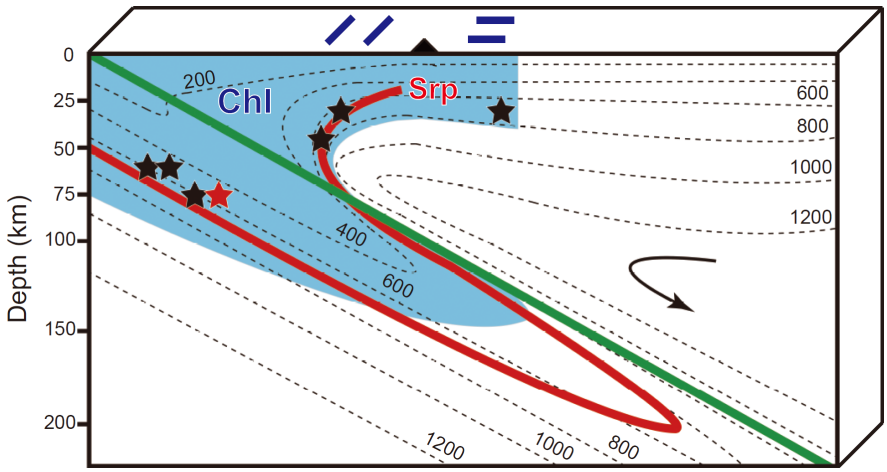

Figure 16. Chlorite stability field in subduction zones. Stability field of chlorite (blue area) and serpentine (red line) in subduction zones (modified after Schmidt and Poli (1998)). The green line represents the top of the subducting slab and the dashed lines are isotherms. Black arrow indicates the flow line in the mantle wedge. Blue bars at the top represent the polarization directions of the fast S-wave, showing trench-parallel or trench-normal seismic anisotropy observed in subduction zones (Fischer et al., 1998; Long, 2013; Long and Silver, 2008; Nakajima and Hasegawa, 2004; Park and Levin, 2002; Savage, 1999; Smith et al., 2001). Black and red stars indicate the experimental conditions in this study. Chl: chlorite; Srp: serpentine.

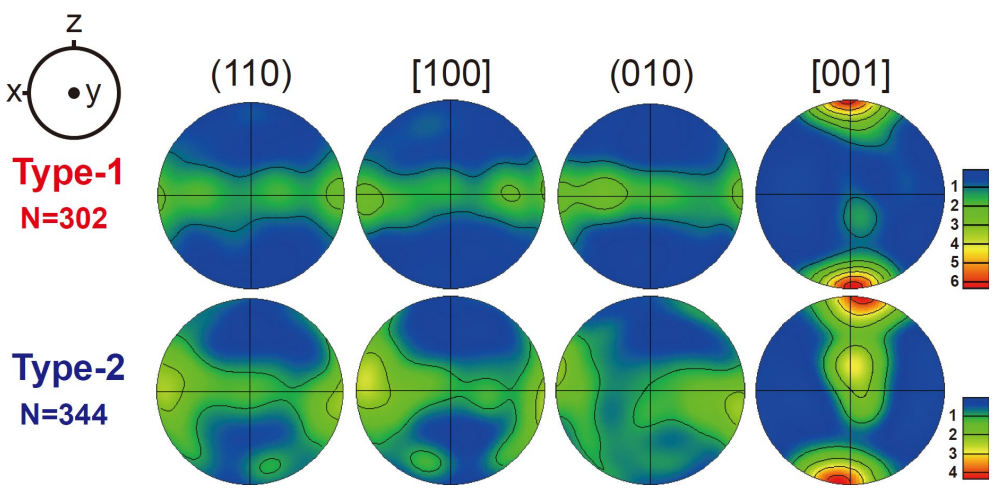

Figure 17. Pole figures of chlorite observed in natural samples showing two different types of LPOs (Kim and Jung, 2015). Pole figures are presented in the lower hemisphere using an equal-area projection. N represents the number of grains, and a half-scatter width of 30° was used for the contours. The rounded contours in the pole figure represent the multiples of uniform distributions (m.u.d.), showing a fabric strength. x: lineation direction; z: direction normal to the foliation.

2. Materials and methods

The starting material was chlorite peridotite (Fig. 18) sourced from Almklovdalen, in the Western Gneiss Region, southwest Norway. The chlorite peridotite of starting material showed the bulk composition of olivine (60%), chlorite (31%), orthopyroxene (5%), clinopyroxene (3%), and garnet (1%). The chemical composition of chlorite was clinochlore of composition $(Mg_{4.6}Fe^{2+}_{0.3}Cr_{0.1})Al(Si_3Al)O_{10}(OH)_8$ (Table 4). A JEOL JXA-8900R EPMA at the NCIRF at SNU was used to analyze chemical composition of the starting material. For the EPMA setting, the acceleration voltage was 15 kV, working distance was 10 mm, current probe was 20 nA, and beam diameter was 3 μm. Peak time was 10 seconds for Na and K, and 20 seconds for other elements. Background time was 5 seconds for Na and K, and 10 seconds for other elements.

Simple shear experiments were conducted using a modified Griggs apparatus at the Tectonophysics Laboratory, SEES in SNU. Figure 19 shows the sample assembly. The samples were core-drilled with a diameter of 3.1 mm. Core-drilled sample were cut at 45° to the foliation. The samples were then placed between two alumina pistons inside a nickel capsule, and the foliation of starting material was aligned parallel to σ_1 direction to minimize the effect of preexisting chlorite LPO of starting material (Fig. 19). Nickel foil was inserted in the middle of the sample—perpendicular to the shear plane—to measure the shear strain. Weak CsCl and NaCl were used as pressure mediums. The temperature was measured by two thermocouples (Pt-30% Rh-70% and Pt-6% Rh-94%). The confining pressure was increased in 12 h and the temperature was increased within 1 h. Samples were

deformed under constant strain rates of 2.7–9.7×10^{-6} s^{-1} (Table 5). After each deformation experiment, the sample was quenched to room temperature by shutting off the power and decreasing the pressure in 12 h.

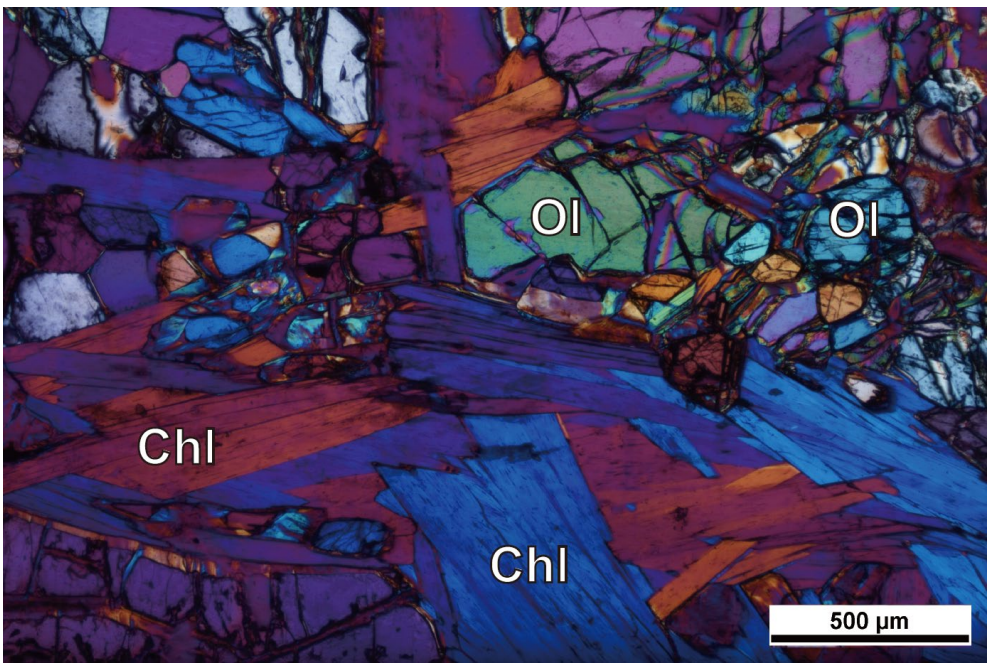

Figure 18. Optical photomicrograph of starting material (chlorite peridotite) in cross-polarized light with λ plate inserted. Natural chlorite peridotite from Almklovdalen, southwest Norway (sample 436 of Kim and Jung (2015)) was used for the experiments in this study. Chl: chlorite; Ol: olivine.

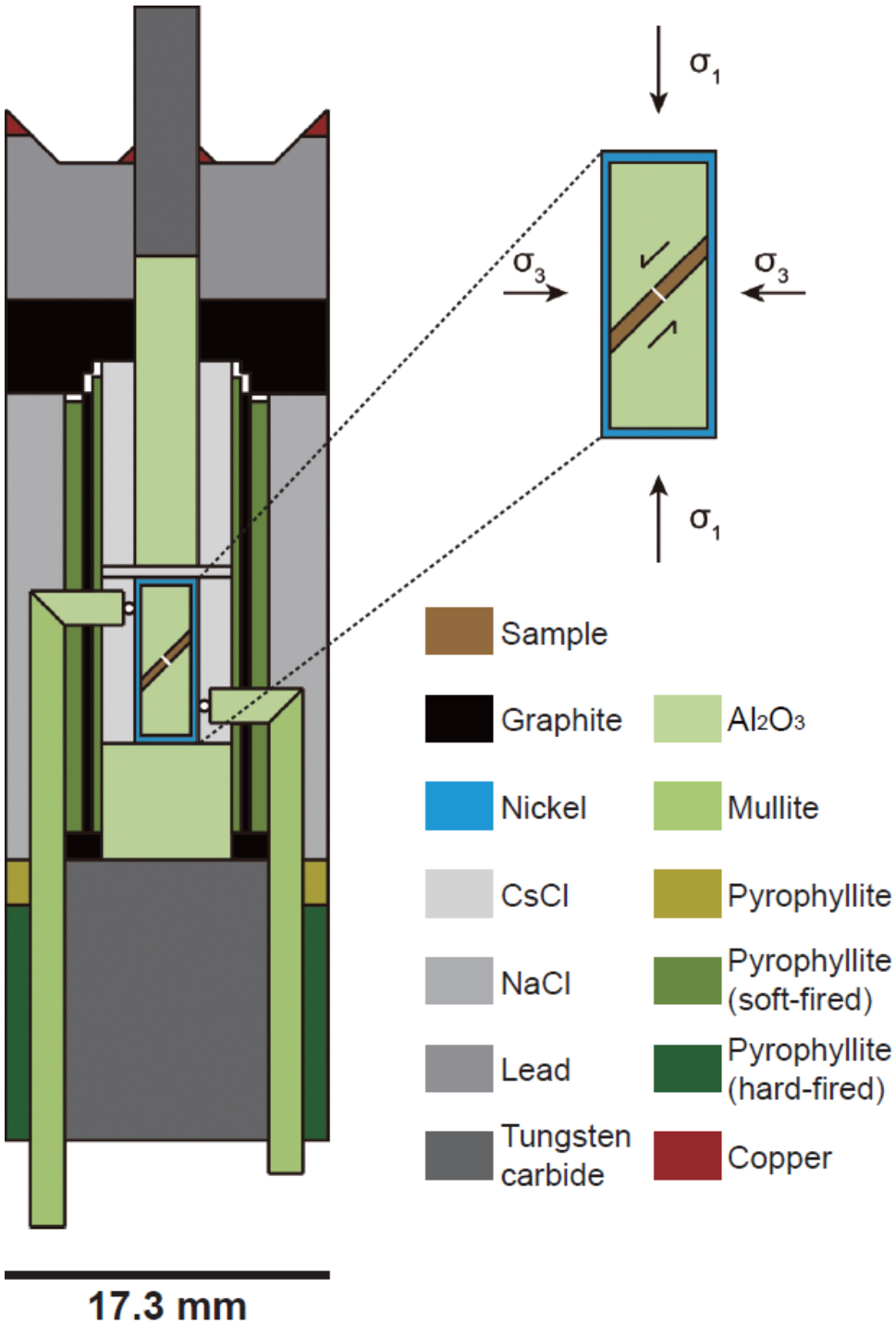

Figure 19. Sample assembly for deformation experiments of chlorite peridotite. Deformation experiments were conducted in simple shear using a modified Griggs apparatus under high P-T conditions. Nickel foil was inserted in the middle of the sample—perpendicular to the shear plane—to measure the shear strain. σ_1 and σ_3 represent the maximum and minimum principal stresses, respectively.

Table 4. Chemical composition of starting material minerals.

wt.% Oxides	Olivine[1]	Chlorite[1]	Pyroxene[1]
SiO_2	40.33	31.12	51.80
TiO_2	0.02	0.04	0.12
Al_2O_3	0.02	17.70	4.97
Cr_2O_3	0.02	1.45	0.89
FeO	13.18	3.99	2.67
MnO	0.21	0.04	0.04
MgO	47.51	31.75	16.75
CaO	0.01	0.02	20.27
Na_2O	0.02	0.01	1.58
K_2O	0.01	0.01	0.03
NiO	0.51	0.27	0.09
Sum[2]	101.77	86.36	99.16
O=12			
Si	2.967	2.554	3.786
Ti	0.001	0.002	0.006
Al	0.001	1.712	0.429
Cr	0.001	0.094	0.051
Fe^{2+}	0.811	0.274	0.164
Mn	0.013	0.003	0.003
Mg	5.209	3.884	1.826
Ca	0.001	0.002	1.587
Na	0.003	0.001	0.224
K	0.001	0.001	0.002
Ni	0.030	0.018	0.005
Cations	9.034	8.542	8.080

[1]The average of three EPMA measurements for each mineral.

[2]Includes uncertainty of ±1.5%.

Experimental specimens were cut along the x-z plane (x: shear direction, z: normal to the shear plane). They were carefully polished using alumina powders, 1 μm diamond paste, and Syton 0.06 μm colloidal silica for 8 h to remove mechanical damage. The polished sample was observed using a JEOL JSM-7100F field-emission scanning electron microscope (FE-SEM) housed at the SEES in SNU. Chlorite grain thickness was measured with the BEIs magnified up to 16,000× using the FE-SEM. The chemical composition of the dehydration products was determined using an EDS in the JEOL JSM-7100F FE-SEM at the SEES in SNU.

The LPOs of chlorite and olivine were determined using EBSD, which was attached to the JEOL JSM-6380 SEM at SEES. The accelerating voltage was 20 kV and the working distance was 15 mm in the SEM for the EBSD analysis. The HKL EBSD system with channel 5 software was used to index the EBSD patterns. The EBSD patterns of each grain was analyzed manually to ensure correct indexing with a MAD less than 1°. The fabric strength of the LPO was determined using the misorientation index (M-index) (Skemer et al., 2005). The M-index ranges from 0 (random fabric) to 1 (single crystal or complete alignment). Because of manual analysis for accurate data, the numbers of EBSD data in this study were smaller than those of automated mapping (Cao et al., 2020; Park and Jung, 2020). However, according to the previous study (Skemer et al., 2005), minimum number of grains for a meaningful fabric strength and LPO is N = 150. Numbers of grain for EBSD data in this study were over meaningful 150 for each experimental sample.

The seismic anisotropy of chlorite and olivine was calculated from the LPO

data of experimentally deformed chlorite and olivine using the ANIS2k and VpG programs from Mainprice (1990), using chlorite elastic constants for the P = 1.8 GPa condition from Mookherjee and Mainprice (2014). However, the observed seismic anisotropy in the subduction zone may be caused by the mixture of the LPOs of olivine, chlorite, and serpentine in the path of seismic propagation. Therefore, seismic anisotropy of the mixture of the olivine and chlorite LPOs, and the mixture of the chlorite and serpentine LPOs were calculated, using the olivine elastic constants from Abramson et al. (1997) and the serpentine elastic constants from Bezacier et al. (2010). Because of the absence of serpentine in our specimen, we used the LPO data of serpentine (VM3) from previous study (Jung, 2011), which showed a well-defined foliation. In the calculation of seismic properties, we arranged the foliation of serpentine identical to the shear plane of experiments. The ANIS2k and VpG programs were used for the calculation of polyphasic seismic anisotropy, which have been qualified over decades (Mainprice, 1990). The delay time (dt) of the S-wave was calculated using the following equation (Pera et al., 2003): $dt = (0.01 \times AVs \times T) / \langle Vs \rangle$, where T is the anisotropic layer thickness, $\langle Vs \rangle$ is the average velocity of the fast and slow shear waves (Vs1 and Vs2, respectively), and AVs is the anisotropy of the S-wave expressed as a percentage.

To understand the stability field of chlorite peridotite in this study we calculated the stability field and the volume percentage of chlorite in the Na_2O-CaO-FeO-MgO-Al_2O_3-SiO_2-H_2O (NCFMASH) model system using Theriak-Domino software (de Capitani and Petrakakis, 2010) with the database of Holland and Powell (2011) (tc55MnNCKFMASH file). Solid solution for the mineral phases includes chlorite (Holland et al., 1998), olivine (Holland and Powell, 1998),

antigorite (Holland and Powell, 1998), diopside (Holland and Powell, 1996), garnet (White et al., 2007), amphibole (Diener and Powell, 2012), orthopyroxene (Powell and Holland, 1999), phlogopite (Holland and Powell, 1998), pargasite (Holland and Powell, 1998), brucite (Holland and Powell, 1998), hercynite (Holland and Powell, 1998), clinohumite (Holland and Powell, 1998), monticellite (Holland and Powell, 1998), vesuvianite (Holland and Powell, 1998), and phase A (Holland and Powell, 1998). The bulk composition was determined by modal composition of starting material and EPMA analysis (Table 4), which is average value of at least three points for each mineral.

Table 5. Experimental conditions and results of experimentally deformed chlorite.

Sample	Pressure (GPa)	Temperature (°C)	LPO type of chlorite	Shear strain	Strain rate (s^{-1})	M-index[1]	AVp[2] (%)	Max. AVs[2] (%)	Max. Delay time[3] (s)
JH101	0.5	650±15	Type-1	3.1±0.3	2.65×10^{-6}	0.479	21.9	42.8	0.4–2.7
JH100	1.0	720±20	Type-1	1.9±0.2	5.48×10^{-6}	0.621	23.6	48.7	0.5–3.0
JH154	2.0	570±10	Type-1	2.2±0.5	6.41×10^{-6}	0.510	20.4	37.0	0.4–2.3
JH156	2.5	540±10	Type-1	1.7±0.2	6.53×10^{-6}	0.534	21.7	42.3	0.4–2.6
JH116	0.5	650±15	Type-2	5.7±1.0	9.68×10^{-6}	0.075	11.0	16.2	0.2–1.1
JH127	1.0	650±15	Type-2	5.1±1.5	6.30×10^{-6}	0.127	17.0	21.6	0.2–1.4
JH138	1.5	650±15	Type-2	6.2±1.7	6.26×10^{-6}	0.256	16.6	21.3	0.2–1.4
JH152	2.5	630±10	Type-2	6.3±1.6	6.51×10^{-6}	0.080	13.2	16.5	0.2–1.1

[1]Fabric strength of chlorite is shown as M-index (Skemer et al., 2005).

[2]AVp: anisotropy of P-wave velocity, AVs: anisotropy of S-wave velocity of chlorite only in the specimen.

[3]Delay time of S-wave velocity considering 5–30 km thick layer of chlorite peridotite (Fumagalli and Poli, 2005; Hacker et al., 2003b; Schmidt and Poli, 1998).

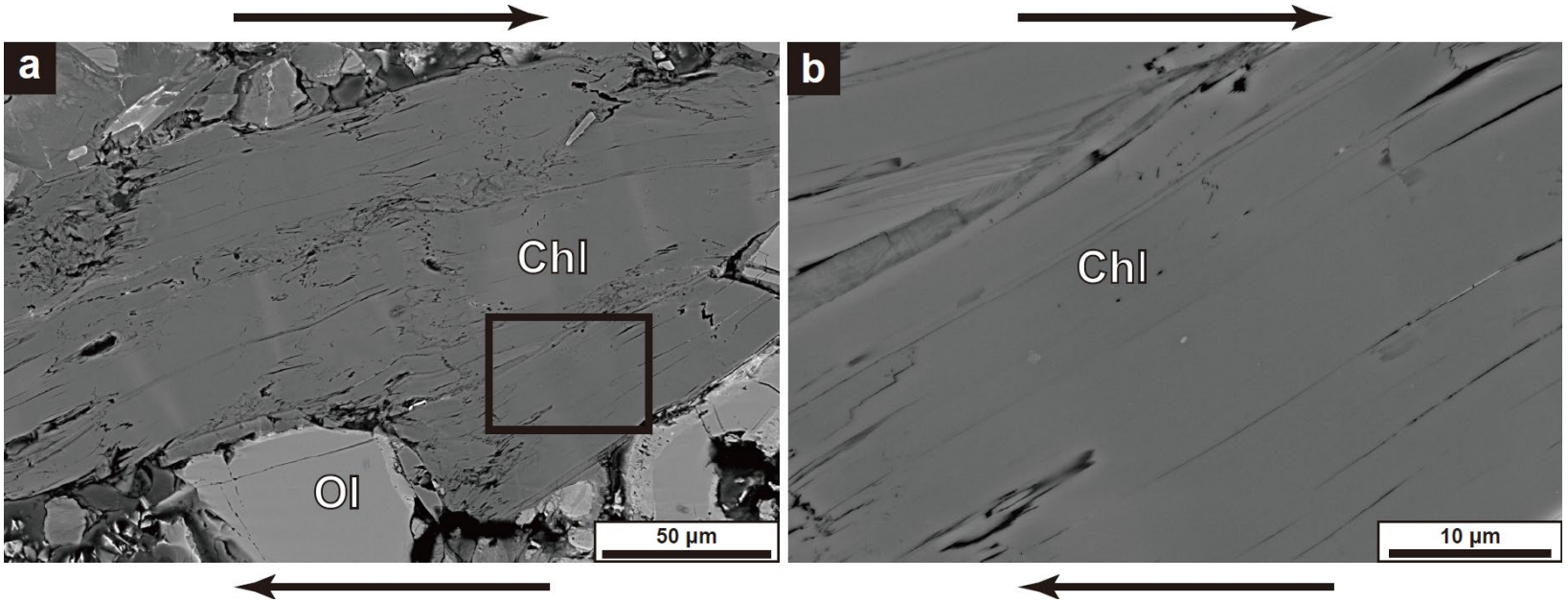

Figure 20. BEIs of deformed sample. **(a)** BEI of experimentally deformed chlorite peridotite (sample JH156) at P = 2.5 GPa and T = 540 °C (red star in Figure 16), taken with an acceleration voltage of 15 kV and a working distance of 10 mm using the JEOL JSM-7100F field-emission scanning electron microscope (FE–SEM). **(b)** Magnified view of the black box in **(a)**, showing deformed chlorites. Horizontal black arrows indicate the dextral shear direction of the experiment. Chl: chlorite; Ol: olivine.

3. Results

3.1. Microstructures

The bulk composition of experimental specimens was olivine (60%), chlorite (35%), pyroxene (4%), and other minor components (1%). An example of deformed chlorite peridotite in simple shear at the pressure of P = 2.5 GPa and temperature of T = 540 °C is shown in Fig. 20. We did not observe phase change with increasing shear strain at any P-T condition. Chlorite grains became thin and showed very strong shape preferred orientation on every experimental specimen in common. They assembled to form chlorite sheets, which was aligned less than about 30° from the shear direction (Table 5 and Fig. 20). Shear strain was localized along the chlorite-rich area. Olivine grains preserved their round shape and had a grain size up to 100 μm (Fig. 20a). Most chlorite grains were thinner than 10 μm, and they became much thinner in the sample deformed at high shear strain (Figs. 20 and 21).

3.2. The LPOs of chlorite

The same starting material was used for every experiment in this study, and chlorite LPO of the starting material is shown at the top of Figure 22. The starting material showed the [001] axes of chlorite aligned about 45° from the experimental shear direction, and other axes of chlorite aligned as a girdle subnormal to the [001] axes (Fig. 22). The pole figure of the starting material is very much different from the LPOs of experimentally deformed chlorite under the same reference frame (Fig. 22). Although the starting material showed initial chlorite fabric, the chlorite LPOs were significantly changed to type-1 LPO of chlorite at the low

shear strain ($\gamma \leq 3.1$) and to type-2 LPO at the high shear strain ($\gamma \geq 5.1$) after deformation experiments (Fig. 22).

Table 5 shows the experimental conditions and the results of the eight experiments conducted under high P-T conditions (P = 0.5–2.5 GPa, T = 540–720 °C) (Fig. 16). Four samples were deformed at low shear strain ($\gamma \leq 3.1 \pm 0.3$) and the other four samples were deformed at high shear strain ($\gamma \geq 5.1 \pm 1.5$) (Table 5). The resulting chlorite LPOs from all eight experiments are shown in Figure 22. Sample JH156, JH100, JH154, and JH101—deformed at a low shear strain ($\gamma \leq 3.1$)—showed a strong chlorite LPO with the [001] axes aligned subnormal to the shear plane (type-1), indicating a dominant slip system of (001)[hk0]. However, sample JH127, JH116, JH138, and JH152—deformed at a high shear strain ($\gamma \geq 5.1$)—showed the [001] axes of chlorite aligned as a girdle with two high concentrations: subnormal to the shear plane and subnormal to the shear direction on the shear plane (type-2), indicating a dominant slip system of (001)[hk0] and additional pencil-glide slip systems. The two chlorite LPO types were developed depending on the magnitude of shear strain (Table 5 and Fig. 22). Regardless of the P-T conditions, samples that were deformed under low shear strain ($\gamma \leq 3.1 \pm 0.3$) showed type-1 LPOs, whereas samples under high shear strain ($\gamma \geq 5.1 \pm 1.5$) showed type-2 LPOs (Table 5 and Fig. 22). Two samples, JH101 and JH116, were deformed under the same P-T conditions (P = 0.5 GPa, T = 650 °C) with different shear strain of γ = 3.1 and 5.7, respectively (Table 5). Sample JH101, under low shear strain, developed a type-1 LPO, whereas sample JH116, under high shear strain, developed a type-2 LPO (Fig. 22). The chlorite fabric strength was presented as a M-index (Skemer et al., 2005), which is very strong for type-1 chlorite LPOs

(M = 0.479–0.621), and relatively weak for type-2 chlorite LPOs (M = 0.075–0.256) (Table 5). The LPOs of olivine in samples JH156 and JH116 were also measured and are shown in Figure 23a.

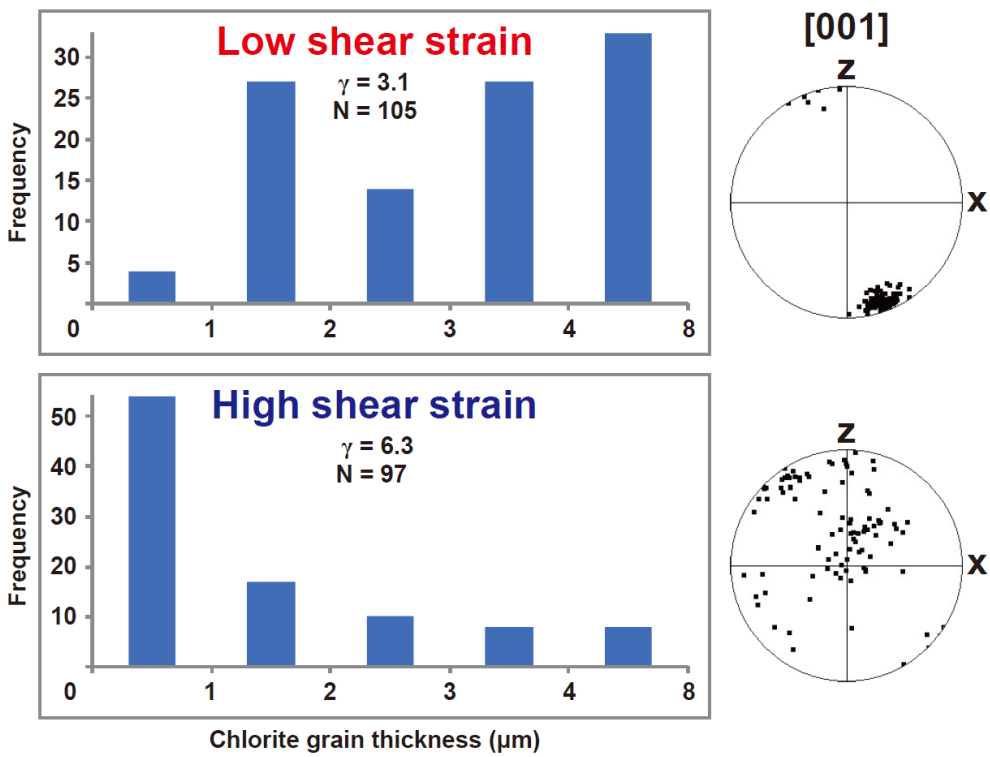

Figure 21. Chlorite grain thickness of two different LPO types of chlorite. Chlorite grain thickness histogram and corresponding pole figures of chlorite [001] axes presented in the lower hemisphere using an equal-area projection. Thickness of 105 chlorite grains of low-shear-strain experiment (sample JH101) and 97 chlorite grains of high-shear-strain experiment (sample JH152) were measured using the BEIs taken from the JSM-7100F FE–SEM. x: shear direction; z: direction normal to the shear plane; γ: shear strain of sample; N: number of grains.

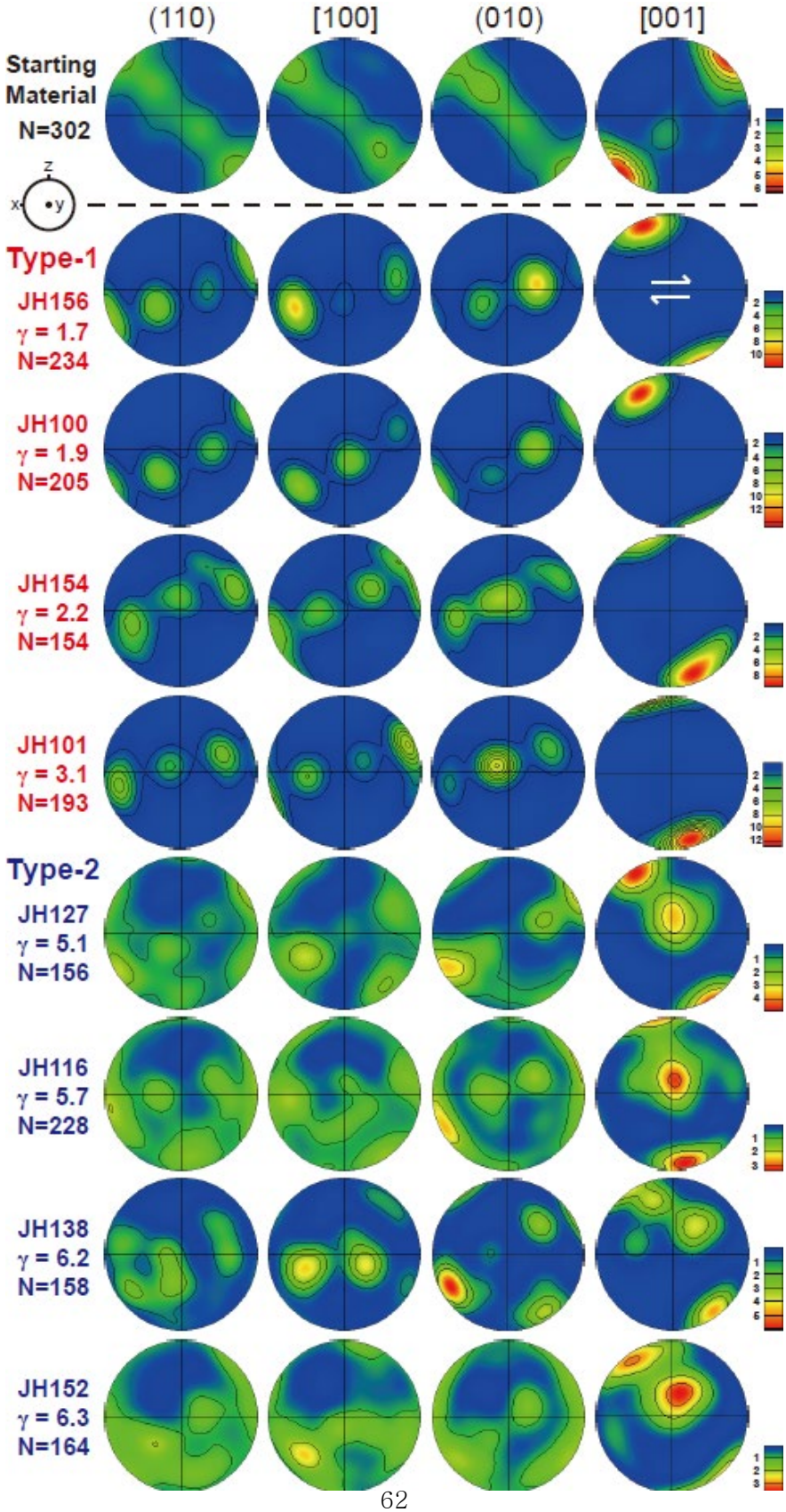
(110)
[100]
(010)
[001]
Starting Material
N=302
z
x
y
Type-1
JH156
γ = 1.7
N=234
JH100
γ = 1.9
N=205
JH154
γ = 2.2
N=154
JH101
γ = 3.1
N=193
Type-2
JH127
γ = 5.1
N=156
JH116
γ = 5.7
N=228
JH138
γ = 6.2
N=158
JH152
γ = 6.3
N=164

Figure 22. Pole figures of experimentally deformed chlorite. Pole figures of chlorite are presented in the lower hemisphere using an equal-area projection. The LPO of chlorite in the starting material is shown at the top. Sample names under low shear strain with the type-1 chlorite LPO are shown as red color, and other sample names under high strain with the type-2 LPO are shown as blue color. White arrows indicate the dextral direction of shear. N represents the number of grains. γ represents the shear strain of experiments, and a half-scatter width of 30° was used for the contours. The rounded contours in the pole figure represent the multiples of uniform distributions (m.u.d.), showing a fabric strength. x: shear direction; z: direction normal to the shear plane.

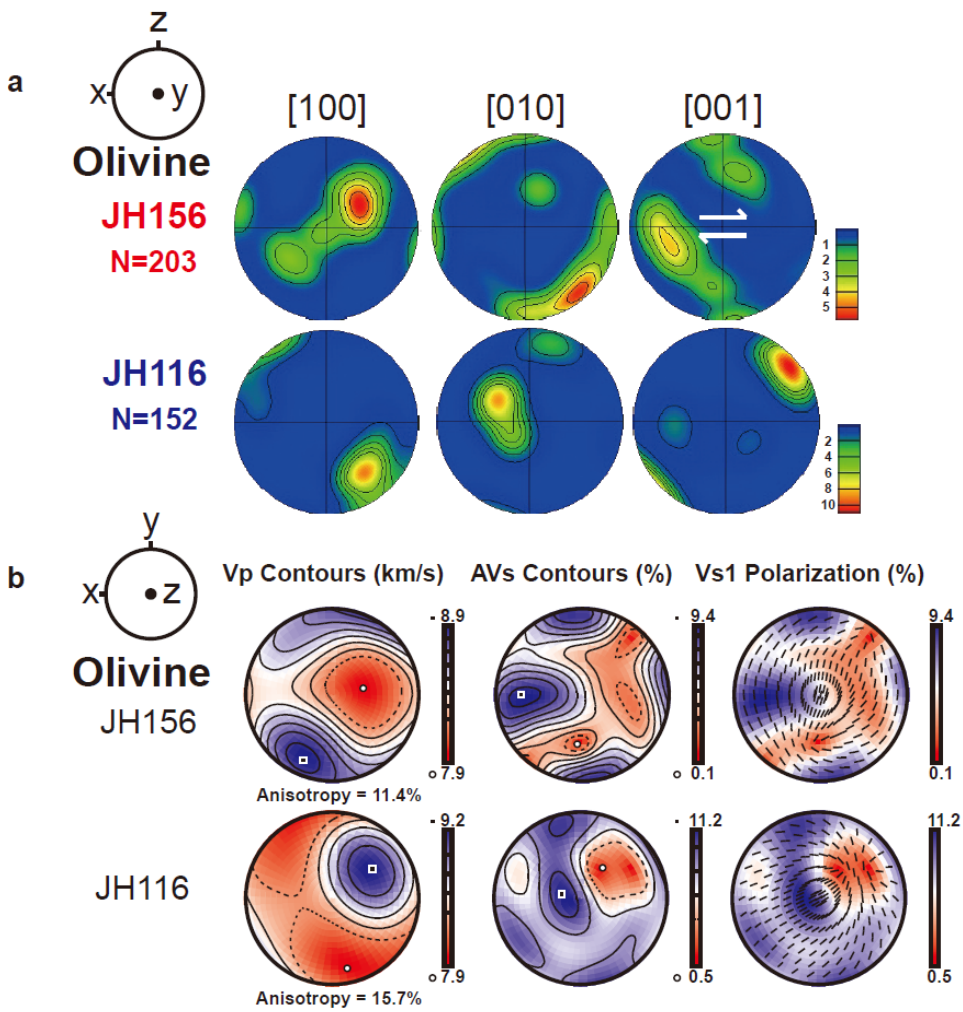

Figure 23. Pole figures and seismic anisotropy of experimentally deformed olivine. **(a)** Pole figures of olivine are presented in the lower hemisphere using an equal-area projection. White arrows indicate the dextral direction of shear. Sample JH156 shows a B-type LPO of olivine (Jung and Karato, 2001b). N represents the number of grains, and a half-scatter

width of 30° was used for the contours. The rounded contours in the pole figure represent the multiples of uniform distributions (m.u.d.), showing a fabric strength. **(b)** Seismic velocity and anisotropy calculated from the LPO of olivine are presented in the lower hemisphere using an equal-area projection. The P-wave velocity (Vp), amplitude of the S-wave anisotropy (AVs), and the polarization of the fast S-wave (Vs1) are plotted. The polarization direction of the vertically propagating fast S-wave (Vs1) is shown as bars at the center of the stereonet. x: shear direction; z: direction normal to the shear plane.

Table 6. Seismic anisotropy and delay time of mineral mixtures.

Sample	Mineral mixture (%)	AVp[1] (%)	Max. AVs[1] (%)	Max. Delay time[2] (s)
JH156	Ol (70) + Chl (30)	13.1	19.3	0.2–1.2
	Ol (100) + Chl (0)	11.4	9.4	0.1–0.6
JH116	Ol (70) + Chl (30)	11.7	12.1	0.1–0.8
	Ol (100) + Chl (0)	15.7	11.2	0.1–0.7
JH100	Chl (25) + Srp (75)[3]	26.2	28.4	0.3–2.0
	Chl (37.5) + Srp (62.5)[3]	25.3	28.7	0.3–2.0
	Chl (50) + Srp (50)[3]	24.7	30.4	0.3–2.1
	Chl (62.5) + Srp (37.5)[3]	24.2	33.4	0.4–2.2
	Chl (75) + Srp (25)[3]	23.9	37.6	0.4–2.4

[1]AVp: anisotropy of P-wave velocity, AVs: anisotropy of S-wave velocity.

[2]Delay time of S-wave velocity considering 5–30 km thick layer of chlorite peridotite (Fumagalli and Poli, 2005; Hacker et al., 2003b; Schmidt and Poli, 1998).

[3]Serpentine LPO of VM3 (Jung, 2011) was used. Ol: olivine; Chl: chlorite; Srp: serpentine.

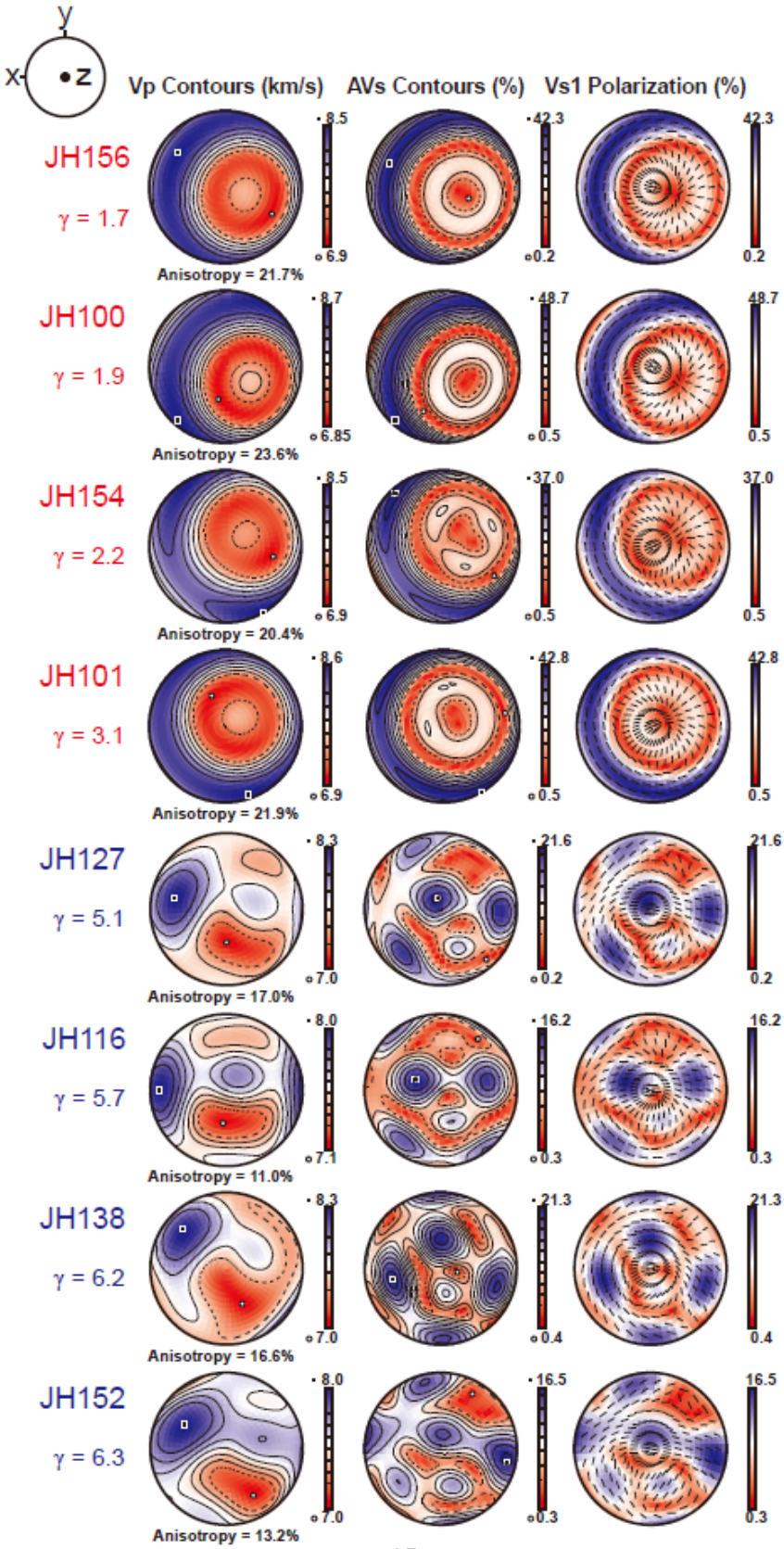
y
x
z
Vp Contours (km/s)
AVs Contours (%)
Vs1 Polarization (%)
JH156
γ = 1.7
8.5
6.9
Anisotropy = 21.7%
42.3
0.2
42.3
0.2
JH100
γ = 1.9
8.7
6.85
Anisotropy = 23.6%
48.7
0.5
48.7
0.5
JH154
γ = 2.2
8.5
6.9
Anisotropy = 20.4%
37.0
0.5
37.0
0.5
JH101
γ = 3.1
8.6
6.9
Anisotropy = 21.9%
42.8
0.5
42.8
0.5
JH127
γ = 5.1
8.3
7.0
Anisotropy = 17.0%
21.6
0.2
21.6
0.2
JH116
γ = 5.7
8.0
7.1
Anisotropy = 11.0%
16.2
0.3
16.2
0.3
JH138
γ = 6.2
8.3
7.0
Anisotropy = 16.6%
21.3
0.4
21.3
0.4
JH152
γ = 6.3
8.0
7.0
Anisotropy = 13.2%
16.5
0.3
16.5
0.3

Figure 24. Seismic velocity and anisotropy of experimentally deformed chlorite. Seismic velocity and anisotropy calculated from the chlorite LPO (Fig. 22) are presented in the lower hemisphere using an equal-area projection. The P-wave velocity (Vp), amplitude of the S-wave anisotropy (AVs), and the polarization of the fast S-wave (Vs1) are plotted. The polarization direction of the vertically propagating fast S-wave (Vs1) is shown as bars at the center of the stereonet. x: shear direction; z: direction normal to the shear plane; γ: shear strain of sample.

3.3. Seismic anisotropy

The seismic anisotropy of P-wave is defined as $(V_{PH}-V_{PV})/V_{PV}$, and that of S-wave is defined as $(V_{SH}-V_{SV})/V_{SV}$, where V_{PH} and V_{PV} are the velocities of horizontally and vertically propagating P-waves, and V_{SH} and V_{SV} are the velocities of horizontally and vertically polarized S-waves propagating horizontally (Mainprice, 2015). The seismic velocity and anisotropy of all samples are shown in Figure 24. Type-1 chlorite LPOs produced substantially stronger seismic anisotropy than type-2 chlorite LPOs. Sample JH156, JH100, JH154, and JH101 (type-1 chlorite LPOs) produced high values (blue area of Fig. 24) for both P-wave velocity and S-wave anisotropy subparallel to the shear plane (x-y plane) (Fig. 24). In contrast, sample JH127, JH116, JH138, and JH152 (type-2 chlorite LPOs) produced high P-wave velocity (blue area of Fig. 24) subparallel to the shear direction, and high S-wave anisotropy (blue area of Fig. 24) distributed along the x-z plane. The maximum seismic anisotropy of type-1 chlorite LPOs (sample JH156, JH100, JH154, and JH101) was very strong: 23.6% for the P-wave and 48.7% for the S-wave (Table 5 and Fig. 24). In contrast, the maximum seismic anisotropy of type-2 chlorite LPOs (sample JH127, JH116, JH138, and JH152) was less strong 17.0% for the P-wave and 21.6% for the S-wave (Table 5 and Fig. 24).

For horizontal shear (θ = 0°), the polarization direction of the fast S-wave (Vs1) was subparallel to flow direction (x-direction) for both chlorite LPO types for the vertically propagating S-wave (z-direction) (Fig. 24). We also calculated seismic anisotropy of olivine for the representative two samples. The maximum seismic anisotropy of olivine LPO was 15.7% for the P-wave and 11.2% for the S-wave (Table 6 and Fig 23b). The polarization direction of the fast S-wave in olivine from sample JH156 was subnormal to the flow direction for the vertically propagating S-wave (z-direction) (Fig. 23b). For olivine from sample JH116, the polarization direction of the fast S-wave was subparallel to the flow direction (x-direction) (Fig. 23b).

4. Discussion

4.1. The LPO development of chlorite

Deformation experiments of chlorite peridotite at low shear strain ($\gamma \leq 3.1\pm0.3$) showed type-1 LPOs of chlorite, whereas those at high shear strain ($\gamma \geq 5.1\pm1.5$) showed type-2 LPOs of chlorite (Table 5 and Fig. 22). These two types of chlorite LPOs are similar to those reported in previous studies of natural samples (Kang and Jung, 2019; Kim and Jung, 2015; Morales et al., 2013; Padrón-Navarta et al., 2015; Puelles et al., 2012; Wallis et al., 2015).

Figure 21 shows the histogram of chlorite grain thickness for two samples at low shear strain (sample JH101, $\gamma = 3.1\pm0.3$) and high shear strain (sample JH152, $\gamma = 6.3\pm1.6$), respectively. The low-shear-strain sample showed a wide range of chlorite grain sizes, whereas the high-shear-strain sample showed a narrow range

of chlorite grain sizes. The orientations of chlorite [001] axes were also measured corresponding to the grains. The low-shear-strain sample had predominantly thick chlorite grains (> 1 μm) and the [001] axes of chlorite were aligned subnormal to the shear plane (type-1 LPO) (Fig. 21). In contrast, the high-shear-strain sample had predominantly thin chlorite grains (≤ 1 μm) and the [001] axes of the small chlorite grains were aligned subnormal to the shear direction (girdle distribution) with a strong concentration near the center of the pole figure (type-2 LPO) (Fig. 21). These LPO results are similar to the pole figures of chlorite in Figure 22 (type-1 and type-2 LPOs). Crystal rotation accompanied by grain size reduction with increasing shear strain may be a possible factor in the development of different chlorite LPOs. The LPO development of small chlorite grains with large shear strain in this study is similar to that of amphibole (Kim and Jung, 2019; Zucali et al., 2015), micas (Wenk et al., 2010), wadsleyite (Tommasi et al., 2004), and calcite (Zucali and Chateigner, 2020). Kim and Jung (2019) have recently conducted deformation experiments of amphibole in simple shear under high P-T conditions (P = 0.5 GPa, T = 500–700 °C). The increased shear strain reduced the grain size of amphibole and the [100] axes of the small grains were distributed as a girdle with a strong concentration near the center of the pole figure, which is characterized as type-IV amphibole LPO (Kim and Jung, 2019).

4.2. Implications for seismic anisotropy

The maximum seismic anisotropy of the S-wave was up to 48.7% for the type-1 chlorite LPOs, and up to 21.6% for the type-2 chlorite LPOs (Table 5 and Fig. 24). Seismic anisotropy of the mixture of the olivine and chlorite LPOs (sample JH156 and JH116), and the mixture of the chlorite and serpentine LPOs (sample

JH100 for chlorite and sample VM3 of Jung (2011) for serpentine) were calculated (Table 6). The delay time of the S-wave of the mixtures were calculated using the equation of Pera et al. (2003), for the 5–30 km thick layer of chlorite peridotite (Fumagalli and Poli, 2005; Hacker et al., 2003b; Schmidt and Poli, 1998). Although the maximum seismic anisotropy of the S-wave of olivine LPOs was moderate (9.4–11.2%) (Table 6 and Fig. 23b), mixing olivine with chlorite (70:30 ratio) increased the maximum seismic anisotropy of the S-wave up to 19.3% (Table 6). The maximum seismic anisotropy of the mixture of chlorite and serpentine LPOs was 28.4–37.6% for the S-wave, which increased continuously with increasing chlorite ratio (Table 6 and Fig. 25). The delay time of the S-wave of the mixture of olivine and chlorite LPOs (70:30 ratio) was in the range of 0.2–1.2 s, and that of the mixture of chlorite and serpentine LPOs was up to 0.4–2.4 s, which increased continuously with increasing chlorite ratio (Table 6). The resulting maximum seismic anisotropy and delay time of the S-wave of the mixtures are considered to be sufficiently large to influence seismic anisotropy in subduction zones. Other clay minerals like talc (Lee et al., 2020) and phengite (Ha et al., 2018) showed a strong source of seismic anisotropy in subduction zones. Carbonate such as magnesite was found inside serpentinite and showed a strong LPO development (Menzel et al., 2022). But, there was no report on the seismic anisotropy of magnesite.

Considering deformation of chlorite in subduction zones where the slab has a dip angle, a type-1 chlorite LPO produces a trench-normal (parallel to the x-direction) Vs1 polarization direction for shallow subducting slab dip angles ($\theta = 0$ and 30°), but a trench-parallel (parallel to the y-direction) Vs1 polarization

direction for a large dip angles (θ = 45 and 60°) (Figs. 24 and 26). Previous studies of the LPO of deformed chlorite in nature showed a similar result (Kim and Jung, 2015). However, a type-2 chlorite LPO produces a trench-normal Vs1 polarization direction for any dip angle of the subducting slab (Figs. 24 and 26). The chlorite fabric transition probably occurs as subduction progresses to increasing levels of shear strain. New chlorites are produced in the mantle wedge under the fore-arc area owing to the dehydration of minerals in the subducting slab. As the new chlorites have not yet experienced a large shear strain in the subduction zone, they can retain the type-1 LPO to a considerable depth. In addition, thick chlorite peridotite at low temperatures in the upper part of the subducting slab under the fore-arc area may experience a low shear strain, producing the type-1 LPO. Therefore, the type-1 chlorite LPO may occur in fore-arc zones with low shear strain, producing trench-parallel seismic anisotropy in the slab and at the lower part of the mantle wedge. The type-2 chlorite LPO may occur in back-arc zones with high shear strain, producing the trench-normal seismic anisotropy observed in back-arc regions (Fischer et al., 1998; Huang et al., 2011a, b; Nakajima and Hasegawa, 2004; Smith et al., 2001). As suggested by previous studies, different olivine LPOs may also contribute to the large seismic anisotropy observed in fore-arc and back-arc settings (Jung and Karato, 2001b; Jung et al., 2006; Jung et al., 2020; Karato et al., 2008; Katayama and Karato, 2006; Kneller et al., 2005).

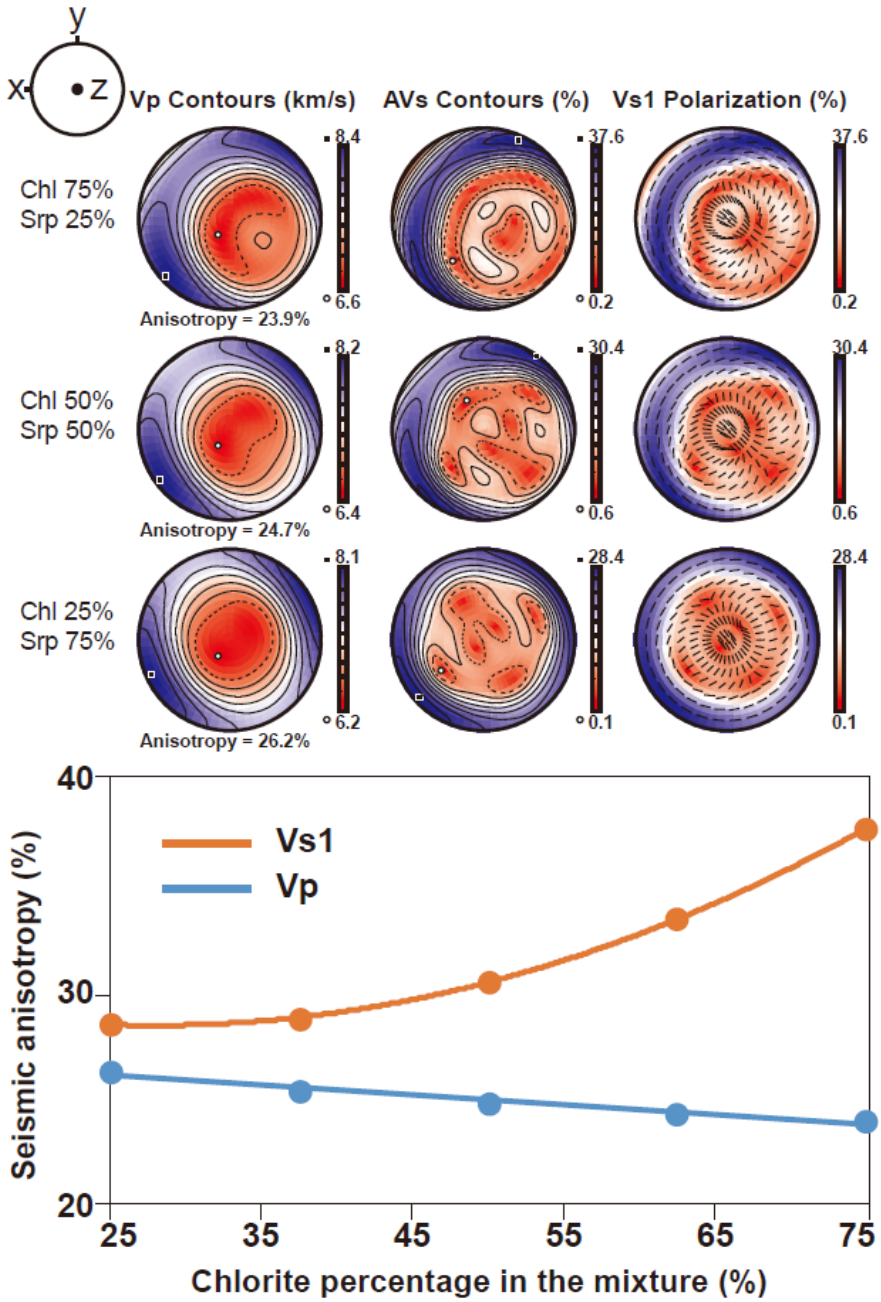

Figure 25. Change in seismic anisotropy due to the mixture of chlorite and serpentine. Seismic velocity and anisotropy were calculated using the LPO of the chlorite (sample JH100) and serpentine (sample VM3 of Jung (2011)). Pole figures are presented in the lower hemisphere using an equal-area projection. The P-wave velocity (Vp), amplitude of the S-wave anisotropy (AVs), and the polarization of the fast S-wave (Vs1) are plotted. The polarization direction of the vertically propagating fast S-wave (Vs1) is shown as bars at the center of the stereonet. x: shear direction; z: direction normal to the shear plane; Chl: chlorite; Srp: serpentine.

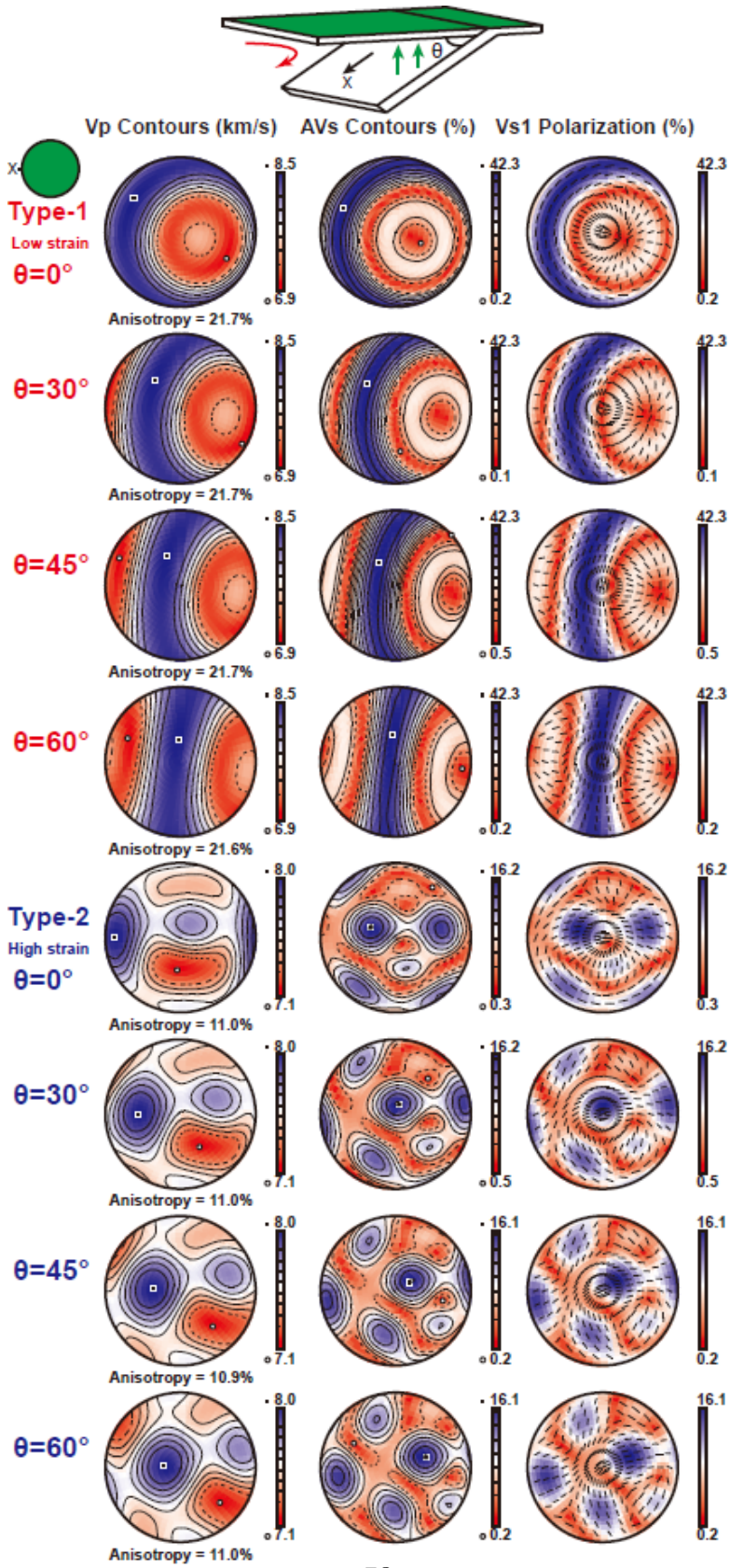
θ
X
Vp Contours (km/s)
AVs Contours (%)
Vs1 Polarization (%)
Type-1
Low strain
θ=0°
Anisotropy = 21.7%
θ=30°
Anisotropy = 21.7%
θ=45°
Anisotropy = 21.7%
θ=60°
Anisotropy = 21.6%
Type-2
High strain
θ=0°
Anisotropy = 11.0%
θ=30°
Anisotropy = 11.0%
θ=45°
Anisotropy = 10.9%
θ=60°
Anisotropy = 11.0%

Figure 26. Seismic velocity and anisotropy of experimentally deformed chlorite with a dip angle (θ). Seismic velocity and anisotropy calculated from representative chlorite LPOs (type-1 (sample JH156, γ = 1.7) and type-2 (sample JH116, γ = 5.7)) (Fig. 22) are presented in the lower hemisphere using an equal-area projection. The P-wave velocity (Vp), amplitude of the S-wave anisotropy (AVs), and the polarization of the fast S-wave (Vs1) are plotted. The polarization direction of the vertically propagating fast S-wave (Vs1) is shown as bars at the center of the stereonet. In the cartoon, the green plane represents the projection plane of pole figures, the green arrows represent the vertically propagating S-wave, and the red arrow represents the mantle flow direction. x: shear direction.

4.3. Chlorite stability in subduction zone

Chlorite is stable in the upper part of the subducting slab and chlorite peridotite in the slab can be thick (~5–30 km) depending on the slab temperature (Fumagalli and Poli, 2005; Hacker et al., 2003b; Schmidt and Poli, 1998). Chlorite can also be formed in the mantle wedge by the reaction of peridotite with fluid available from the dehydration of minerals in the subducting slab. Kim and Jung (2015) reported natural chlorite peridotites exhumed from the subduction zone, which contained up to 35% chlorite. Morales et al. (2013) reported the presence of ~22% chlorite in erupted mantle fragments, and Alt et al. (2012) also reported the presence of ~20% chlorite in chlorite harzburgite which was exhumed from the subduction zone. Lee et al. (2020) recently reported the presence of ~30% chlorite in ultrahigh-pressure tectonic mélange from central Asia. Figure 27 is the pseudosection calculated using Theriak-Domino software (de Capitani and Petrakakis, 2010), showing that chlorite peridotite in the subduction zone can contain up to 37% chlorite.

5. Conclusions

High P-T (P = 0.5–2.5 GPa, T = 540–720 °C) deformation experiments of chlorite peridotite revealed two different LPO types of chlorite, which developed depending on the magnitude of the shear strain. The type-1 chlorite LPO was characterized by the [001] axes aligned subnormal to the shear plane and developed under low shear strain ($\gamma \leq 3.1 \pm 0.3$). The type-2 chlorite LPO was characterized by a girdle distribution of the [001] axes subnormal to the shear direction and developed under high shear strain ($\gamma \geq 5.1 \pm 1.5$). Our data indicate that crystal rotation accompanied by grain size reduction with increasing shear strain possibly causes different LPOs of chlorite. When considering mixtures of chlorite with olivine or serpentine, the strong seismic anisotropy of the S-wave of chlorite LPOs (48.7% for the type-1 chlorite LPO and 21.6% for the type-2 chlorite LPO) can increase those seismic anisotropy of mixtures. We found that the type-1 chlorite LPO could produce trench-parallel seismic anisotropy in the fore-arc zones, whereas the type-2 chlorite LPO could produce trench-normal seismic anisotropy in the back-arc area of subduction zones. Our results suggest that anomalous seismic anisotropy of S-wave in subduction zones can be influenced by a strong chlorite LPO.

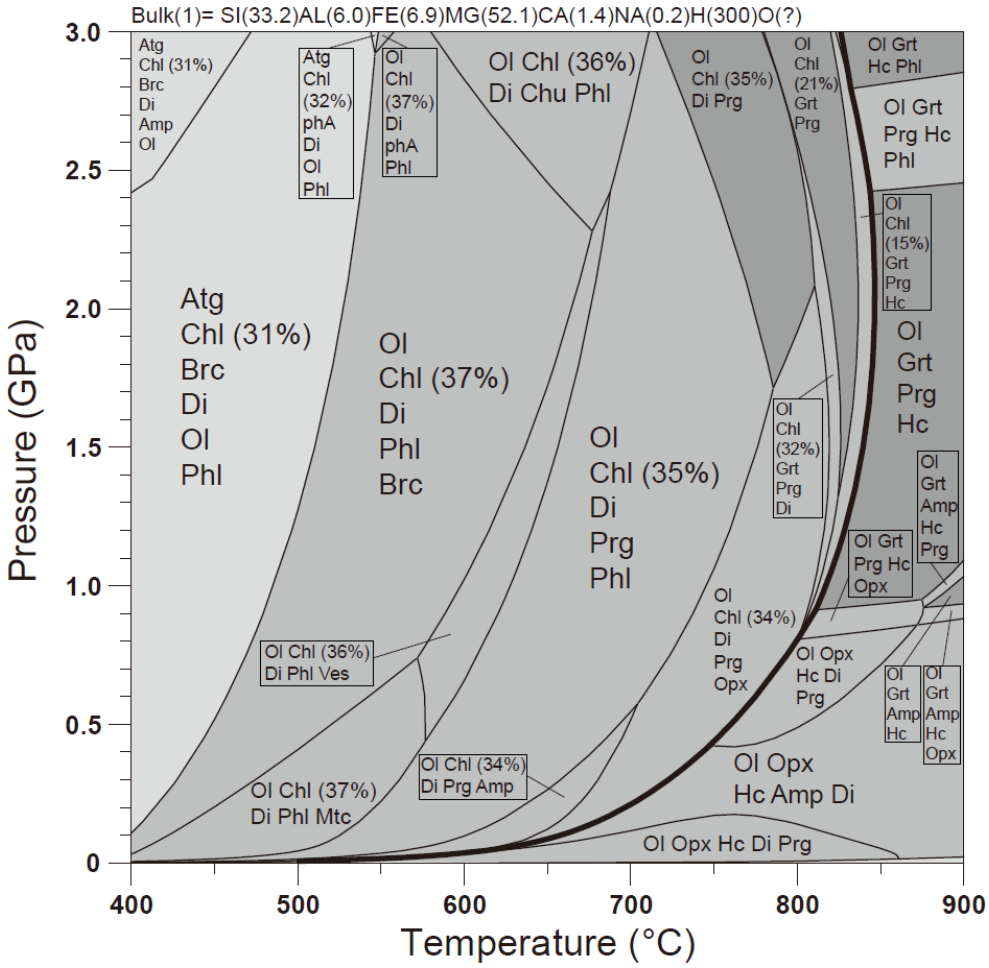

Figure 27. Chlorite stability field and volume percentage. Based on the starting material (chlorite peridotite of Kim and Jung (2015)), the stability field and volume percentage of chlorite were calculated using Theriak-Domino software (de Capitani and Petrakakis, 2010). The thick solid line represents stability field of chlorite. O(?) in bulk represents auto calculation of oxygen content in Theriak-Domino software. Chl: chlorite; Ol: olivine; Atg: antigorite; Di: diopside; Grt: garnet; Amp: amphibole; Opx: orthopyroxene; Phl: phlogopite; Prg: pargasite; Brc: brucite; Hc: hercynite; Chu: clinohumite; Mtc: monticellite; Ves: vesuvianite; phA: phase A.

CHAPTER 4: Dehydration embrittlement of chlorite and implications for intermediate-depth earthquakes

Abstract

Dehydration embrittlement has been proposed as the possible mechanism for intermediate-depth (50–300 km) earthquakes of subducting slabs. Previous experimental studies of serpentine and lawsonite showed their dehydration embrittlement which could trigger intermediate-depth earthquakes. Even though chlorite is known as hydrous and stable mineral under pressure-temperature (P-T) conditions of double seismic zone of subducting slabs, dehydration embrittlement of chlorite has not been studied yet. Deformation experiments of chlorite peridotite were conducted under the high P-T conditions (P = 0.5–2.5 GPa, T = 500–750 °C). Some high temperature conditions of experiments caused partial dehydration of chlorite. Fine-grained Ca-amphibole was found by energy dispersive spectrometer (EDS) and field emission electron probe micro analyzer (FE-EPMA) as dehydration product of chlorite. Samples with partial dehydration of chlorite showed faults under high pressure conditions ($1.5 \leq P \leq 2.5$ GPa) with dehydration product, Ca-amphibole, which distributed along fault plane. However, every sample under low pressure conditions ($0 < P < 1.5$ GPa) showed no faults. The results indicate that dehydration embrittlement of chlorite can trigger intermediate-depth earthquakes under the phase of chlorite peridotite in double seismic zone of subducting slabs.

Keywords: chlorite, earthquake, dehydration embrittlement

1. Introduction

Intermediate-depth earthquakes are defined as earthquakes of 50–300 km depth of subducting slabs (Hacker et al., 2003b; Jung et al., 2004) and have been reported in many subducting slabs (Abers et al., 2013; Kirby et al., 1996; Kita et al., 2010; Kita et al., 2006). However, brittle deformation hardly occurs in high pressure and temperature (P-T) conditions (Green and Houston, 1995; Kirby, 1995; Raleigh and Paterson, 1965). There are three main hypotheses for the mechanism of intermediate-depth earthquakes: transformational faulting, ductile shear instability, and dehydration embrittlement (Hacker et al., 2003b). Transformational faulting is a fault-making process by weaker reaction products of phase transformation (Green and Burnley, 1989; Kirby, 1987). Ductile shear instability is that a shear instability generates heat faster, melts failure planes and causes slip under relatively low shear stresses (Ogawa, 1987). Dehydration embrittlement is a change from ductile to brittle behavior by increasing fluid pressure, which comes from dehydration reactions (Raleigh and Paterson, 1965). The equation for shear failure $\sigma_s = C + \mu\sigma_n$ changes into $\sigma_s = C + \mu(\sigma_n - P_f) = C + \mu\sigma_n^*$ with dehydration reactions, where σ_s is the shear stress at failure, σ_n is the normal stress at failure, C is the constant known as cohesion, μ is the constant known as coefficient of internal friction, P_f is fluid pressure, and σ_n^* is the effective stress (Raleigh and Paterson, 1965; van der Pluijm and Marshak, 2010). Increased fluid pressure by mineral dehydrations decreases the effective stress, which weakens wet rocks to be broken under lower differential stress than dry rocks (van der Pluijm and Marshak, 2010). Thus, dehydration embrittlement was proposed as a plausible mechanism of intermediate-depth earthquakes of subducting slabs so far (Green and Houston,

1995; Hacker et al., 2003b; Hasegawa and Nakajima, 2017; Jung and Green, 2004; Jung et al., 2004; Kirby, 1995; Mishra and Zhao, 2004; Raleigh and Paterson, 1965; Wang et al., 2017), and might affect even deep-focus (> 300 km) earthquakes (Zhang et al., 2021). Experimental studies of Jung and Green (2004) and Jung et al. (2004) found out that dehydration embrittlement of serpentine could trigger intermediate-depth earthquakes. Experiments of Okazaki and Hirth (2016) found out that dehydration embrittlement of lawsonite also could be the cause of intermediate-depth earthquakes in subducting oceanic crust. Experimental study of Incel et al. (2017) suggested transition from lawsonite blueschist to lawsonite eclogite could cause brittle failure of cold subduction zones. Ferrand and Manea (2021) found dehydration-driven stress transfer in a subducted oceanic crust could be the mechanism of intermediate-depth earthquakes beneath Romania. Recently, Wang et al. (2022) found that hydrated faults in subducting slabs could trigger trench-parallel seismic anisotropy, and great earthquakes like 2011 Tohoku-oki earthquake (Mw 9.0) on intermediate-depth.

Chlorite is a hydrous mineral which has wide stability field in high P-T conditions of subduction zones (Fumagalli and Poli, 2005; Hacker et al., 2003b) (Fig. 28). Chlorite also has been reported as an important mineral for water transport to the mantle as well as for fluid transfer reactions in subduction zones (Hermann and Lakey, 2021; Peacock and Wang, 1999; Scambelluri et al., 2019; Smit and von Strandmann, 2020); arc magmatism and seismicity on the lower plane of double seismic zones could possibly be influenced by chlorite breakdown (Fumagalli and Poli, 2005; Hacker et al., 2003b). In particular, the thermal structure of subduction zones was considered to have relation with intermediate-

depth (50–300 km) intraslab seismicity, which could be interpreted by the pore-fluid pressure increasing dehydration of hydrous minerals including serpentine and chlorite (Hasegawa and Nakajima, 2017; Jung et al., 2004; Kirby et al., 1996; Mishra and Zhao, 2004; Peacock, 2001; Wang et al., 2017). Peacock and Wang (1999) compared the seismicity and thermal structures of the subduction zones of northeastern and southwestern Japan, and suggested dehydration reactions of hydrous minerals including chlorite for triggering intermediate depth earthquakes. Because there has been no evidence on the dehydration embrittlement of chlorite yet, we conducted deformation experiments of chlorite peridotite in this study for dehydration embrittlement of chlorite.

2. Methods

2.1. Starting material

The chlorite peridotite of Almklovdalen, Western Gneiss Region, southwest Norway was used as the starting material. The starting material bulk composition was olivine (60%), chlorite (31%), orthopyroxene (5%), clinopyroxene (3%), and garnet (1%). The chemical composition of chlorite was clinochlore of $(Mg_{4.6}Fe^{2+}_{0.3}Cr_{0.1})Al(Si_3Al)O_{10}(OH)_8$, analyzed by a JEOL JXA-8900R EPMA at the NCIRF at SNU (Kim and Jung, 2015).

2.2. Deformation experiment

A modified Griggs apparatus at the Tectonophysics Laboratory, SEES in SNU was used to conduct simple shear experiments. Figure 19 shows the sample assembly. Samples were prepared with starting material core-drilled with a

diameter of 3.1 mm and cut at 45°. They were placed between Al_2O_3 pistons inside a nickel capsule. Pressure mediums were CsCl and NaCl. The temperature was measured by two thermocouples (Pt-30% Rh-70% and Pt-6% Rh-94%). The confining pressure was increased in 12 h and the temperature was increased within 1 h. Samples were deformed under constant strain rates of $2.7–9.7\times10^{-6}$ s^{-1}. After each deformation experiment, the sample was quenched to room temperature by shutting off the power and decreasing the pressure in 12 h.

2.3. Stability field and modal abundance of minerals

Thermodynamic calculation was used for the stability field, modal abundance, and reaction between minerals. The calculation was based on the modal composition of starting material and the Na_2O-CaO-FeO-MgO-Al_2O_3-SiO_2-H_2O (NCFMASH) model system using Theriak-Domino software (de Capitani and Petrakakis, 2010) with the database of Holland and Powell (2011) (tc55MnNCKFMASH file). Solid solutions for the mineral phases were chlorite (Holland et al., 1998), olivine (Holland and Powell, 1998), antigorite (Holland and Powell, 1998), diopside (Holland and Powell, 1996), garnet (White et al., 2007), amphibole (Diener and Powell, 2012), orthopyroxene (Powell and Holland, 1999), phlogopite (Holland and Powell, 1998), pargasite (Holland and Powell, 1998), brucite (Holland and Powell, 1998), hercynite (Holland and Powell, 1998), clinohumite (Holland and Powell, 1998), monticellite (Holland and Powell, 1998), vesuvianite (Holland and Powell, 1998), and phase A (Holland and Powell, 1998).

2.4. Analytical methods

Samples were cut along the x-z plane (x: shear direction, z: normal to the

shear plane) after experiments. Carefully polished using Syton 0.06 μm colloidal silica, samples were observed using a JEOL JSM-7100F FE-SEM housed at the SEES in SNU. EDS mapping in a FE-SEM was used for acquiring element distributions on microstructures of samples. The accelerating voltage was 15 kV, and the working distance was 10 mm in the FE-SEM. Step size of EDS mapping was ca. 45–200 nm. AZtec software of Oxford Instruments was used for the EDS analysis. A JEOL JXA-8530F FE-EPMA at the NCIRF at SNU was used to analyze the chemical composition of the resultant minerals of samples. For the FE-EPMA setting, the acceleration voltage was 15 kV, working distance was 10 mm, current probe was 20 nA, and beam diameter was 3 μm. Peak time was 10 seconds for Na and K, and 20 seconds for other elements. Background time was 5 seconds for Na and K, and 10 seconds for other elements.

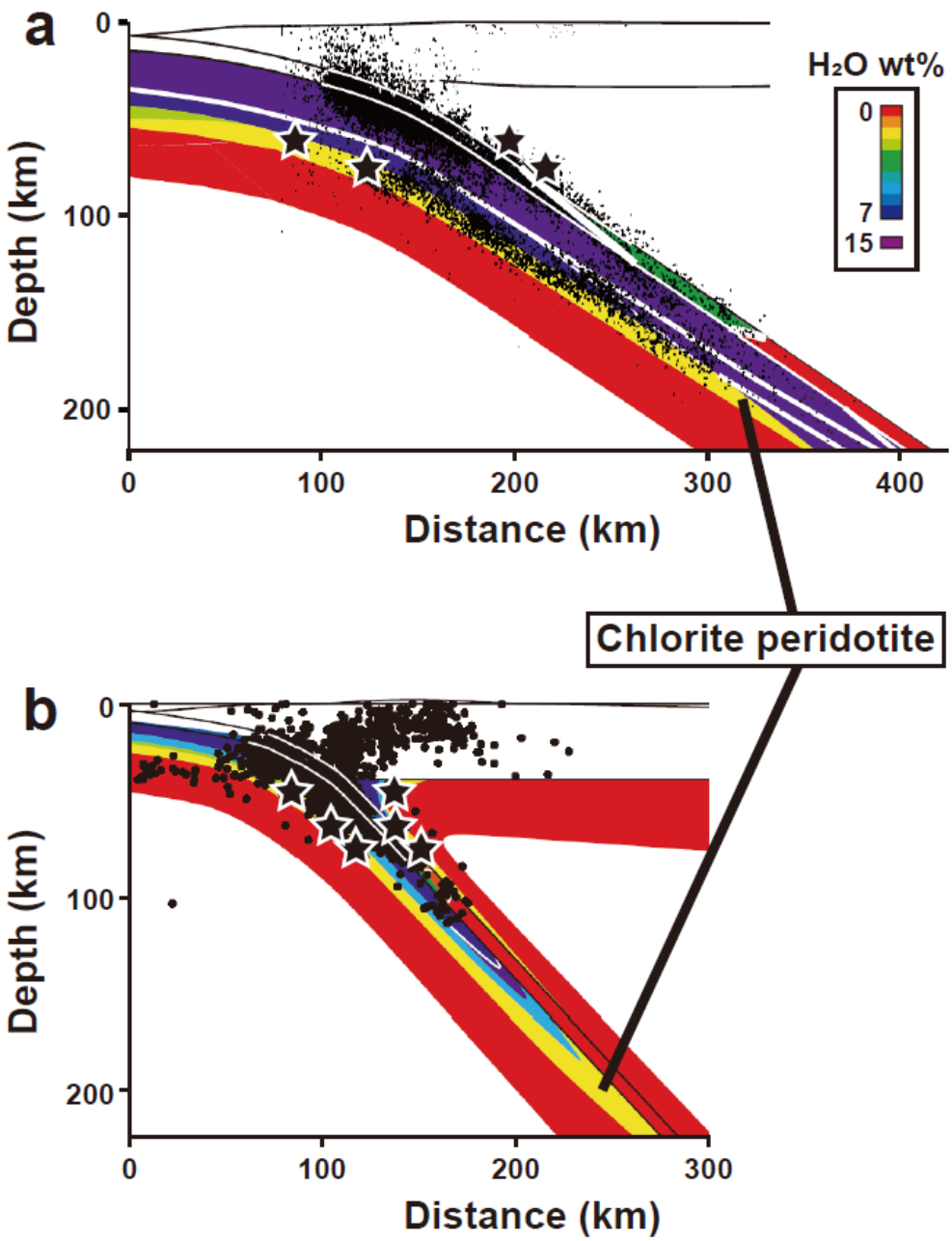

Figure 28. Stable area of chlorite peridotite phase in subduction zones of **(a)** northeastern Japan and **(b)** Costa Rica, corresponds to yellow area (modified after Hacker et al. (2003b)). Seismicity was represented as black dots. Black stars indicate experimental conditions of samples showing faults and partial dehydration of chlorite in this study.

Table 7. Experimental conditions and results of experiments.

Sample	Pressure (GPa)	Temperature (°C)	Longitudinal Strain	Strain Rate (s^{-1})	Max. Differential Stress (MPa)	Fault Development
JH101	**0.5**	**650±15**	0.09	2.65×10^{-6}	254±15	X
JH116	**0.5**	**650±15**	0.19	9.68×10^{-6}	348±15	X
JH127	**1.0**	**650±15**	0.15	6.30×10^{-6}	120±10	X
JH100	**1.0**	**720±20**	0.09	5.48×10^{-6}	131±10	X
JH138	**1.5**	**650±15**	0.14	6.26×10^{-6}	352±15	O
JH218	**1.5**	**650±15**	0.13	6.03×10^{-6}	415±20	O
JH146	**2.0**	**500±10**	0.14	6.90×10^{-6}	354±15	X
JH154	**2.0**	**570±10**	0.12	6.41×10^{-6}	259±15	X
JH139	**2.0**	**600±10**	0.16	6.19×10^{-6}	346±15	X
JH140	**2.0**	**650±15**	0.16	6.36×10^{-6}	173±10	X
JH220	**2.0**	**670±15**	0.21	6.77×10^{-6}	363±15	X
JH228	**2.0**	**730±20**	0.15	7.33×10^{-6}	489±20	O
JH156	**2.5**	**540±10**	0.07	6.53×10^{-6}	238±15	X
JH152	**2.5**	**630±10**	0.17	6.51×10^{-6}	171±10	X
JH221	**2.5**	**690±15**	0.09	6.81×10^{-6}	130±10	X
JH225	**2.5**	**750±20**	0.21	7.12×10^{-6}	169±10	O

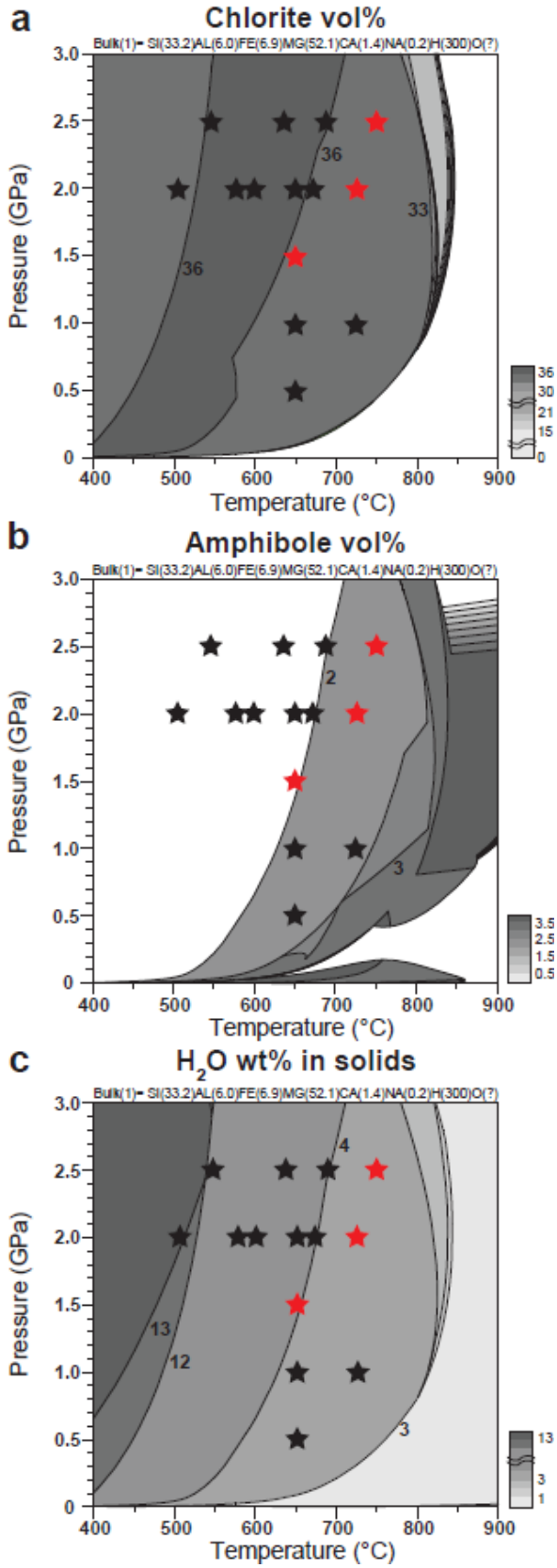
a
Chlorite vol%
Bulk(1)= SI(33.2)AL(6.0)FE(6.9)MG(52.1)CA(1.4)NA(0.2)H(300)O(?)
Pressure (GPa)
Temperature (°C)
36
33
36
36
30
21
15
0
b
Amphibole vol%
Bulk(1)= SI(33.2)AL(6.0)FE(6.9)MG(52.1)CA(1.4)NA(0.2)H(300)O(?)
Pressure (GPa)
Temperature (°C)
2
3
3.5
2.5
1.5
0.5
c
H2O wt% in solids
Bulk(1)= SI(33.2)AL(6.0)FE(6.9)MG(52.1)CA(1.4)NA(0.2)H(300)O(?)
Pressure (GPa)
Temperature (°C)
4
13
12
3
13
3
1

Figure 29. Stability fields and volume percentage of minerals, and weight percentage of H_2O in solids. Based on the starting material (chlorite peridotite of Kim and Jung (2015)), calculated using Theriak-Domino software (de Capitani and Petrakakis, 2010). O(?) in bulk represents auto calculation of oxygen content in Theriak-Domino software. Black and red stars indicate the experimental conditions in this study. Red stars are samples in which fault microstructures and Ca-amphibole observed.

3. Results

Table 7 shows results of simple shear deformation experiments. Sixteen experiments were conducted under high P-T conditions (P = 0.5–2.5 GPa, T = 500–750 °C) and constant strain rate of 2.7–9.7×10^{-6} s^{-1} (Table 7). Only four samples showed faulted microstructures developed in three different P-T conditions, 1.5 GPa and 650 °C, 2.0 GPa and 730 °C, 2.5 GPa and 750 °C (Table 7 and Fig. 29). Figure 29 shows stability field of minerals calculated based on the starting material modal composition (Kim and Jung, 2015; Kim et al., 2020). Thermodynamic calculation also expected that the amphibole could be the product of the dehydration reaction: chlorite + pyroxene + Na-phlogopite + vesuvianite = olivine + amphibole + H_2O. Every sample with fault microstructures were found on chlorite-amphibole coexistence zone of P-T condition, under pressure range of 1.5–2.5 GPa (Fig. 29).

In case of samples without faulted microstructures, strain localization made chlorite grains become thin and their sheets be aligned slightly oblique to the shear direction (Fig. 30a). However, chlorite sheets and olivine grains of three high temperature conditions were cut by fault plane under pressure 1.5–2.5 GPa (Table 7 and Figs. 30b, c). Evidence of the dehydration of chlorite is the existence of fluid

inclusions. Fluid inclusion trails were observed in samples which developed fault structures (Fig. 31). Fluid came from dehydration of chlorite left fluid inclusion trails inside olivine grains and the trails were aligned subparallel to σ_1, the maximum principal stress of deformation experiments (Figs. 19 and 31a, c). Aligned fluid inclusions were developed into Mode-I cracks which were also subparallel to σ_1 (Figs. 31b and d).

EDS mapping of samples detected fine-grained reaction products along fault microstructures. Figures 32 and 33 show EDS mapped images of the area including the fault plane. Chlorite sheets were shown as the area of Al concentrations (Fig. 32b), and the existence of the thin Ca area was found in the fault plane (Figs. 32c and 33b, d). The only mineral containing Ca in the starting material was clinopyroxene in 3% of bulk composition. However, FE-EPMA analysis revealed the resultant dehydration product containing Ca as amphibole (Table 8), which did not exist in the starting material. The chemical composition of the Ca-amphibole was close to tremolite, determined by using a Excel spreadsheet of Locock (2014).

4. Discussion and conclusions

Experiments were conducted in the expected stability field of chlorite (Table 7 and Fig. 29a). However, partial dehydration of chlorite produced amphibole (up to 2.4% of modal composition) with increasing temperature (Fig. 29b). In three different pressure conditions (1.5, 2.0, and 2.5 GPa), samples showed Ca-amphibole as partial dehydration product of chlorite with their upmost temperature conditions of deformation experiments (Figs. 29, 32, and 33). However, in lower

pressure conditions (0.5 and 1.0 GPa) samples showed no evidence of partial dehydration products of chlorite nor fault microstructures (Figs. 29 and 34). Consistent occurrence of fault microstructures and Ca-amphibole—observed on pressure range of 1.5–2.5 GPa—imply that dehydration embrittlement of chlorite may not be active under the pressure 1.5 GPa (~ca. 50 km depth).

Double seismic zone is characteristic intermediate-depth seismicity in subducting slabs observed in many subduction zones including northeastern Japan, Tonga, northern Chile, Alaska, Kamchatka, the Marianas, New Britain, Costa Rica, and the Kuriles (Brudzinski et al., 2007; Fang and van der Hilst, 2019; Florez and Prieto, 2019; Hacker et al., 2003b; Peacock, 2001; Wang et al., 2017). Type I double seismic zones are characterized as the layer separation of 20–40 km, which converges at 200 km, represented by northeastern Japan, Kamchatka, the Kuriles, the Marianas, Tonga, and so on; type II double seismic zones are characterized as the layer separation less than 15 km, which converges at 150 km, represented by northern Chile, Alaska, New Britain, Costa Rica, and so on (Florez and Prieto, 2019; Han et al., 2016). The upper layer seismicity of double seismic zone was thought to be attributed to dehydration embrittlement of hydrous minerals like serpentine and lawsonite, but the seismicity resources of the lower layer of double seismic zone was relatively ambiguous (Florez and Prieto, 2019; Hacker et al., 2003b; Han et al., 2016; Hasegawa and Nakajima, 2017; Kirby, 1995; Okazaki and Hirth, 2016; Peacock, 2001; Wang et al., 2017). Most of warm subduction zones, which corresponds to type II double seismic zone, were known as their characteristics to produce and deliver fluids to much deeper depth than other subduction zones could (Han et al., 2016; Peacock and Wang, 1999; Smit and von

Strandmann, 2020). Therefore, type II double subduction zones could be considered to have more plausible dehydration embrittlement. However, even cold subduction zones, which corresponds to type I double seismic zone, were considered to be able to deliver fluids to the deep mantle in chlorite-rich rock composition (Hermann and Lakey, 2021). Accordingly, dehydration embrittlement could be considered as possible origin of seismicity for cold subduction zones either (Hasegawa and Nakajima, 2017; Mishra and Zhao, 2004; Peacock, 2001; Wang et al., 2017).

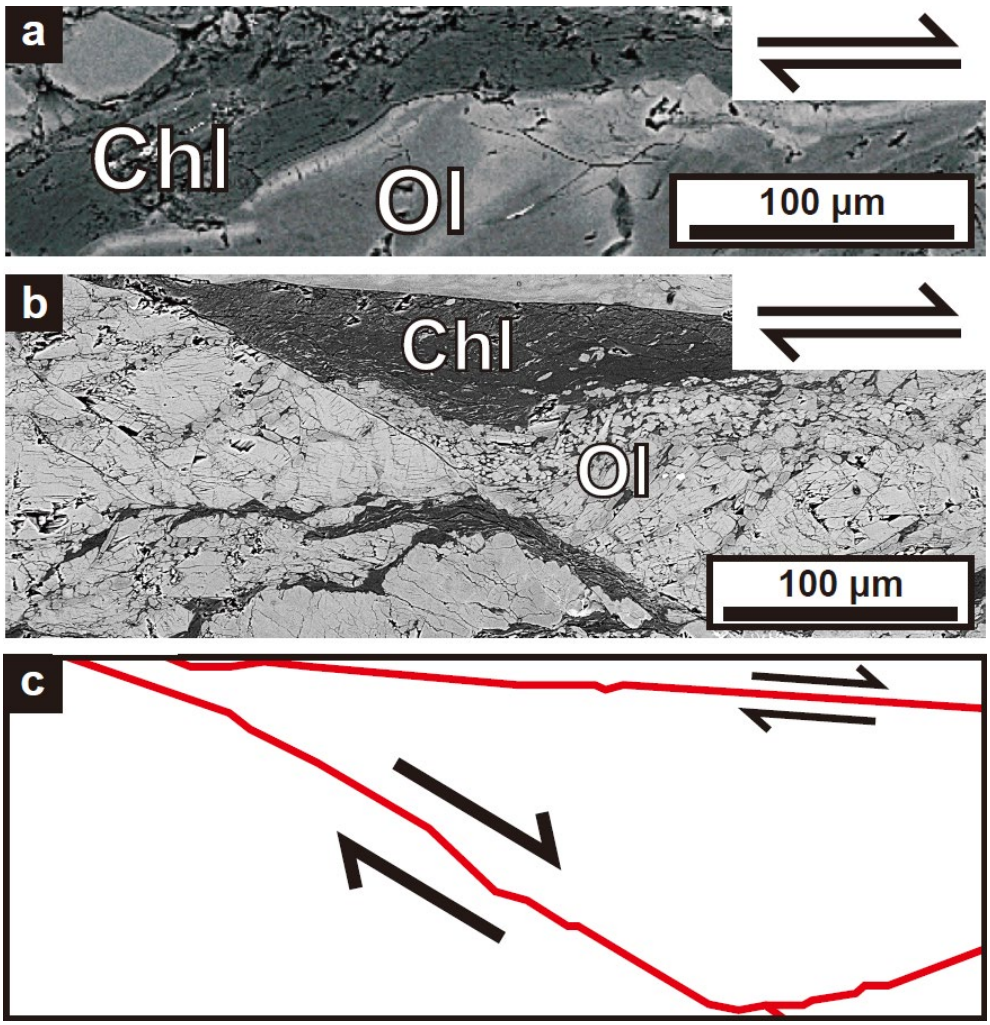

Figure 30. BEIs of deformed samples taken with an acceleration voltage of 15 kV and a working distance of 10 mm using the JEOL JSM-7100F FE-SEM. **(a)** BEI of sample JH146 (P = 2.0 GPa, T = 500 °C), showing ductile chlorite sheets. **(b)** BEI of sample JH228(P = 2.0 GPa, T = 730 °C), showing faulted chlorite sheets. **(c)** Faults illustration of **(b)**. Chl: chlorite; Ol: olivine.

Table 8. Chemical composition of minerals after deformation experiment.

wt% Oxides	JH220			JH138			JH228			JH225		
	Ol	Chl	Py	Amp 1	Amp 2	Amp 3	Amp 1	Amp 2	Amp 3	Amp 1	Amp 2	Amp 3
SiO_2	40.68	37.65	57.23	58.27	57.32	58.22	57.54	55.52	54.47	54.53	54.36	54.82
TiO_2	-	0.18	0.08	0.03	0.03	-	0.07	0.06	0.12	0.05	0.01	0.02
Al_2O_3	0.06	8.82	3.03	1.05	1.01	1.01	1.67	2.57	2.57	1.75	1.45	1.70
Cr_2O_3	-	0.85	0.53	0.15	0.17	0.15	0.20	0.59	0.65	0.31	0.23	0.37
FeO	8.12	5.95	1.90	1.85	1.86	1.74	1.85	2.07	2.26	1.79	1.93	1.98
MnO	0.11	0.02	0.05	0.03	0.08	0.10	0.08	0.04	0.09	0.15	0.11	0.07
MgO	50.49	31.94	24.11	24.31	23.68	24.24	22.88	22.90	23.19	19.93	21.97	22.26
CaO	0.04	0.03	11.83	11.60	11.45	11.86	12.33	12.10	11.81	18.25	14.89	15.70
Na_2O	0.14	0.33	1.11	0.59	0.61	0.62	0.63	0.95	0.88	0.75	0.58	0.79
K_2O	-	0.08	0.11	0.01	0.03	0.03	0.04	0.08	0.08	-	0.01	0.01
NiO	0.45	-	-	-	-	-	-	-	-	-	-	-
Sum[1]	100.09	85.85	99.97	97.89	96.24	97.98	97.29	96.87	96.13	97.51	95.55	97.73
O=24												
Si	5.948	6.223	7.983	8.254	8.263	8.247	8.223	8.017	7.945	7.970	8.025	7.944
Ti	-	0.023	0.009	0.004	0.003	-	0.007	0.006	0.013	0.005	0.002	0.003
Al	0.010	1.719	0.505	0.175	0.172	0.169	0.282	0.438	0.442	0.301	0.253	0.290
Cr	-	0.111	0.060	0.016	0.019	0.017	0.023	0.068	0.075	0.036	0.027	0.043
Fe^{2+}	0.993	0.823	0.224	0.219	0.225	0.207	0.222	0.250	0.276	0.219	0.239	0.240
Mn	0.014	0.003	0.006	0.004	0.010	0.012	0.010	0.004	0.011	0.019	0.014	0.009
Mg	11.003	7.871	5.008	5.134	5.089	5.119	4.874	4.930	5.043	4.341	4.835	4.808
Ca	0.007	0.004	1.772	1.761	1.769	1.800	1.887	1.872	1.845	2.858	2.356	2.439
Na	0.041	0.107	0.303	0.161	0.170	0.170	0.174	0.265	0.250	0.213	0.165	0.223
K	-	0.016	0.020	0.002	0.005	0.006	0.008	0.015	0.016	-	0.002	0.001
Ni	0.053	-	-	-	-	-	-	-	-	-	-	-
Cations	18.068	16.901	15.888	15.730	15.725	15.747	15.709	15.866	15.916	15.962	15.918	15.999

[1]Includes uncertainty of ±1.0%.

Ol: olivine; Chl: chlorite; Py: pyroxene; Amp: amphibole.

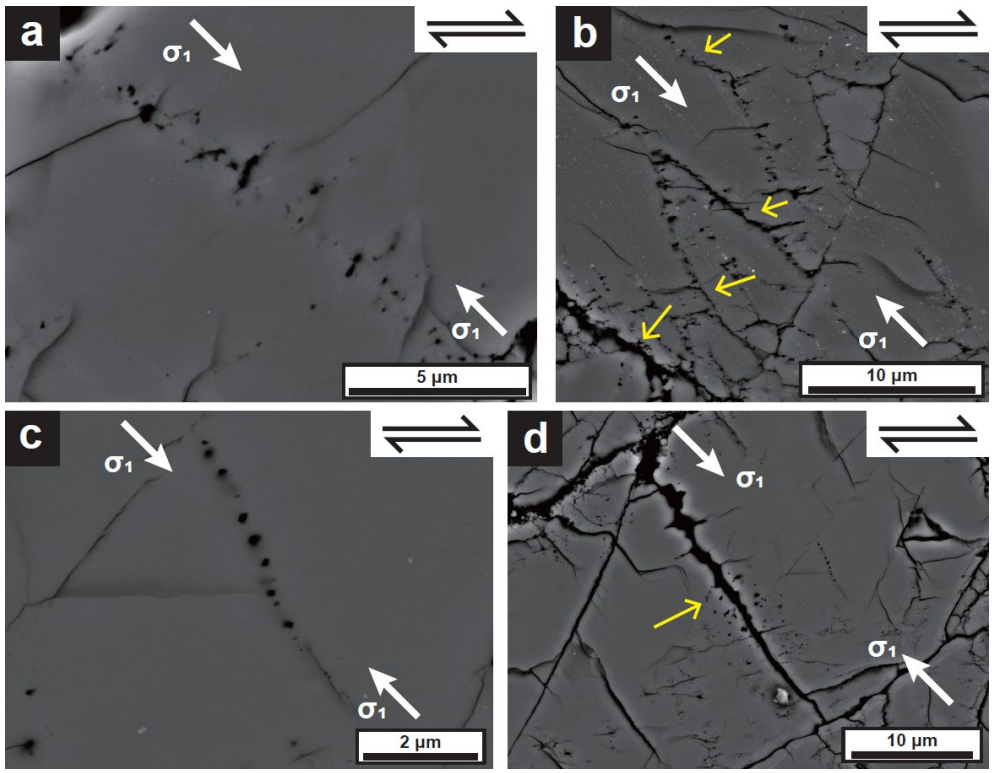

Figure 31. BEIs showing fluid inclusion trails **(a and c)** and Mode-I cracks **(b and d)** in olivine of samples which showed fault microstructures. BEIs were taken with an acceleration voltage of 15 kV and a working distance of 10 mm using the JEOL JSM-7100F FE-SEM. Representative BEIs of **(a)** JH218 (P = 1.5 GPa, T = 650 °C), **(b)** JH138(P = 1.5 GPa, T = 650 °C), and **(c and d)** JH228(P = 2.0 GPa, T = 730 °C) were selected. White arrows indicate σ_1, the maximum principal stress, and yellow arrows indicate Mode-I cracks generated along the fluid inclusion trails.

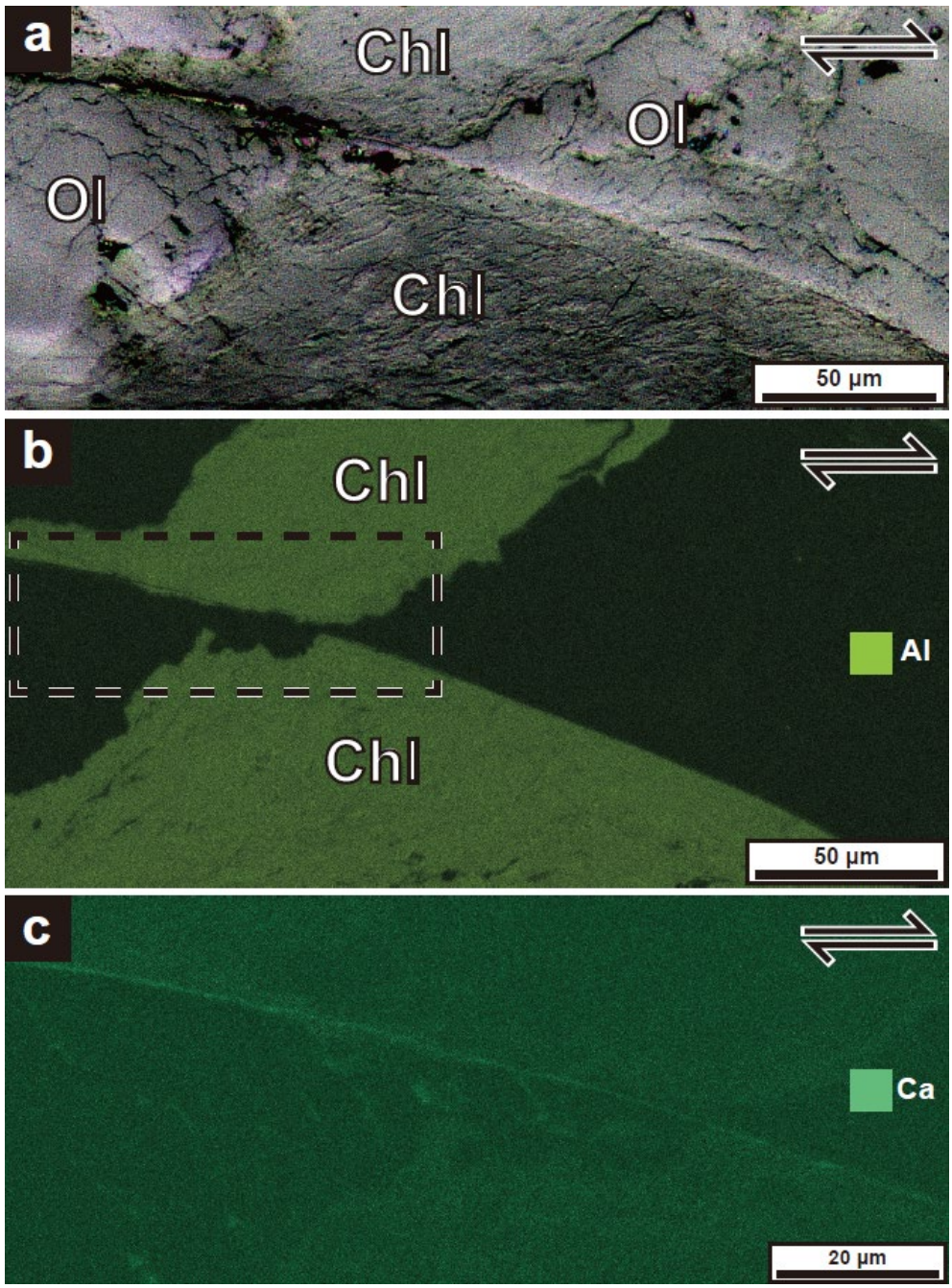

Figure 32. The fault plane of sample JH138 (P = 1.5 GPa, T = 650 °C) shown by **(a)** optical photomicrograph with reflected light and **(b)** EDS mapping image using the JEOL JSM-7100F FE-SEM. Chlorite sheets were represented by Al concentration of EDS mapping image. **(c)** Magnified view of the dashed box in **(b)** showed thin and clear Ca distribution on the fault plane. Chl: chlorite; Ol: olivine.

Previous studies about dehydration embrittlement of double seismic zones mostly focused on serpentine, but serpentine dehydration was hard to explain the lower layer seismicity of double seismic zone (Hasegawa and Nakajima, 2017; Mishra and Zhao, 2004; Peacock, 2001). The chlorite peridotite phase is stable on almost consistent area with the lower layer of double seismic zone (Hacker et al., 2003b), even more for type II—relatively warmer and younger—double seismic zone (Brudzinski et al., 2007; Hasegawa and Nakajima, 2017). Furthermore, dehydration embrittlement of chlorite found in this study was by partial dehydration of chlorite, preserving chlorite sheets in the samples after developing fault microstructures (Figs. 30, 32, and 33). The correlation between phase stability of chlorite peridotite and double seismic zone can be understood as chlorite-preserving faulted chlorite peridotites in this study. Peacock (2001) found the lower layer earthquakes of double seismic zone at 3.0 GPa and 550–800 °C; this was close to the experimental conditions of this study which showed fault microstructures and partial dehydration of chlorite (P = 1.5–2.5 GPa, T = 650–750 °C). The P-T conditions of faulted chlorite peridotite samples in this study (P = 1.5–2.5 GPa, T = 650–750 °C) could be compared to observed double seismic zone of subducting slabs. Both upper and lower layer of double seismic zone correspond to faulted chlorite peridotites in this study under intermediate-depth (Fig. 28). Especially for type II double seismic zone, seismicity of the mantle wedge also could match P-T conditions of faulted chlorite peridotite (Fig. 28b). Therefore, intermediate-depth earthquakes of double seismic zone could be attributed to dehydration embrittlement of chlorite peridotite. The starting material contained ~30% of chlorite in volume percentage. Faulted samples after deformation experiments showed > 15% of chlorite volume percentage. Hacker et al. (2003a)

calculated 10–35% chlorite volume percentage in the peridotites of subducting slab conditions. Therefore, it is considered that chlorite volume percentage of ~15–30% in the peridotites in subducting slabs may be sufficient for dehydration embrittlement. Figure 28 showed the representative examples of double seismic zone for dehydration embrittlement of chlorite peridotite: northeastern Japan for type I double seismic zone, and Costa Rica for type II double seismic zone. The different depth limit of two types of double seismic zone was attributed to subducting angles, oceanic plate age, slab temperature, plate thickness, convergence velocity, back-arc deformation patterns, and so on (Florez and Prieto, 2019; Han et al., 2016). The correlation between dehydration embrittlement of chlorite and slab seismicity also could explain the different depth limit of two types of double seismic zone. The temperature difference of slabs could affect the depth of full dehydration of chlorite, which was possibly responsible for the lower layer of double seismic zone. Warm slabs might have the full dehydration depth of chlorite shallower than cold slabs, and that depth difference could affect the depth limit of double seismic zone.

This study conducted deformation experiments of chlorite peridotite to find out dehydration embrittlement of chlorite under high P-T conditions of subduction zone (P = 0.5–2.5 GPa, T = 500–750 °C). Under the pressure $1.5 \leq P \leq 2.5$ GPa, partial dehydration of chlorite produced Ca-amphibole and developed a fault. The P-T conditions of experiments, which showed partial dehydration of chlorite and fault microstructures (P = 1.5–2.5 GPa, T = 650–750 °C) had a good match with both seismicity of upper and lower layer of double seismic zone (Fumagalli and Poli, 2005; Hacker et al., 2003b; Peacock, 2001). The type II double seismic

zones—that of warmer and younger slabs—was more plausible for dehydration embrittlement of chlorite. The result in this study suggests dehydration embrittlement of chlorite peridotite the possible intermediate-depth earthquake triggering mechanism for double seismic zone, especially for the lower layer, whose seismicity resources were relatively ambiguous.

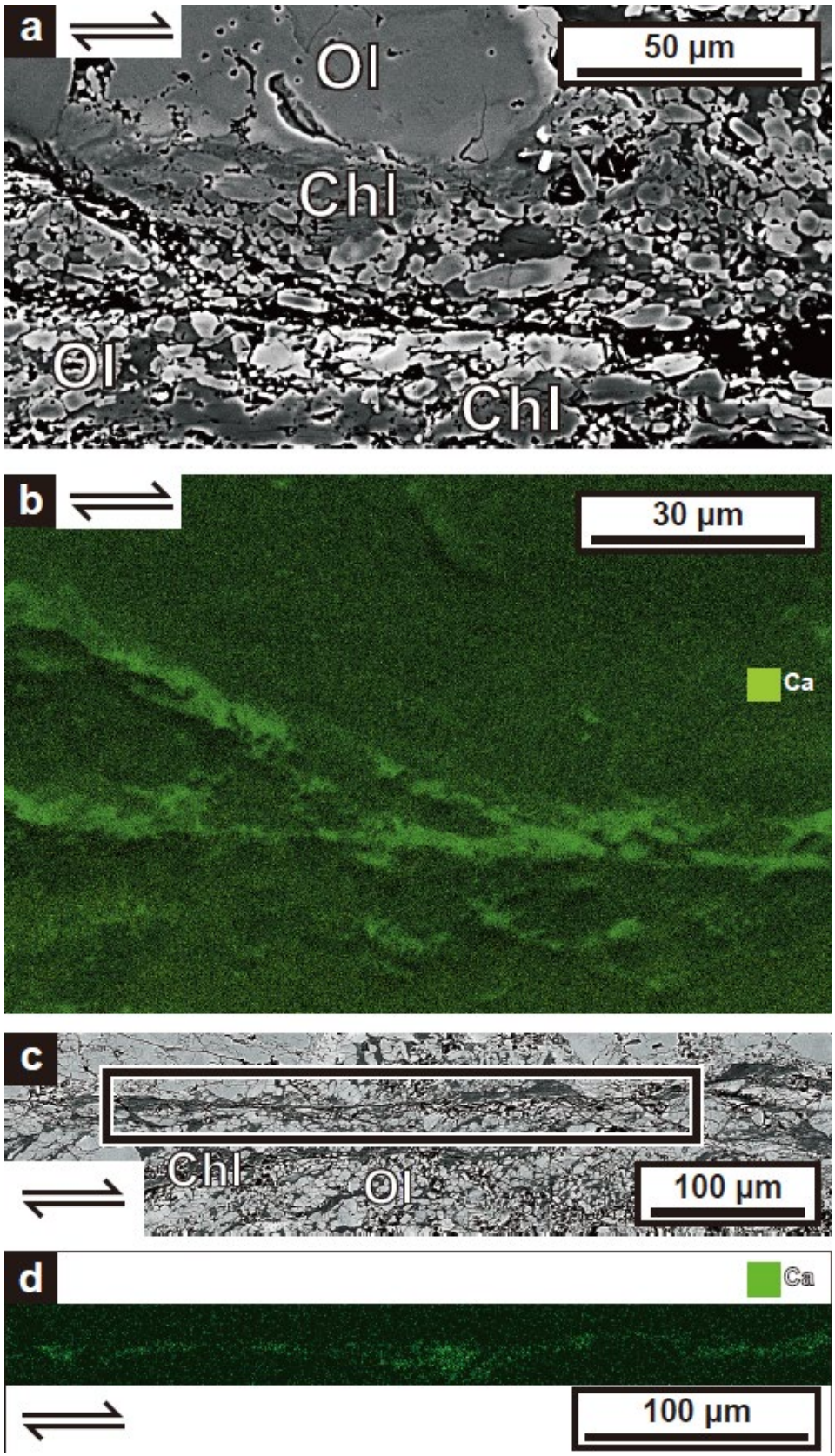
a
Ol
50 µm
Chl
Ol
Chl
b
30 µm
Ca
c
Chl
Ol
100 µm
d
Ca
100 µm

Figure 33. BEIs and EDS mapping images using the JEOL JSM-7100F FE-SEM. **(a)** BEI of sample JH225 (P = 2.5 GPa, T = 750 °C) shear zone. **(b)** Ca distribution shown by EDS mapping of **(a)**. **(c)** BEI of sample JH228 (P = 2.0 GPa, T = 730 °C) shear zone. **(d)** Ca distribution shown by EDS mapping of a solid box in **(c)**. Chl: chlorite; Ol: olivine.

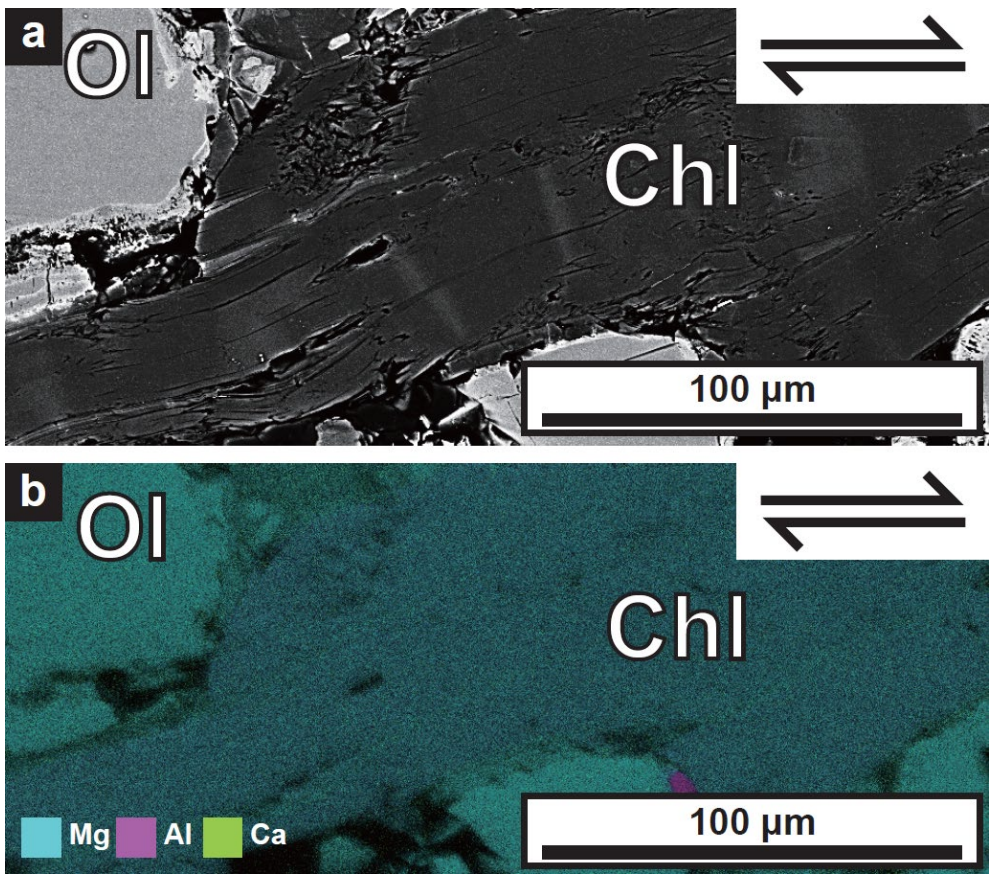

Figure 34. BEI and EDS mapping images using the JEOL JSM-7100F FE-SEM. **(a)** BEI of sample JH156 (P = 2.5 GPa, T = 540 °C), showing no fault microstructures developed. **(b)** Mg, Al, and Ca distribution shown by EDS mapping of **(a)**. Ca distribution was not detected unlike Mg and Al. Chl: chlorite; Ol: olivine.

CHAPTER 5: Conclusion

The thesis presented detailed analysis of chlorite microstructures under high pressure and high temperature conditions, to understand seismic anisotropy and mechanism of intermediate-depth observed in subduction zones. Chlorite is elastically anisotropic and hydrous mineral which is stable over subducting slab and mantle wedge. It is found two distinct LPO types of chlorite from naturally and experimentally deformed chlorite peridotites. Presented are the studies of deformed natural chlorite peridotites exhumed from high P-T condition (Chapter 2), experimentally deformed chlorite microstructures under high P-T conditions (Chapter 3), and dehydration embrittlement of chlorite to understand intermediate-depth earthquakes in subduction zones (Chapter 4).

In chapter 2, chlorite peridotites from Almklovdalen, southwest Norway were studied. The deformed samples were exhumed from peak P-T conditions about 2.2 GPa and 690–770 °C. Olivine showed previously known LPO types (Jung, 2017; Jung and Karato, 2001b; Jung et al., 2006; Katayama et al., 2004). Chlorite showed two different types of LPOs, producing strong seismic anisotropy in subduction zones. Furthermore, the polarization direction of the fast S-wave rotated 90° depending on the dip angle (θ) in subducting slab. Low angle ($\theta \leq 45°$) subducting slab with chlorite can contribute to trench-normal seismic anisotropy, and high angle ($\theta > 50°$) subducting slab can contribute to trench-parallel seismic anisotropy.

In chapter 3, chlorite peridotite was experimentally deformed under high P-T

conditions (P = 0.5–2.5 GPa, T = 540–720 °C) in simple shear, using modified Griggs apparatus to find out distinct deformation conditions for two different LPO types of chlorite. The type-1 chlorite LPO is characterized by the [001] axes aligned subnormal to the shear plane, and the type-2 chlorite LPO is characterized by a girdle distribution of the [001] axes subnormal to the shear direction (Jung, 2017; Kim and Jung, 2015). The type-1 chlorite LPO developed under low shear strain ($\gamma \leq 3.1 \pm 0.3$), producing trench-parallel seismic anisotropy. The type-2 chlorite LPO developed under high shear strain ($\gamma \geq 5.1 \pm 1.5$), producing trench-normal seismic anisotropy.

In chapter 4, dehydration embrittlement of chlorite was studied to understand mechanism of intermediate-depth (50–300 km) earthquakes. The chlorite peridotite is expected to be stable over double seismic zone of subducting slabs (Hacker et al., 2003b). Thermodynamic calculation and models of the starting material predicted a partial dehydration of chlorite to produce Ca-amphibole at high temperature. Deformation experiments using modified Griggs apparatus under high P-T conditions (P = 0.5–2.5 GPa, T = 500–750 °C) showed some samples with fault microstructures. Only with fine-grained Ca-amphibole observed, faults were developed under high pressure conditions ($1.5 \leq P \leq 2.5$ GPa). This result suggests that chlorite dehydration embrittlement can contribute to cause intermediate-depth earthquakes in double seismic zone of subducting slabs in subduction zones.

REFERENCES

Abers, G. A., Nakajima, J., van Keken, P. E., Kita, S., and Hacker, B. R., 2013, Thermal–petrological controls on the location of earthquakes within subducting plates: Earth and Planetary Science Letters, v. 369, p. 178-187.

Abramson, E. H., Brown, J. M., Slutsky, L. J., and Zaug, J., 1997, The elastic constants of San Carlos olivine to 17 GPa: Journal of Geophysical Research: Solid Earth, v. 102, no. B6, p. 12253-12263.

Abt, D. L., Fischer, K. M., Abers, G. A., Strauch, W., Protti, J. M., and González, V., 2009, Shear wave anisotropy beneath Nicaragua and Costa Rica: Implications for flow in the mantle wedge: Geochemistry, Geophysics, Geosystems, v. 10, no. 5, p. Q05S15.

Aleksandrov, K. S., and Ryzhova, T. V., 1961, The elastic properties of rock forming minerals, pyroxenes and amphiboles: Bulletin of Academy of Sciences USSR, Geophysical Series, v. 9, p. 871-875.

Alt, J. C., Garrido, C. J., Shanks, W. C., Turchyn, A., Padrón-Navarta, J. A., López Sánchez-Vizcaíno, V., Gómez-Pugnaire, M. T., and Marchesi, C., 2012, Recycling of water, carbon, and sulfur during subduction of serpentinites: A stable isotope study of Cerro del Almirez, Spain: Earth and Planetary Science Letters, v. 327, p. 50-60.

Behr, W. M., and Smith, D., 2016, Deformation in the mantle wedge associated with Laramide flat-slab subduction: Geochemistry, Geophysics, Geosystems, v. 17, no. 7, p. 2643-2660.

Bell, D. R., Rossman, G. R., Maldener, J., Endisch, D., and Rauch, F., 2003, Hydroxide in olivine: A quantitative determination of the absolute amount and calibration of the IR spectrum: Journal of Geophysical Research: Solid Earth (1978–2012), v. 108, no. B2, p. 2105.

ben Ismaïl, W., and Mainprice, D., 1998, An olivine fabric database: An overview of upper mantle fabrics and seismic anisotropy: Tectonophysics, v. 296, p. 145-157.

Berman, R. G., Aranovich, L. Y., and Pattison, D. R. M., 1995, Reassessment of the garnet-clinopyroxene Fe-Mg exchange thermometer: II. Thermodynamic

analysis: Contributions to Mineralogy and Petrology, v. 119, p. 30-42.

Bezacier, L., Reynard, B., Bass, J. D., Sanchez-Valle, C., and van de Moortèle, B., 2010, Elasticity of antigorite, seismic detection of serpentinites, and anisotropy in subduction zones: Earth and Planetary Science Letters, v. 289, no. 1-2, p. 198-208.

Boudier, F., Baronnet, A., and Mainprice, D., 2010, Serpentine mineral replacements of natural olivine and their seismic implications: Oceanic lizardite versus subduction-related antigorite: Journal of Petrology, v. 51, no. 1-2, p. 495-512.

Brownlee, S. J., Hacker, B. R., Harlow, G. E., and Seward, G., 2013, Seismic signatures of a hydrated mantle wedge from antigorite crystal-preferred orientation (CPO): Earth and Planetary Science Letters, v. 375, p. 395-407.

Brudzinski, M. R., Thurber, C. H., Hacker, B. R., and Engdahl, E. R., 2007, Global prevalence of double Benioff zones: Science, v. 316, no. 5830, p. 1472-1474.

Bystricky, M., Kunze, K., Burlini, L., and Burg, J.-P., 2000, High shear strain of olivine aggregates: Rheological and seismic consequences: Science, v. 290, p. 1564-1567.

Cao, Y., Du, J., Park, M., Jung, S., Park, Y., Kim, D., Choi, S., Jung, H., and Austrheim, H., 2020, Metastability and nondislocation-based deformation mechanisms of the Flem eclogite in the Western Gneiss Region, Norway: Journal of Geophysical Research: Solid Earth, v. 125, no. 5, p. e2020JB019375.

Cao, Y., Jung, H., and Song, S., 2017, Olivine fabrics and tectonic evolution of fore-arc mantles: A natural perspective from the Songshugou dunite and harzburgite in the Qinling orogenic belt, central China: Geochemistry, Geophysics, Geosystems, v. 18, no. 3, p. 907-934.

Cardenes, V., Lopez-Sanchez, M. A., Barou, F., Olona, J., and Llana-Fúnez, S., 2021, Crystallographic preferred orientation, seismic velocity and anisotropy in roofing slates: Tectonophysics, v. 808, p. 228815.

Couvy, H., Frost, D. J., Heidelbach, F., Nyilas, K., Ungar, T., Mackwell, S., and Cordier, P., 2004, Shear deformation experiments of forsterite at 11 GPa-1400 °C in the multianvil apparatus: European Journal of Mineralogy, v. 16,

no. 6, p. 877-889.

Currie, C. A., Cassidy, J. F., Hyndman, R. D., and Bostock, M. G., 2004, Shear wave anisotropy beneath the Cascadia subduction zone and western North American craton: Geophysical Journal International, v. 157, p. 341-353.

de Capitani, C., and Petrakakis, K., 2010, The computation of equilibrium assemblage diagrams with Theriak/Domino software: American Mineralogist, v. 95, no. 7, p. 1006-1016.

Deer, W. A., Howie, R. A., and Zussman, J., 2013, Chlorite group, An introduction to the rock-forming minerals, Mineralogical Society of Great Britain and Ireland, p. 208-215.

Diener, J. F. A., and Powell, R., 2012, Revised activity–composition models for clinopyroxene and amphibole: Journal of Metamorphic Geology, v. 30, no. 2, p. 131-142.

Faccenda, M., Burlini, L., Gerya, T. V., and Mainprice, D., 2008, Fault-induced seismic anisotropy by hydration in subducting oceanic plates: Nature, v. 455, p. 1097-1100.

Fang, H., and van der Hilst, R. D., 2019, Earthquake depth phase extraction with P wave autocorrelation provides insight into mechanisms of intermediate-depth earthquakes: Geophysical Research Letters, v. 46, no. 24, p. 14440-14449.

Ferrand, T. P., and Manea, E. F., 2021, Dehydration-induced earthquakes identified in a subducted oceanic slab beneath Vrancea, Romania: Scientific Reports, v. 11, p. 10315.

Fischer, K. M., Fouch, M. J., Wiens, D. A., and Boettcher, M. S., 1998, Anisotropy and flow in Pacific subduction zone back-arcs, Geodynamics of lithosphere & Earth's mantle, Springer, p. 463-475.

Florez, M. A., and Prieto, G. A., 2019, Controlling factors of seismicity and geometry in double seismic zones: Geophysical Research Letters, v. 46, no. 8, p. 4174-4181.

Fumagalli, P., and Poli, S., 2005, Experimentally determined phase relations in hydrous peridotites to 6·5 GPa and their consequences on the dynamics of subduction zones: Journal of Petrology, v. 46, no. 3, p. 555-578.

Gifkins, R. C., 1970, Optical microscopy of metals, New York, American Elsevier.

Green, H. W., and Burnley, P. C., 1989, A new self-organizing mechanism for deep-focus earthquakes: Nature, v. 341, p. 733-737.

Green, H. W., and Houston, H., 1995, The mechanics of deep earthquakes: Annual Review of Earth and Planetary Sciences, v. 23, p. 169-213.

Ha, Y., Jung, H., and Raymond, L. A., 2018, Deformation fabrics of glaucophane schists and implications for seismic anisotropy: The importance of lattice preferred orientation of phengite: International Geology Review, v. 61, no. 6, p. 720-737.

Hacker, B. R., Abers, G. A., and Peacock, S. M., 2003a, Subduction factory 1. Theoretical mineralogy, densities, seismic wave speeds, and H2O contents: Journal of Geophysical Research: Solid Earth, v. 108, no. B1, p. 2029.

Hacker, B. R., Andersen, T. B., Johnston, S., Kylander-Clark, A. R. C., Peterman, E. M., Walsh, E. O., and Young, D., 2010, High-temperature deformation during continental-margin subduction & exhumation: The ultrahigh-pressure Western Gneiss Region of Norway: Tectonophysics, v. 480, no. 1-4, p. 149-171.

Hacker, B. R., Peacock, S. M., Abers, G. A., and Holloway, S. D., 2003b, Subduction factory 2. Are intermediate-depth earthquakes in subducting slabs linked to metamorphic dehydration reactions?: Journal of Geophysical Research: Solid Earth, v. 108, no. B1, p. 2030.

Han, P., Wei, D., Zhang, K., Sun, Z., and Zhou, X., 2016, Lattice-Preferred orientations of olivine in subducting oceanic lithosphere derived from the observed seismic anisotropies in double seismic zones: Earthquake Science, v. 29, no. 4, p. 243-258.

Han, S., and Jung, H., 2021, Deformation microstructures of phyllite in Gunsan, Korea, and implications for seismic anisotropy in continental crust: Minerals, v. 11, no. 3, p. 294.

Hasegawa, A., and Nakajima, J., 2017, Seismic imaging of slab metamorphism and genesis of intermediate-depth intraslab earthquakes: Progress in Earth and Planetary Science, v. 4, p. 1-31.

Hermann, J., and Lakey, S., 2021, Water transfer to the deep mantle through hydrous, Al-rich silicates in subduction zones: Geology, v. 49, no. 8, p. 911-915.

Hirauchi, K.-i., Michibayashi, K., Ueda, H., and Katayama, I., 2010, Spatial variations in antigorite fabric across a serpentinite subduction channel: Insights from the Ohmachi Seamount, Izu-Bonin frontal arc: Earth and Planetary Science Letters, v. 299, no. 1-2, p. 196-206.

Holland, T. J. B., Baker, J., and Powell, R., 1998, Mixing properties and activity-composition relationships of chlorites in the system MgO-FeO-Al2O3-SiO2-H2O: European Journal of Mineralogy, v. 10, no. 3, p. 395-406.

Holland, T. J. B., and Powell, R., 1996, Thermodynamics of order-disorder in minerals: II. symmetric formalism applied to solid solutions: American Mineralogist, v. 81, no. 11-12, p. 1425-1437.

-, 1998, An internally consistent thermodynamic data set for phases of petrological interest: Journal of Metamorphic Geology, v. 16, no. 3, p. 309-343.

-, 2011, An improved and extended internally consistent thermodynamic dataset for phases of petrological interest, involving a new equation of state for solids: Journal of Metamorphic Geology, v. 29, no. 3, p. 333-383.

Holtzman, B. K., Kohlstedt, D. L., Zimmerman, M. E., Heidelbach, F., Hiraga, T., and Hustoft, J., 2003, Melt segregation and strain partitioning: Implications for seismic anisotropy and mantle flow: Science, v. 301, p. 1227-1230.

Huang, Z., Zhao, D., and Wang, L., 2011a, Frequency-dependent shear-wave splitting and multilayer anisotropy in northeast Japan: Geophysical Research Letters, v. 38, p. L08302.

-, 2011b, Shear wave anisotropy in the crust, mantle wedge, and subducting Pacific slab under northeast Japan: Geochemistry, Geophysics, Geosystems, v. 12, no. 1, p. Q01002.

Incel, S., Hilairet, N., Labrousse, L., John, T., Deldicque, D., Ferrand, T., Wang, Y., Renner, J., Morales, L., and Schubnel, A., 2017, Laboratory earthquakes triggered during eclogitization of lawsonite-bearing blueschist: Earth and Planetary Science Letters, v. 459, p. 320-331.

Ji, S., Li, A., Wang, Q., Long, C., Wang, H., Marcotte, D., and Salisbury, M., 2013, Seismic velocities, anisotropy, and shear-wave splitting of antigorite serpentinites and tectonic implications for subduction zones: Journal of Geophysical Research: Solid Earth, v. 118, no. 3, p. 1015-1037.

Jung, H., 2009, Deformation fabrics of olivine in Val Malenco peridotite found in

Italy and implications for the seismic anisotropy in the upper mantle: Lithos, v. 109, no. 3-4, p. 341-349.

-, 2011, Seismic anisotropy produced by serpentine in mantle wedge: Earth and Planetary Science Letters, v. 307, no. 3-4, p. 535-543.

-, 2017, Crystal preferred orientations of olivine, orthopyroxene, serpentine, chlorite, and amphibole, and implications for seismic anisotropy in subduction zones: A review: Geosciences Journal, v. 21, no. 6, p. 985-1011.

Jung, H., and Green, H. W., 2004, Experimental faulting of serpentinite during dehydration: Implications for earthquakes, seismic low-velocity zones, and anomalous hypocenter distributions in subduction zones: International Geology Review, v. 46, no. 12, p. 1089-1102.

Jung, H., Green, H. W., and Dobrzhinetskaya, L. F., 2004, Intermediate-depth earthquake faulting by dehydration embrittlement with negative volume change: Nature, v. 428, p. 545-549.

Jung, H., and Karato, S.-i., 2001a, Effects of water on dynamically recrystallized grain-size of olivine: Journal of Structural Geology, v. 23, no. 9, p. 1337-1344.

-, 2001b, Water-induced fabric transitions in olivine: Science, v. 293, p. 1460-1463.

Jung, H., Katayama, I., Jiang, Z., Hiraga, T., and Karato, S.-i., 2006, Effect of water and stress on the lattice-preferred orientation of olivine: Tectonophysics, v. 421, no. 1-2, p. 1-22.

Jung, H., Lee, J., Ko, B., Jung, S., Park, M., Cao, Y., and Song, S., 2013, Natural type-C olivine fabrics in garnet peridotites in North Qaidam UHP collision belt, NW China: Tectonophysics, v. 594, p. 91-102.

Jung, H., Mo, W., and Choi, S. H., 2009a, Deformation microstructures of olivine in peridotite from Spitsbergen, Svalbard and implications for seismic anisotropy: Journal of Metamorphic Geology, v. 27, no. 9, p. 707-720.

Jung, H., Mo, W., and Green, H. W., 2009b, Upper mantle seismic anisotropy resulting from pressure-induced slip transition in olivine: Nature Geoscience, v. 2, p. 73-77.

Jung, S., Jung, H., and Austrheim, H., 2014, Characterization of olivine fabrics and mylonite in the presence of fluid and implications for seismic anisotropy and shear localization: Earth, Planets and Space, v. 66, p. 46.

-, 2020, Microstructural evolution of amphibole peridotites in Åheim, Norway, and the implications for seismic anisotropy in the mantle wedge: Minerals, v. 10, no. 4, p. 345.

Kang, H., and Jung, H., 2019, Lattice-preferred orientation of amphibole, chlorite, and olivine found in hydrated mantle peridotites from Bjørkedalen, southwestern Norway, and implications for seismic anisotropy: Tectonophysics, v. 750, p. 137-152.

Karato, S.-i., 1987, Scanning electron microscope observation of dislocations in olivine: Physics and Chemistry of Minerals, v. 14, no. 3, p. 245-248.

Karato, S.-i., Jung, H., Katayama, I., and Skemer, P., 2008, Geodynamic significance of seismic anisotropy of the upper mantle: New insights from laboratory studies: Annual Review of Earth and Planetary Sciences, v. 36, p. 59-95.

Karato, S.-i., Toriumi, M., and Fujii, T., 1980, Dynamic recrystallization of olivine single crystals during high-temperature creep: Geophysical Research Letters, v. 7, no. 9, p. 649-652.

Katayama, I., Hirauchi, K.-i., Michibayashi, K., and Ando, J.-i., 2009, Trench-parallel anisotropy produced by serpentine deformation in the hydrated mantle wedge: Nature, v. 461, p. 1114-1117.

Katayama, I., Jung, H., and Karato, S.-i., 2004, New type of olivine fabric from deformation experiments at modest water content and low stress: Geology, v. 32, no. 12, p. 1045-1048.

Katayama, I., and Karato, S.-i., 2006, Effect of temperature on the B-to C-type olivine fabric transition and implication for flow pattern in subduction zones: Physics of the Earth and Planetary Interiors, v. 157, no. 1-2, p. 33-45.

Katayama, I., Karato, S.-i., and Brandon, M., 2005, Evidence of high water content in the deep upper mantle inferred from deformation microstructures: Geology, v. 33, no. 7, p. 613-616.

Kim, D., and Jung, H., 2015, Deformation microstructures of olivine and chlorite in chlorite peridotites from Almklovdalen in the Western Gneiss Region, southwest Norway, and implications for seismic anisotropy: International Geology Review, v. 57, no. 5-8, p. 650-668.

Kim, D., Jung, H., and Lee, J., 2020, Strain-induced fabric transition of chlorite and implications for seismic anisotropy in subduction zones: Minerals, v. 10, no. 6, p. 503.

Kim, J., and Jung, H., 2019, New crystal preferred orientation (CPO) of amphibole experimentally found in simple shear: Geophysical Research Letters, v. 46, no. 22, p. 12996-13005.

Kirby, S., 1987, Localized polymorphic phase transformations in high-pressure faults and applications to the physical mechanism of deep earthquakes: Journal of Geophysical Research: Solid Earth, v. 92, no. B13, p. 13789-13800.

-, 1995, Interslab earthquakes and phase changes in subducting lithosphere: Reviews of Geophysics, v. 33, no. S1, p. 287-297.

Kirby, S., Engdahl, R. E., and Denlinger, R., 1996, Intermediate-depth intraslab earthquakes and arc volcanism as physical expressions of crustal and uppermost mantle metamorphism in subducting slabs: Subduction Top to Bottom, p. 195-214.

Kita, S., Okada, T., Hasegawa, A., Nakajima, J., and Matsuzawa, T., 2010, Existence of interplane earthquakes and neutral stress boundary between the upper and lower planes of the double seismic zone beneath Tohoku and Hokkaido, northeastern Japan: Tectonophysics, v. 496, p. 68-82.

Kita, S., Okada, T., Nakajima, J., Matsuzawa, T., and Hasegawa, A., 2006, Existence of a seismic belt in the upper plane of the double seismic zone extending in the along-arc direction at depths of 70–100 km beneath NE Japan: Geophysical Research Letters, v. 33, p. L24310.

Kneller, E. A., van Keken, P. E., Karato, S.-i., and Park, J., 2005, B-type olivine fabric in the mantle wedge: Insights from high-resolution non-Newtonian subduction zone models: Earth and Planetary Science Letters, v. 237, no. 3-4, p. 781-797.

Kneller, E. A., van Keken, P. E., Katayama, I., and Karato, S.-i., 2007, Stress, strain, and B-type olivine fabric in the fore-arc mantle: Sensitivity tests using high-resolution steady-state subduction zone models: Journal of Geophysical Research: Solid Earth, v. 112, p. B04406.

Köhler, T. P., and Brey, G. P., 1990, Calcium exchange between olivine and

clinopyroxene calibrated as a geothermobarometer for natural peridotites from 2 to 60 kb with applications: Geochimica et Cosmochimica Acta, v. 54, no. 9, p. 2375-2388.

Kohlstedt, D. L., Goetze, C., Durham, W. B., and vander Sande, J., 1976, New technique for decorating dislocations in olivine: Science, v. 191, p. 1045-1046.

Kohlstedt, D. L., Keppler, H., and Rubie, D. C., 1996, Solubility of water in the α, β and γ phases of (Mg,Fe)2SiO4: Contributions to Mineralogy and Petrology, v. 123, no. 4, p. 345-357.

Lapen, T. J., Medaris, L. G., Beard, B. L., and Johnson, C. M., 2009, The Sandvik peridotite, Gurskøy, Norway: Three billion years of mantle evolution in the Baltica lithosphere: Lithos, v. 109, no. 3-4, p. 145-154.

Lee, J., and Jung, H., 2015, Lattice-preferred orientation of olivine found in diamond-bearing garnet peridotites in Finsch, South Africa and implications for seismic anisotropy: Journal of Structural Geology, v. 70, p. 12-22.

Lee, J., Jung, H., Klemd, R., Tarling, M. S., and Konopelko, D., 2020, Lattice preferred orientation of talc and implications for seismic anisotropy in subduction zones: Earth and Planetary Science Letters, v. 537, p. 116178.

Locock, A. J., 2014, An Excel spreadsheet to classify chemical analyses of amphiboles following the IMA 2012 recommendations: Computers & Geosciences, v. 62, p. 1-11.

Long, M. D., 2013, Constraints on subduction geodynamics from seismic anisotropy: Reviews of Geophysics, v. 51, p. 76-112.

Long, M. D., and Silver, P. G., 2008, The subduction zone flow field from seismic anisotropy: A global view: Science, v. 319, p. 315-318.

-, 2009, Shear wave splitting and mantle anisotropy: Measurements, interpretations, and new directions: Surveys in Geophysics, v. 30, no. 4-5, p. 407-461.

Long, M. D., and van der Hilst, R. D., 2006, Shear wave splitting from local events beneath the Ryukyu arc: Trench-parallel anisotropy in the mantle wedge: Physics of the Earth and Planetary Interiors, v. 155, no. 3, p. 300-312.

Mackwell, S. J., and Kohlstedt, D. L., 1990, Diffusion of hydrogen in olivine: Implications for water in the mantle: Journal of Geophysical Research:

Solid Earth (1978–2012), v. 95, no. B4, p. 5079-5088.

Mainprice, D., 1990, A FORTRAN program to calculate seismic anisotropy from the lattice preferred orientation of minerals: Computers & Geosciences, v. 16, no. 3, p. 385-393.

-, 2015, Seismic anisotropy of the deep Earth from a mineral and rock physics perspective, Treatise on geophysics, Elsevier, p. 487-538.

Mainprice, D., and Ildefonse, B., 2009, Seismic anisotropy of subduction zone minerals–contribution of hydrous phases, Subduction zone geodynamics: Berlin, Springer, p. 63-84.

McCormack, K., Wirth, E. A., and Long, M. D., 2013, B-type olivine fabric and mantle wedge serpentinization beneath the Ryukyu arc: Geophysical Research Letters, v. 40, no. 9, p. 1697-1702.

Mei, S., and Kohlstedt, D. L., 2000, Influence of water on plastic deformation of olivine aggregates: 1. Diffusion creep regime: Journal of Geophysical Research: Solid Earth, v. 105, no. B9, p. 21457-21469.

Menzel, M. D., Urai, J. L., Ukar, E., Hirth, G., Schwedt, A., Kovács, A., Kibkalo, L., and Kelemen, P. B., 2022, Ductile deformation during carbonation of serpentinized peridotite: Nature Communications, v. 13, p. 3478.

Michibayashi, K., and Oohara, T., 2013, Olivine fabric evolution in a hydrated ductile shear zone at the Moho Transition Zone, Oman ophiolite: Earth and Planetary Science Letters, v. 377, p. 299-310.

Michibayashi, K., Tasaka, M., Ohara, Y., Ishii, T., Okamoto, A., and Fryer, P., 2007, Variable microstructure of peridotite samples from the southern Mariana Trench: Evidence of a complex tectonic evolution: Tectonophysics, v. 444, p. 111-118.

Mishra, O. P., and Zhao, D., 2004, Seismic evidence for dehydration embrittlement of the subducting Pacific slab: Geophysical Research Letters, v. 31, p. L09610.

Mizukami, T., Wallis, S. R., and Yamamoto, J., 2004, Natural examples of olivine lattice preferred orientation patterns with a flow-normal a-axis maximum: Nature, v. 427, p. 432-436.

Mookherjee, M., and Mainprice, D., 2014, Unusually large shear wave anisotropy for chlorite in subduction zone settings: Geophysical Research Letters, v.

41, no. 5, p. 1506-1513.

Morales, L. F. G., Mainprice, D., and Boudier, F., 2013, The influence of hydrous phases on the microstructure and seismic properties of a hydrated mantle rock: Tectonophysics, v. 594, p. 103-117.

Mosenfelder, J. L., Deligne, N. I., Asimow, P. D., and Rossman, G. R., 2006, Hydrogen incorporation in olivine from 2–12 GPa: American Mineralogist, v. 91, no. 2-3, p. 285-294.

Nakajima, J., and Hasegawa, A., 2004, Shear-wave polarization anisotropy and subduction-induced flow in the mantle wedge of northeastern Japan: Earth and Planetary Science Letters, v. 225, no. 3-4, p. 365-377.

Nakamura, D., and Hirajima, T., 2005, Experimental evaluation of garnet–clinopyroxene geothermometry as applied to eclogites: Contributions to Mineralogy and Petrology, v. 150, no. 6, p. 581-588.

Nicolas, A., and Christensen, N. I., 1987, Formation of anisotropy in upper mantle peridotites: A review: Geodynamics Series, v. 16, p. 111-123.

Nimis, P., and Taylor, W. R., 2000, Single clinopyroxene thermobarometry for garnet peridotites. Part I. Calibration and testing of a Cr-in-Cpx barometer and an enstatite-in-Cpx thermometer: Contributions to Mineralogy and Petrology, v. 139, no. 5, p. 541-554.

Nishii, A., Wallis, S. R., Mizukami, T., and Michibayashi, K., 2011, Subduction related antigorite CPO patterns from forearc mantle in the Sanbagawa belt, southwest Japan: Journal of Structural Geology, v. 33, no. 10, p. 1436-1445.

Ogawa, M., 1987, Shear instability in a viscoelastic material as the cause of deep focus earthquakes: Journal of Geophysical Research: Solid Earth, v. 92, no. B13, p. 13801-13810.

Ohuchi, T., Kawazoe, T., Nishihara, Y., and Irifune, T., 2012, Change of olivine a-axis alignment induced by water: Origin of seismic anisotropy in subduction zones: Earth and Planetary Science Letters, v. 317, p. 111-119.

Ohuchi, T., Kawazoe, T., Nishihara, Y., Nishiyama, N., and Irifune, T., 2011, High pressure and temperature fabric transitions in olivine and variations in upper mantle seismic anisotropy: Earth and Planetary Science Letters, v. 304, no. 1-2, p. 55-63.

Okazaki, K., and Hirth, G., 2016, Dehydration of lawsonite could directly trigger

earthquakes in subducting oceanic crust: Nature, v. 530, p. 81-84.

Padrón-Navarta, J. A., Tommasi, A., Garrido, C. J., López Sánchez-Vizcaíno, V., Gómez-Pugnaire, M. T., Jabaloy, A., and Vauchez, A., 2010, Fluid transfer into the wedge controlled by high-pressure hydrofracturing in the cold top-slab mantle: Earth and Planetary Science Letters, v. 297, no. 1-2, p. 271-286.

Padrón-Navarta, J. A., Tommasi, A., Garrido, C. J., and Mainprice, D., 2015, On topotaxy and compaction during antigorite and chlorite dehydration: An experimental and natural study: Contributions to Mineralogy and Petrology, v. 169, p. 35.

Panozzo, R., 1984, Two-dimensional strain from the orientation of lines in a plane: Journal of Structural Geology, v. 6, no. 1-2, p. 215-221.

Park, J., and Levin, V., 2002, Seismic anisotropy: Tracing plate dynamics in the mantle: Science, v. 296, p. 485-489.

Park, J., Yuan, H., and Levin, V., 2004, Subduction zone anisotropy beneath Corvallis, Oregon: A serpentinite skid mark of trench-parallel terrane migration?: Journal of Geophysical Research: Solid Earth, v. 109, p. B10306.

Park, M., and Jung, H., 2020, Analysis of electron backscattered diffraction (EBSD) mapping of geological materials: Precautions for reliably collecting and interpreting data on petro-fabric and seismic anisotropy: Geosciences Journal, v. 24, no. 6, p. 679-687.

Park, M., Jung, H., and Kil, Y., 2014, Petrofabrics of olivine in a rift axis and rift shoulder and their implications for seismic anisotropy beneath the Rio Grande Rift: Island Arc, v. 23, no. 4, p. 299-311.

Park, Y., and Jung, H., 2015, Deformation microstructures of olivine and pyroxene in mantle xenoliths in Shanwang, eastern China, near the convergent plate margin, and implications for seismic anisotropy: International Geology Review, v. 57, no. 5-8, p. 629-649.

Paterson, M. S., 1982, The determination of hydroxyl by infrared absorption in quartz, silicate glasses and similar materials: Bulletin de Minéralogie, v. 105, p. 20-29.

Peacock, S. M., 2001, Are the lower planes of double seismic zones caused by

serpentine dehydration in subducting oceanic mantle?: Geology, v. 29, no. 4, p. 299-302.

Peacock, S. M., and Wang, K., 1999, Seismic consequences of warm versus cool subduction metamorphism: Examples from southwest and northeast Japan: Science, v. 286, p. 937-939.

Pera, E., Mainprice, D., and Burlini, L., 2003, Anisotropic seismic properties of the upper mantle beneath the Torre Alfina area (Northern Apennines, Central Italy): Tectonophysics, v. 370, no. 1-4, p. 11-30.

Peyton, V., Levin, V., Park, J., Brandon, M., Lees, J., Gordeev, E., and Ozerov, A., 2001, Mantle flow at a slab edge: Seismic anisotropy in the Kamchatka region: Geophysical Research Letters, v. 28, no. 2, p. 379-382.

Powell, R., and Holland, T. J. B., 1999, Relating formulations of the thermodynamics of mineral solid solutions: Activity modeling of pyroxenes, amphiboles, and micas: American Mineralogist, v. 84, no. 1-2, p. 1-14.

Pozgay, S. H., Wiens, D. A., Conder, J. A., Shiobara, H., and Sugioka, H., 2007, Complex mantle flow in the Mariana subduction system: Evidence from shear wave splitting: Geophysical Journal International, v. 170, p. 371-386.

Puelles, P., Gil Ibarguchi, J. I., Beranoaguirre, A., and Ábalos, B., 2012, Mantle wedge deformation recorded by high-temperature peridotite fabric superposition and hydrous retrogression (Limo massif, Cabo Ortegal, NW Spain): International Journal of Earth Sciences, v. 101, no. 7, p. 1835-1853.

Raleigh, C. B., and Paterson, M. S., 1965, Experimental deformation of serpentinite and its tectonic implications: Journal of Geophysical Research, v. 70, no. 16, p. 3965-3985.

Russ, J. C., and Dehoff, R. T., 2012, Practical stereology, Springer Science & Business Media.

Russo, R. M., and Silver, P. G., 1994, Trench-parallel flow beneath the Nazca plate from seismic anisotropy: Science, v. 263, p. 1105-1111.

Savage, M. K., 1999, Seismic anisotropy and mantle deformation: What have we learned from shear wave splitting?: Reviews of Geophysics, v. 37, no. 1, p. 65-106.

Scambelluri, M., Cannaò, E., and Gilio, M., 2019, The water and fluid-mobile

element cycles during serpentinite subduction. A review: European Journal of Mineralogy, v. 31, no. 3, p. 405-428.

Schmidt, M. W., and Poli, S., 1998, Experimentally based water budgets for dehydrating slabs and consequences for arc magma generation: Earth and Planetary Science Letters, v. 163, no. 1-4, p. 361-379.

Schmidtke, M. J., Keppler, R., Kossak-Glowczewski, J., Froitzheim, N., and Stipp, M., 2021, Elastic anisotropies of rocks in a subduction and exhumation setting: Solid Earth, v. 12, no. 8, p. 1801-1828.

Schulte-Pelkum, V., Monsalve, G., Sheehan, A., Pandey, M. R., Sapkota, S., Bilham, R., and Wu, F., 2005, Imaging the Indian subcontinent beneath the Himalaya: Nature, v. 435, p. 1222-1225.

Skemer, P., Katayama, I., Jiang, Z., and Karato, S.-i., 2005, The misorientation index: Development of a new method for calculating the strength of lattice-preferred orientation: Tectonophysics, v. 411, p. 157-167.

Skemer, P., Katayama, I., and Karato, S.-i., 2006, Deformation fabrics of the Cima di Gagnone peridotite massif, Central Alps, Switzerland: Evidence of deformation at low temperatures in the presence of water: Contributions to Mineralogy and Petrology, v. 152, p. 43-51.

Smit, M. A., and von Strandmann, P. A. E. P., 2020, Deep fluid release in warm subduction zones from a breached slab seal: Earth and Planetary Science Letters, v. 534, p. 116046.

Smith, G. P., Wiens, D. A., Fischer, K. M., Dorman, L. M., Webb, S. C., and Hildebrand, J. A., 2001, A complex pattern of mantle flow in the Lau backarc: Science, v. 292, p. 713-716.

Tasaka, M., Michibayashi, K., and Mainprice, D., 2008, B-type olivine fabrics developed in the fore-arc side of the mantle wedge along a subducting slab: Earth and Planetary Science Letters, v. 272, no. 3-4, p. 747-757.

Till, C. B., Grove, T. L., and Withers, A. C., 2012, The beginnings of hydrous mantle wedge melting: Contributions to Mineralogy and Petrology, v. 163, no. 4, p. 669-688.

Tommasi, A., Mainprice, D., Cordier, P., Thoraval, C., and Couvy, H., 2004, Strain-induced seismic anisotropy of wadsleyite polycrystals and flow patterns in the mantle transition zone: Journal of Geophysical Research:

Solid Earth, v. 109, p. B12405.

Ulmer, P., and Trommsdorff, V., 1995, Serpentine stability to mantle depths and subduction-related magmatism: Science, v. 268, p. 858-861.

van der Pluijm, B. A., and Marshak, S., 2010, Earth structure, New York, W. W. Norton & Company.

van der Wal, D., Chopra, P., Drury, M., and Gerald, J. F., 1993, Relationships between dynamically recrystallized grain size and deformation conditions in experimentally deformed olivine rocks: Geophysical Research Letters, v. 20, no. 14, p. 1479-1482.

van Keken, P. E., Hacker, B. R., Syracuse, E. M., and Abers, G. A., 2011, Subduction factory: 4. Depth-dependent flux of H2O from subducting slabs worldwide: Journal of Geophysical Research: Solid Earth (1978–2012), v. 116, p. B01401.

Wada, I., Behn, M. D., and Shaw, A. M., 2012, Effects of heterogeneous hydration in the incoming plate, slab rehydration, and mantle wedge hydration on slab-derived H2O flux in subduction zones: Earth and Planetary Science Letters, v. 353, p. 60-71.

Wagner, L. S., Fouch, M. J., James, D. E., and Long, M. D., 2013, The role of hydrous phases in the formation of trench parallel anisotropy: Evidence from Rayleigh waves in Cascadia: Geophysical Research Letters, v. 40, no. 11, p. 2642-2646.

Wallis, D., Lloyd, G. E., Phillips, R. J., Parsons, A. J., and Walshaw, R. D., 2015, Low effective fault strength due to frictional-viscous flow in phyllonites, Karakoram Fault Zone, NW India: Journal of Structural Geology, v. 77, p. 45-61.

Wang, J., and Zhao, D., 2013, P-wave tomography for 3-D radial and azimuthal anisotropy of Tohoku and Kyushu subduction zones: Geophysical Journal International, v. 193, no. 3, p. 1166-1181.

Wang, J., Zhao, D., and Yao, Z., 2017, Seismic anisotropy evidence for dehydration embrittlement triggering intermediate-depth earthquakes: Scientific Reports, v. 7, p. 1-9.

Wang, Q., Xia, Q. K., O'Reilly, S. Y., Griffin, W. L., Beyer, E. E., and Brueckner, H. K., 2013, Pressure- and stress-induced fabric transition in olivine from

peridotites in the Western Gneiss Region (Norway): Implications for mantle seismic anisotropy: Journal of Metamorphic Geology, v. 31, p. 93-111.

Wang, Z., Zhao, D., and Chen, X., 2022, Seismic anisotropy and intraslab hydrated faults beneath the NE Japan forearc: Geophysical Research Letters, v. 49, no. 2, p. e2021GL097266.

Watanabe, T., Shirasugi, Y., Yano, H., and Michibayashi, K., 2011, Seismic velocity in antigorite-bearing serpentinite mylonites: Geological Society, London, Special Publications, v. 360, p. 97-112.

Webber, C. E., Little, T., Newman, J., and Tikoff, B., 2008, Fabric superposition in upper mantle peridotite, Red Hills, New Zealand: Journal of Structural Geology, v. 30, no. 11, p. 1412-1428.

Wenk, H.-R., Kanitpanyacharoen, W., and Voltolini, M., 2010, Preferred orientation of phyllosilicates: Comparison of fault gouge, shale and schist: Journal of Structural Geology, v. 32, no. 4, p. 478-489.

White, R. W., Powell, R., and Holland, T. J. B., 2007, Progress relating to calculation of partial melting equilibria for metapelites: Journal of Metamorphic Geology, v. 25, no. 5, p. 511-527.

Zhang, H., van der Lee, S., Bina, C. R., and Ge, Z., 2021, Deep dehydration as a plausible mechanism of the 2013 Mw 8.3 Sea of Okhotsk deep-focus earthquake: Frontiers in Earth Science, v. 9, p. 521220.

Zucali, M., Barberini, V., Voltolini, M., Ouladdiaf, B., Chateigner, D., Mancini, L., and Lutterotti, L., 2015, Quantitative 3D microstructural analysis of naturally deformed amphibolite from the Southern Alps (Italy): Microstructures, CPO and seismic anisotropy from a fossil extensional margin, Rock deformation from field, experiments and theory: A volume in honour of Ernie Rutter, Volume 409, Geological Society of London, p. 201-222.

Zucali, M., and Chateigner, D., 2020, Crystallographic and seismic anisotropies of calcite at different depths: A study using quantitative texture analysis by neutron diffraction: Minerals, v. 10, no. 1, p. 26.

국문초록

섭입대에서 관찰되는 중발지진과 지진파 이방성을 이해하기 위해 녹니석 페리도타이트의 변형미구조에 대한 자연암석과 변형실험에 대한 연구를 수행하였다. 첫번째 단계로서 노르웨이 Almklovdalen지역 녹니석 페리도타이트의 변형미구조를 연구한 결과 과거 보고되었던 감람석의 A, B, C, E타입 격자선호방향과 더불어 녹니석의 두가지 다른 격자선호방향을 발견해 타입 1, 타입 2로 명명했다. 녹니석의 타입 1 격자선호방향은 [001]축이 엽리에 아수직한 방향으로 배열되어 있으며, 타입 2 격자선호방향은 [001]축이 선구조에 수직한 방향을 둘러싸는 모양으로 분포하고 있다. 녹니석의 격자선호방향은 감람석보다 더 강하게 형성되어 섭입대의 지진파 이방성에 큰 영향을 미쳤다. 특히 빠른 S파의 편파방향이 슬랩의 섭입각에 따라 90도까지 회전하는 것으로 나타났다. 45도 이하의 작은 섭입각에서는 해구에 수직한 지진파 이방성이 형성되었으며 50도를 넘는 큰 섭입각에서는 해구에 평행한 지진파 이방성이 형성되었다. 두번째 단계로서 녹니석의 두가지 격자선호방향이 형성되는 조건을 밝혀내기 위한 고온 고압 암석변형실험이 수행되었다. 0.5~2.5GPa, 540~720℃의 온도 압력 조건 하에서 녹니석 페리도타이트의 단순전단 변형실험으로 녹니석의 두가지 다른 격자선호방향이 생성되었다. 녹니석의 타입 1 격자선호방향은 3.1±0.3 이하의 작은 전단변형 조건에서 형성되어 해구에 평행한 지진파 이방성 편파방향을 만들어냈으며, 녹니석의 타입 2 격자선호방향은 5.1±1.5 이상의 큰 전단변형 조건에서 형성되어 해구에 수직한 지진파 이방성 편파방향을 만들어냈다. 마지막 단계로서 중발지진(50~300km) 발생을 설명하기 위한 녹니석의 탈수약화작용을 연구하였다. 0.5~2.5GPa, 500~750℃의 온도 압력 조건 하에서 녹니석 페리도타이트 암석변형실험이 수행되었다. 1.5~2.5GPa의 고압조건 하에서 녹니석의 부분탈수반응이 관찰되었다. 탈수반응의 결과

Ca각섬석이 생성되었고 그에 따라 단층 구조가 형성되었다. 섭입대에서 녹니석 페리도타이트상은 이중 지진성 지역(double seismic zone)을 포함한 영역에서 안정하게 존재할 것으로 생각되기 때문에, 이 실험 결과로서 녹니석이 이중 지진성 지역의 중발지진을 설명하는데 중요한 역할을 할 수 있을 것으로 기대된다.

주요어 : 녹니석, 격자선호방향, 지진파 이방성, 지진, 탈수약화작용
학 번 : 2012-20335

감사의 말

하고싶은 일에 무조건 도전하고 항상 마음속의 꿈을 이루기 위해 살아야 한다는 일념을 품어온 저에게, 지질학을 전공하고 대학원에 진학하는 것에는 한치의 망설임도 없었습니다. 그러나 그 나이대에 으레 그렇듯 일생의 중대한 기로가 되는 사건들을 겪게 되고 누구도 예상할 수 없었던 장벽을 마주하게 되어, 학위과정의 길을 걷는다는 것이 생각처럼 순탄하지 못하게 되었습니다. 응원은커녕 비아냥만 듣는 일에는 익숙했으나 소중한 꿈들이 제 손을 떠나가게 되는 일은 견디기 어려웠습니다. 그러던 와중 저에게 용기를 심어준 여러 사람들이 없었다면 이렇게 학위과정이 결실을 맺게 되는 일은 없었을 것입니다. 저에게 많은 배움과 도움을 준 여러분께 감사한 마음을 떠올리며, 앞으로도 어려운 일이 있더라도 충분히 이겨낼 수 있는 한 명의 연구자가 되었음을 되새깁니다.

가장 먼저 지도교수 정해명 교수님께 감사드립니다. 긴 시간동안 곁에서 많은 것을 보고 배운 덕에 대학원 석박사통합과정을 졸업할 수 있게 되었습니다. 특히 세계 각국에서 경험한 여러 야외조사는 저에게 즐겁고 유익한 공부가 되었습니다. 다른 곳에서는 결코 배울 수 없는 많은 것을 가르쳐 주신 것 감사드립니다. 또한 박사 학위논문 심사에 참여해주신 이준기 교수님, 이현우 교수님, 전남대 길영우 교수님, 충북대 박문재 교수님, 그리고 제안 발표를 심사해주신 이인성 교수님, 이준기 교수님, 김영희 교수님, 부경대 강태섭 교수님께 감사드립니다. 교수님들의 여러 조언덕에 많은 것을 배울 수 있었고, 제 박사 학위논문이 크게 보완되고 개선될 수 있었습니다.

오랜 기간 동고동락한 지체구조물리학 연구실 동료들에게 감사의 말을 전합니다. 정세진 박사님, 박용 박사님, 재석형, 석영, 준하, 정진,

승순, 윤해, Krista, 그 외에 박문재 교수님, Yi Cao 교수님, 현선, 장윤용 선생님, 김선우 선생님 등 여러 사람들이 함께해 준 덕에 지금의 제가 있을 수 있었습니다. 특히 연구실의 기둥이자 연구 내외적으로 수많은 도움을 준 박용 박사님, 훌륭한 연구 동료이자 오랜 친구인 석영, 항상 좋은 친구로서 힘이 되어주고 함께 연구에 힘써준 정진, 고된 연구실 생활 중 즐거운 추억들을 함께할 수 있게 해 준 승순에게 특별한 감사를 전하고 싶습니다.

이외에도 학부와 대학원 과정을 거치며 여러 선후배와 교수님들을 통해 큰 가르침과 도움을 받았습니다. 김대영 박사님, 김태환 박사님, 이유영 박사님, 김영민 박사님, 김기범 교수님, Koen de Jong 교수님, 김지혁 박사님, 이아침 박사님, 선화씨, 다인, 나현씨, 지수, 현우, 지훈, 주호에게 감사하다는 말을 전하고 싶습니다. 항상 행정실에서 수고하고 계시며 여러 도움을 주신 장정란 선생님, 신성미 선생님, 이강준 선생님, 유정현 선생님, 김종원 선생님께 감사드립니다. 그리고 곤란한 경제적 상황 중에 수혜 받을 수 있게 된 장학금이 없었다면 학위과정이 무사히 마무리될 수 없었을 것입니다. 손동준 기부자님께 깊은 감사를 드립니다.

마지막으로 아버지, 어머니, 형에게 감사를 전합니다. 그리고 항상 모든 것에 함께하시고 저를 끝까지 붙들어 주시는 하나님 아버지께 무엇보다 큰 감사를 드립니다.